The Design of a Refrigerated Semi-Trailer using Advanced Composites

by

Ockert Jacobus Strydom

Thesis presented in partial fulfilment of the requirements for the degree of

Master of Science in Mechanical Engineering

at

Stellenbosch University

Submitted to the
Department of Mechanical and Mechatronic Engineering
Faculty of Engineering

Study leaders **Dr. E Terblanche** and **Mr. K van der Westhuizen**

Stellenbosch December 2007

Declaration

I, the undersigned, hereby declare that the work contained in this thesis is my own original work and that I have not previously in its entirety or in part submitted it at any university for a degree.

SIGNATURE:

DATE:

Summary

A refrigerated semi-trailer was designed to solve manufacturing and operational problems. This was achieved by using advanced pultruded composites. The static and dynamic material response was determined. The dynamic loading on the vehicles was also measured and is presented along with static load cases. These boundary conditions were used in a finite element model to determine the structural performance of the trailer. The results show good static performance with some problem areas which still need attention. Initial poor fatigue performance is improved by increasing the ultimate shear stress of the material. A fatigue optimisation technique is suggested for future use.

Opsomming

‘n Verkoelde leunwa is ontwerp om vervaardiging en operasionele probleme op te los. Dit is vermag deur die gebruik van gevorderde pultrusie saamgestelde materiale. Die statiese en dinamiese material eienskappe is bepaal. Die dinamiese belasting op die voetuie is ook gemeet en word saam met die statiese las gevalle aangebied. Hierdie randwaardes word gebruik in ‘n eindige element model om die strukturele gedrag van die leunwa te bepaal. Redelike statiese resultate is gekry maar daar is sekere aspekte wat meer aandag nodig het om die ontwerp produksie gereed te kry. Aanvanklike swak uitputtings gedrag word verbeter deur die gebruik van ‘n hoër skuifsterkte materiaal. ‘n Uitputtings optimerings tegniek word voorgestel vir toekomstige gebruik.

Newton remarked that if he saw further, it was because he stood on the shoulders of giants. However these giants do not only include the Great Masters but also those around us who support and guide us.

Therefore I dedicate this thesis to my giants.

My Parents, Grand Parents, Brothers, and Friends.

Acknowledgements

All pultruded material used in this thesis was kindly donated by *Fibretek* a local pultrusion manufacturer situated in Somerset West. A great debt of gratitude is owed to Mr. Gavin Wilson, managing director of *Fast'n Fresh*, who provided the opportunity to perform the verhicle service load measurements in spite of the disruption of their operations.

I would also like to thank the following persons:

Mr. Ferdi Zietsman who provide so much support with the experimental work and was always ready with advice when *Mr. Murphy* insisted on changes to well set plans. Thank you very much Ferdi.

Mr. Kobus van der Westhuizen for his great help and guidance with everything surrounding composite materials.

The friends and family which provided unlimited and unwavering support and encouragement when the nights were long and the challenges many.

Finally, a special word of thanks to my primary supervisor Dr. Terry Terblanche. For encouraging me to start this journey and giving me the means to do so. Then allowing me the freedom to find my own way while subtly guiding me when the need arose.

Table of Contents

List of Figures

List of Tables

List of Variables and Abbreviations

Variables

A_r	Average roving area
B	Fatigue strength depreciation per decade
E_1	Longitudinal stiffness
E_2	Transverse stiffness
F	Force
F_{king}	Reaction force at king pin
F_{scuff}	Scuffing force due to manuoevring
G_{12}	In-plane shear stiffness
G_{13}	Longitudinal through thickness shear stiffness
G_{23}	Transverse through thickness shear stiffness
H_{fe}	Hill failure index calculated with FE analysis
L_{k_b}	Distance between king pin and centre bogie
LF	Percentage fatigue strength depreciation per decade
M_{bogie}	Moment applied at bogies
m	Mass or fatigue material constant
m_g	Mass of all reinforcement
m_{SM}	Mass of stitched mat reinforcement
N	Newton, Normal force, Cycles to failure
N_{axle}	Normal force per axle
n_i	Number of cycles of vibration for the i^{th} acceleration bracket
n_r	Number of rovings per unit width
t_r	Assumed *in situ* average roving-matrix thickness
t_{SM}	As manufactured thickness
V_f	Volume fibre fill fraction
V_g	Total volume of reinforcement in specimen
V_m	Volume matrix fill fraction
$(V_f)_r$	Roving volume fill fraction
$(V_f)_{SM}$	Stitched mat volume fill fraction
w	Weight per unit area
Y	Yield specific

Variables, continued

ΔS	Stress ratio of applied stress to ultimate stress
υ_{12}	Longitudinal Poisson's ratio
υ_{21}	Transverse Poisson's ratio
ρ_r	Density of fibres
ρ_u	Unconsolidated density of mat reinforcement
σ_1	Stress in longitudinal direction
σ_2	Stress in transverse direction
σ_{UC1}	Ultimate longitudinal compressive strength
σ_{UC2}	Ultimate transverse compressive strength
σ_{UIL}	Ultimate interlaminar shear strength
σ_{UT}	Ultimate tensile strength
σ_{UT1}	Ultimate longitudinal tensile strength
σ_{UT2}	Ultimate transverse tensile strength
τ_{12}	In plane shear stress
τ_{U12}	Ultimate in-plane shear strength
μ	Coefficient of friction
μ_s	Static coefficient of friction

Abbreviations

CFM	Continuous Filament Mat
CLT	Classical Laminate Theory
FE	Finite Element
FEM	Finite Element Model
FFT	Fast Fourier Transform
GRP	Glass Reinforced Polymer
RSM	Random Stitched Mat
TRIAX	Tri-axial Transverse Mat

Chapter 1 Introduction

This project forms part of a research area of the Vehicle Structures Group of the Department of Mechanical and Mechatronic Engineering at Stellenbosch University. Focus on the heavy road transport is natural, as it plays a vital role in the South African economy. According to the Second Annual State of Logistics Survey for South Africa 2005, eighty three percent of the annual 1239 million metric tonne of freight carried in South Africa was done so by road. Technologies which can be applicable in a South African context are identified and developed to satisfy specific industry demands. The use of advanced composites, specifically pultruded composites, in the transport industry is one such case.

Refrigerated semi-trailer transport has been identified as one of the areas where major improvement can be achieved. Consultation with industry indicated that the major deficiency of current semi-trailer designs is the load box. A large part of the total life cost can be attributed to failures in the load boxes and much improvement can be made if the load boxes are redesigned. Typically 72 percent of maintenance cost of the trailer is spent on the load box.

Pultruded composites offer many advantages as a structural material and are well suited to the transport industry. These include high strength to weight ratio, low thermal conductivity, structural optimisation and potentially low cost.

Thus the aim of the project is to:

Design a semi-trailer using pultruded composites with specific emphasis on improved reliability, improved structural performance and reduction of production costs of the load box compared to existing designs.

Chapter 2 Current Trailer Performance

2.1 Design investigation

There are only a few trailer manufacturers in South Africa. These include the older companies like *Serco, Henred Fruehauf, Busaf-Bauer* and also newer producers like *Cape Trailer Services*. Most local designs still use fibre glass clad wood panels as the major structural components in the load box. Floor beams are made of a complex sandwich of wood, steel and fibre glass. New hybrid designs, which make limited use of standard pultruded sections as structural members, are under investigation by various trailer manufacturers. This will probably be the dominating trend in the use of pultruded composites for the next few years. Although these hybrid designs are an improvement on the older designs, it still does not address the major weakness' which were identified in previous research, Strydom (**2002**). All local trailers produced still use wood as a major structural material. Although wood is quite light, strong and cheap it performs quite poorly in wet environments, such as the inside of a refrigerated trailer. In Appendix A and B different side walls and floor beams were tested to establish an understanding of the structural performance of current trailer elements.

2.1.1 European and American designs

Imported trailers are rare in South Africa. The importation cost is high and therefore local manufacturers have a virtual monopoly on the market. Imported trailers are generally built with higher technology and use more advanced materials.

The most well-known international brand is Utility trailer, produced in the U.S.A. The trailer is build mainly of aluminium. It is a chassis-less structure and has a very good reputation as being durable and it has been said to operate at a lower running cost. However no data could be located to support this.

On the European side, the Cargobull family of trailers is found. They utilise foam clad with thin steel plate, producing very strong side and roof panels.

Even though this is a very brief overview of the different design it does illustrate that South African designs are very much out dated.

2.2 Production and operating cost analysis

Production cost analysis is an important part of product design. The cost associated with certain features of the design, like maintenance, running cost or capital expenditure must be quantified in some manner to be able to deliver a better design. Du Toit (**2000**) has done an analysis of the current trailer construction cost and has concluded that the Glass Reinforced Polymer (GRP) load box is the area where the most improvement is possible. However, despite the sterling work of Du Toit (**2000**), little has changed in the construction of the load boxes during the past decade.

Table 1: Trailer cost breakdown as taken from Du Toit (2000).

Process	**% of Complete Trailer Cost**
Outsourced	40.69 %
GRP materials	27.28 %
Labour cost	22.72 %
Chassis materials	9.31 %

Table 2: Labour cost breakdown from Du Toit (2000).

Labour	**22.72 %**
GRP Labour	10.86 %
Steel Assembly	4.74 %
Cutting & Bending	3.95 %
Paint / Finishing Labour	1.78 %
GRP Doors / Fittings Labour	1.38 %

From the above analysis it is clear that the most promising solution to lower trailer cost is to redesign the load box. Load box materials constitute 27.28 percent of the total trailer cost and almost half (48 percent) of all labour cost is spent on load box manufacturing. Thus the load box contributes a total of 38.14 percent to the total trailer cost. It is clear from a manufacturing viewpoint that improvements can be made to reduce load box production costs. The redesign of the load box must use concepts that will reduce production cost and provide a structurally superior product.

To establish an operational viewpoint, a market leader in the refrigerated transport business was identified. Their operational data was reviewed to identify areas where significant

improvement can be made. For this purpose a large logistics operator *Fast'nFresh* was approachedto establish the short comings in their current fleet of trailers. They supplied operational cost data which is presented in the table below.

Table 3: Trailer performance parameters.

Performance parameter	**Value**	**Unit**
Lifespan of GRP box	4-5	Years
Lifespan of chassis	10	Years
Operating cost of GRP box	18	c/km
Operating cost of chassis (excluding tyres and cooling unit)	7	c/km
Cost of new trailer	R 260 000	ZAR
Average monthly mileage	16 000	km/month
Distance covered in ten year lifespan	1 920 000	km
GRP maintenance cost over ten years	R 345 600	ZAR

In Table 3 it can be seen that a total of R 345 600 is spent on the load box throughout its life cycle. It is also clear that the chassis design is quite mature. Chassis lifespan is quite acceptable and little structural repairs are done on the chassis itself. This is expected since the chassis is traditionally the main structural member of the trailer and much attention has been given in the past to that part of the design. This was done in an effort to increase the payload of the trailer while keeping the total weight within the maximum allowed by law. Most of the chassis operating cost can be attributed to maintenance of the running gear, like the axles and suspension elements, which are outsourced items. Therefore little can be done (in terms of load box design) to influence the chassis maintenance cost.

The maintenance to the load box contribute up to 72 percent of the total maintenance cost (not running cost) and is the main operational parameter that must be addressed.

Figure 1: Failure of semi-trailer side when loaded with loose fish and ice.

Figure 2: Close-up of failed trailer side, note the tie straps, these cause further damage.

The load box is made of laminated wood sheets covered with fibreglass. The wood is the main structural material and the fibreglass forms a seal. A load box will be replaced after a

period of 4-5 years and sidewall replacement is routinely carried out to repair damage caused by forklifts and accidents. It is quite difficult to distinguish between damage to the box by abuse and that caused by regular wear and tear. Inspection of refrigerated load boxes revealed many problems associated to the use of multiple-material-construction. Especially the use of wood causes many problems. Any hairline cracks in the GRP covering of the laminated wood, will allow water penetration. This in turn causes delamination of the wood and structural failure. The methods used to fix the frontal bulkhead and the sidewalls to the floor and roof is also an area of concern.

A major cause of damage to the sidewalls is forklifts. Forklifts will routinely use the lower 300 mm of the sidewall to guide the pallet down the length of the trailer. In the process holes or rips will be punched in the walls or the sidewall may even be dislodged from the floor. This is one of the major causes of failure which must be addressed.

Thus from an operations viewpoint it was found that the load box is very expensive to maintain and has half the life span of the chassis. According to operators, the optimal economic lifespan of a refrigerated semi-trailer is 8 years and this is the lifetime for which new designs must strive.

2.3 Conclusion

In this chapter the current state of semi trailer design in South Africa was compared to first world countries. Data was presented to show that the load box materials account for 38 percent of the material cost and that 48 percent of labour cost is spent on it. A reduction in manufacturing cost must be addressed with the new design. Poor durability of the load box is the main operational concern. Multi-material construction, fixing between the side wall and floor as well as damage caused by forklifts were listed as the major problems that need to be addressed.

The next chapter will start with the process of designing a trailer which prevents these problems.

Chapter 3 Load Box Design.

3.1 Introduction

Current designs do not utilise the structural capacity of the load box. Designs have depended on the chassis to carry the longitudinal bending moment of the distributed load and have relied on the floor structure to carry the transverse bending. The structural capacity of the load box has mostly been ignored, but the load box can play an important part in the structural design of the trailer.

Pultrusion is the specified manufacturing process as it offers various advantages for the production of load boxes. According to Brandt Goldsworthy, (**1990**), these include high strength to weight ratio, low thermal conductivity, structural optimisation and potentially low cost. Thus, the aim of this chapter is to develop, elegant load box structures that will increase the carrying capacity of the trailer while keeping the production cost down. This can be achieved by designing cross-sections that combine manufacturing efficiency with structural efficiency.

3.2 Design requirements

The following design requirements were used to generate the concept profiles.

- Use the pultrusion process.
- Reduce the number of dies to a minimum.
- Reduce the part count by using a modular design.
- The load box must be treated as a structural member.
- Maximise thermal efficiency.

These requirements are left purposely broad not to limit the concepts. The most basic load box system consists of two sides, a floor, a roof, a bulkhead and a door frame. These parts will be used to define the load box. The doors themselves are not included as their structural role is small and structurally they will be similar to the sides.

The reduction of dies is of paramount importance as they have a very high capital cost (typically between R400k to R1.2m) and have a limited lifetime.

The modular requirement naturally leads to systems where a number of identical components are used to construct bigger parts of the load box. This will reduce the number of dies and limit the number of different parts needed to build the trailer. Assembly of the modular components must be easy and simple with the maximum number of features build into the dies to reduce assembly cost. The efficient use of reinforcement plays a critical part in the reduction of weight but will be addressed at a later stage.

Only conduction will be considered in the thermal design of the sections. The total thickness of the trailer sides is constrained by two parameters. The first is the maximum legal vehicle width of 2600 mm. The second is the width of a shipping pallet. Two pallets, each 1200 mm wide, must fit into the trailer. With a side wall thickness of 65 mm thick and corner profile adding 10 mm more this leaves a minimum of 17 mm clearance along the pallets. This effectively fixes the maximum thickness of the side walls. Hence in terms of limiting conduction, focus will be on avoiding thermal bridges as far as possible and allowing for the maximum amount of thermal insulation. Further improvements may be possible by an appropriate choice of insulating foam. The insulating foam will have some impact on the structural performance of the sections but at this stage it is assumed (inaccurately, but conservatively) to be insignificant. Further attention should be given to this interaction in future development.

3.3 Pultruded sections

A number of concept profiles were generated and two very different designs will be presented here. With these designs the strong and weak points of pultruded sections are pointed out. The designs are labelled the Mono Profile and the Snap 750 System. The Snap 750 is the system of sections that is ultimately chosen for structural evaluation and the following paragraphs plot its evolution.

3.3.1 Mono Profile

The most extreme of the modular concepts is dubbed the Mono-Profile. This design uses four dies to form a complete floor, side and roof section. The side section is also used to form the bulkhead. Corner sections are incorporated into the floor and roof sections. The sides and bulkhead section is bonded into the corner sections to form the load box. A small capping section will form the door frame. All the sections except the capping is foam filled for thermal isolation.

Error! No topic specified.

Figure 3: Mono floor.

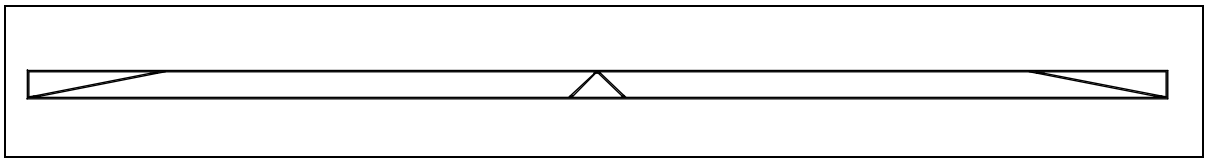

Figure 4: Mono side.

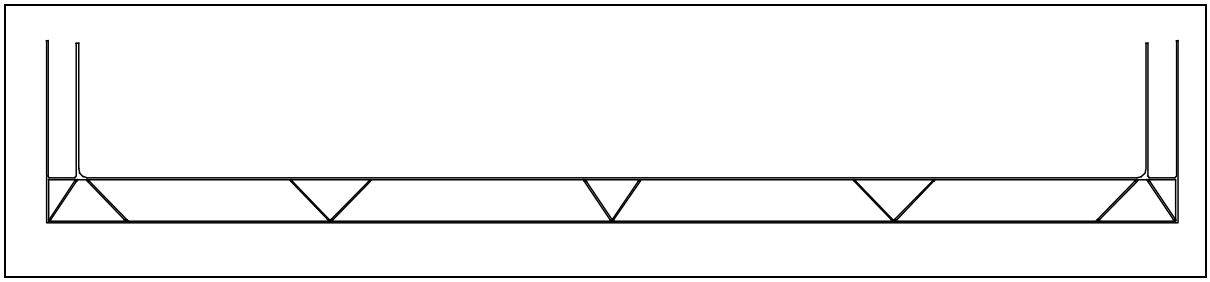

Figure 5: Mono roof.

Consultation with pultrusion equipment manufacturers proved this concept too complex to be successfully manufactured. The complexity is mainly caused by the size of the dies. Die manufacturing cost became prohibitive and so did the cost of the pultrusion and ancillary equipment. The decrease in assembly and labour cost does not off-set the increased capital expenditure. Further set-up of the pultrusion processes would become very difficult. The design of large profiles must balance the capital expenditure against decreased production cost.

3.3.2 Snap 750 System

To counter the cost and complexity problems of the Mono Profile the design was changed to utilise smaller, more cost efficient, dies and machinery. The following sections are proposed. All closed cells are foam filled for thermal insulation.

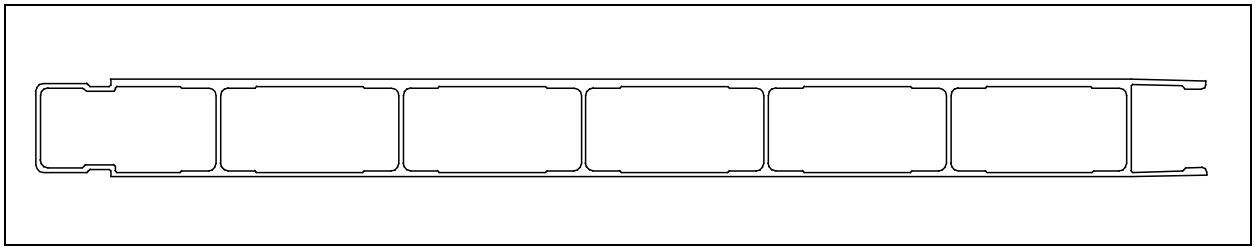

Figure 6: Snap 750 floor section.

At the heart of the design is the Snap 750 floor section. Web spacing is set at 125 mm with a covered size of 750 mm and a web thickness of 3.5 mm. A snap fit is included to allow the sections to be joined easily without clamping. Total section depth is 65 mm. Sections will be cut in lengths of 2458 mm and joined with epoxy adhesive to form the floor of the load box. The top skin is 5 mm thick with a bottom skin of 3 mm.

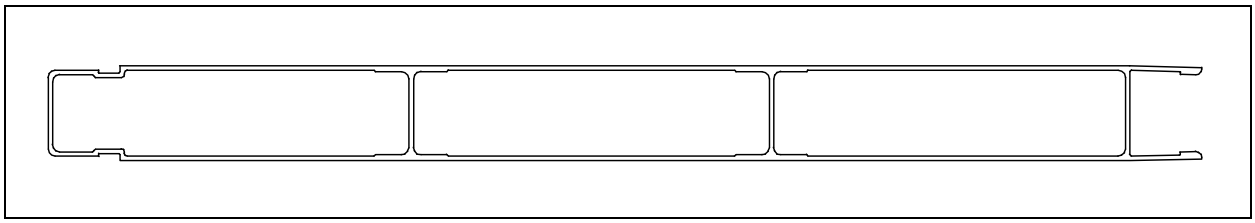

Figure 7: Snap 750 side section.

The Snap750 side section only uses three 3.5 mm webs for stiffening. The covered width is also 750 mm. This section uses the same outer die as the Snap 750 floor section which keeps the cost down. The section depth is set at 65 mm. This leaves a 17 mm clearance between the pallets and the sides of the load box. The Side 65 section will also be used for construction of the roof. Top and bottom skins are both 3 mm thick.

The sides and the floor are joined with the Corner 65 section. The internal leg of the Corner 65 forms a 300 mm high scuffing barrier on the inside of the load box to prevent damage by forklifts. The section is kept symmetrical to prevent problems with the mitre joints of the corners.

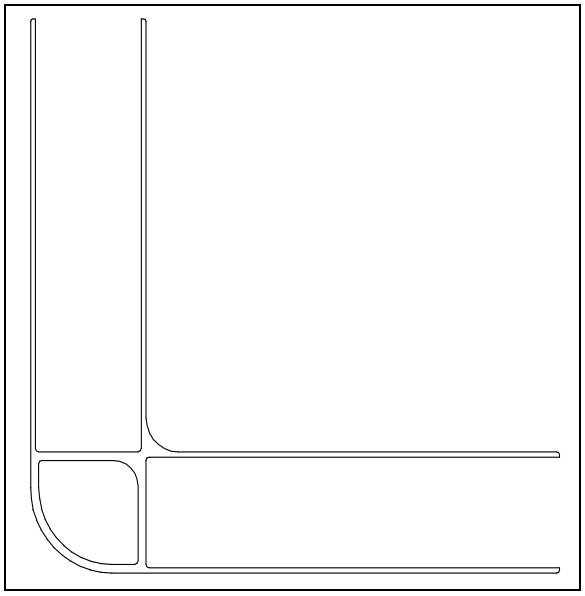

Figure 8: Corner 65 section.

There is two basic ways to use the Snap750 side sections. The first option is to install the sections running in the longitudinal direction and alternatively option two have the side sections running transverse over the chassis in the same way as the Snap 750 floor section.

Option one has the advantage of reducing assembly time, but an additional die is needed to form the roof, increasing the cost.

Option two allows the torsional paths between the roof and the floor sections to be completed, making the structure stiffer in torsion, and thus is superior from a structural point of view. There is also more scope for changes of the trailer height than with option one. Further, if a heavy duty construction is needed, for instance when animal carcasses are being transported, one can alternating use Snap 750 floor sections in the sides and the roof to form a very robust structure.

Thus option two, with superior structural performance and more flexibility is selected for further evaluation.

3.4 Conclusion

To conclude this chapter: Broad design requirements were listed as the reduction in manufacturing cost and the more efficient use of the construction materials. Two conceptual designs where presented to illustrated the need to balance capital expenditure and decreased production cost. A modular set of pultruded sections, called the Snap 750 System, was offered. This option gives an assembly configuration that increases the design options available to the manufacturer while reducing the manufacturing time.

In Chapter six the structural performance of the Snap 750 System will be evaluated. However, before structural analysis is attempted some further study of pultruded material is needed.

Chapter 4 Pultruded Material Characterisation

4.1 Introduction

To accurately model the behaviour of structures with finite elements, three inputs are needed. First, an accurate description of material properties, secondly an accurate description of the true loading on the structure and thirdly boundary conditions must be used to effectively simulate real constraints. In this chapter the first prerequisite will be addressed. This will be done with correlations between theoretical and experimental material properties. The distribution of fibres in a pultruded section will be investigated and the fatigue properties of a pultruded, continuous-filament-mat reinforced, composite will be presented. The chapter will conclude with the material properties to be used in the further development of the pultruded trailer and some thoughts on future material characterization.

Please note that throughout the chapter distinction is made between **laminate composites**, build of individual layers and **pultruded composites**, produced with the pultrusion process.

4.2 Testing laminated composites

It is general practise to determine the material properties of laminated composites by testing. The classical laminate theory (CLT) which is used to describe the behaviour of laminates is built on the knowledge of the material properties of each orthotropic lamina. For each orthotropic lamina E_1, E_2, υ_{12}, G_{12}, G_{13} and G_{23} must be known. These properties are, usually, determined by experiment but can also be calculated with the theory of Micromechanics.

Micromechanics require the properties of the constituent matrix and fibre of the lamina, which also has to be measured. Not only do Micromechanics predict the lamina properties but it also allows us to determine the sensitivity of these properties to changes in fibre fill fraction. Properties of the fibre and polymers matrixes are often supplied in handbooks on composite materials or can be sourced from suppliers as the difficulty of determining the properties of an individual anisotropic fibre (such as carbon fibre) are immense. Many of the individual fibre properties can only be back calculated from the composite properties of a lamina. Micromechanics also does not account for imperfect bonding between the resin and the fibres and stress concentrations caused by voids.

Further, to analyse the strength of a composite component, failure theories are employed. Orthotropic failure theories require ultimate stresses in tension and compression for both material directions as well as the maximum allowable shear stress. For multiple layers lay-ups, the interlaminar shear strength must also be determined. Thus, for every combination of resin and fibre the properties given by Table 4 must be determined by testing:

Table 4: Material properties needed for orthotropic materials.

Abbreviation	Description	Abbreviation	Description
E_1	Longitudinal stiffness	G_{12}	In-plane shear stiffness
E_2	Transverse stiffness	G_{13}	Longitudinal through thickness shear stiffness
υ_{12}	Longitudinal Poisson's ratio	G_{23}	Transverse through thickness shear stiffness
σ_{UT1}	Ultimate longitudinal tensile strength	σ_{UC1}	Ultimate longitudinal compressive strength
σ_{UT2}	Ultimate transverse tensile strength	σ_{UC2}	Ultimate transverse compressive strength
τ_{U12}	Ultimate in-plane shear strength	σ_{UIL}	Interlaminar shear stress

4.3 Testing of pultruded composites

Pultruded composites can be treaded as a special case of the laminated composite, as a lay-up with only a single layer. Testing is performed at laminate level and the laminate properties are used to describe the behaviour of the laminate as a single layer of orthotropic material. This is not ideal as the tensile and flexural moduli of laminated composites differ, a result of the combination of the position of each layer and its relative stiffness in the plane of bending. The analogue is true of pultruded composites, but the difference is caused by the positioning of individual fibre bundles. Thus, some knowledge of the loading on the component is needed to perform proper testing. If the load on the laminate is either pure tension or pure bending then the appropriate moduli can be used.

The layering also causes coupling between the tensile and flexural response of the laminate composite which is not taken into account when modelling the pultruded composite as a single orthotropic layer. This can be eliminated by using a symmetric lay-up which balances

the stiffness of each layer on either side of the section mid-plane and care must be taken when modelling non-symmetric composites.

On account of these challenges, laminate longitudinal and transverse tests are usually performed in tensile and flexure to determine E_1, E_2 and υ_{12} of the laminate in both modes. The in-plane shear modulus G_{12} is determined with the use of a special jig to ensure pure shear loading. Shear moduli in the other planes, G_{13} and G_{23} are difficult to measure and is assumed to be equal to that of the matrix material.

4.4 Experimental material properties

Tensile and flexural tests were performed on material from an 84×35 mm channel section with 5 mm flanges and a 3.5 mm web. Three different symmetric lay-up sequences were investigated, each with a similar core portion of rovings surrounded by a different transverse reinforcement.

- 450 gsm Transverse tri-axial, -45/90/45 (Triax)
- 300 gsm Continuous Filament Mat (CFM)
- 450 gsm Random Stitched Mat (RSM)

The difference between CFM and RSM concerns the length of the fibres used to form the random orientation mat. CFM uses long continuous rovings and RSM uses normal chopped strand fibres which are stitched together. The major advantage of using CFM is the elimination of loose fibre ends, which makes handling and processing easier. The weight of the woven and stitched reinforcement was known but the number of rovings not. NCS 992, an isophthalic polyester resin from *NCS Resins* was used as matrix constituent, see the appendices for the material data sheet.

Table 5: Lay-up sequence.

Section	**Lay-up sequence**
84x35 mm channel	Triax / Roving / Triax
84x35 mm channel	CFM / Roving / CFM / Roving / CFM
84x35 mm channel	RSM / Roving / RSM

As can be seen in Table 5 the Triax and RSM reinforcements were placed on either side of the rovings. When the CFM three layers were used, one either side of the section and one in

the centre, bringing the total weight of transverse reinforcement material to 900 g/m^2 for all lay-ups tested.

Unfortunately not all tests could be performed to properly characterise the material. Tensile and flexural tests were performed according to ASTM D 3039 and ASTM D 790 on both the web and flanges of the pultruded section. Due to the size of the section no transverse samples could be cut that were large enough for tensile testing. Hence only flexural tests were performed, this was possible because no material was wasted to grip the specimen. No ASTM shear or compressive tests were performed due to the availability of the correct test jigs. However the shear stiffness of the CFM material is later correlated by a FE analysis to experimental tensile data (see Section 4.8 for more detail). The following results were recorded for the tensile and flexure tests.

Table 6: Summary of experimental material data.

Material	**Section**	**Material Direction**	**Tensile Strength [MPa]**	**Tensile Modulus [GN/m^2]**	**Flexural Strength [MPa]**	**Flexural Modulus [GN/m^2]**
Triax	Flange	Longitudinal	425.2	31.5	-	-
CFM	Flange	Longitudinal	367.6	35.7	-	-
RSM	Flange	Longitudinal	472.8	29.8	-	-
Triax	Web	Longitudinal	489.0	31.8	532.0	22.9
CFM	Web	Longitudinal	341.0	31.4	490.0	28.2
RSM	Web	Longitudinal	469.6	33.5	446.0	18.6
Triax	Web	Transverse	-	-	158.0	8.1
CFM	Web	Transverse	-	-	98.0	6.9
RSM	Web	Transverse	-	-	78.5	5.9

A surprising result to note is the relatively low tensile strength of the CFM reinforced material but its high tensile modulus. CFM also performed well in the longitudinal flexural test where it achieved the highest modulus, a possible explanation for these two points will be given in the next section. In the transverse flexural test the Triax material was supreme which was expected, as it contains the most transverse reinforcement. RSM in general gives good tensile properties although it is neither as strong nor as stiff as Triax. The flexural performance of RSM is inferior to both Triax and CFM. These results can be explained by different fibre distributions as will be shown in the next section.

4.5 Fibre distribution and volume fill fractions

If pultruded composite is to be modelled as a laminated composite a few things need to be kept in mind. The most important is that pultruded material is fundamentally non-laminated. The fibres in pultruded materials are usually highly aligned in the longitudinal direction, but the position of each fibre bundle can not be controlled as accurately as with normal lay-up methods. Stress and stiffness calculations with Classical Laminate Theory (CLT) use the distance of each layer from the mid-plane and the results are dependent on the square of this distance. Thus the fibre distribution in various parts of the pultruded section is an important parameter. For pultruded material made exclusively of rovings, this positioning is not as critical as when woven or stitched reinforcement is included between the rovings. The woven reinforcement disturbs the distribution of the rovings and causes uncertainty in fibre position, which makes CLT analysis of pultruded composites difficult. The best method to avoid this complication is to use the woven reinforcement on the outer surfaces of the section. This disturbs the rovings less and better correlation is achieved between the theoretical and actual lamina structure.

A further complication arises from the fact that the fibre fill fractions will differ between the tightly packed rovings and the less dense woven or stitched mat. These variations must also be quantified before the analysis can be performed. Davalos *et. al.* (**1996**) calculated the volume fill for rovings with the following relation.

$$\left(V_f\right)_r = \frac{n_r \cdot A_r}{t_r} \qquad \textbf{(4.1)}$$

where

$$A_r = \frac{1}{Y \cdot \rho_r} \qquad \textbf{(4.2)}$$

and n_r is the number of rovings per unit width and A_r the average roving area. The parameter t_r is an assumed *in situ* average roving-matrix thickness. It was assumed that the *in situ* roving thickness is equal to the laminate thickness less the thicknesses of the woven reinforcement layers. The area per roving is equal to the reciprocal of the product of Y, the yield specific (length of a kg of roving) in m/kg and ρ_r the density of the fibres.

For stitched mats Davalos *et. al.* (**1996**) uses:

$$(V_f)_{SM} = \frac{w}{\rho_u \cdot t_{SM}} \quad \textbf{(4.3)}$$

Where w is the weight per unit area and ρ_u the unconsolidated density of the mat. The "as manufactured thickness" is designated t_{SM} and must be supplied by the manufacturer. Neither approach could be used for this study since neither n_r nor t_{SM} were available from the manufacturer.

To give more insight in the fibre distribution, experimental data from various parts of the pultruded section was gathered. Results from these tests will later be used to predict the tensile modulus of different parts of the section with different reinforcements.

Five specimens from each reinforcement type, in both the web and flange, were subjected to a resin burn-out test to determine the specific fibre fill fractions. The data is summarised in Table 7. The volume fill fraction of the stitched mats was calculated with

$$(V_f)_{SM} = \frac{m_{SM}}{V_{SM} \cdot \rho_r} \quad \textbf{(4.4)}$$

where m_{SM} presents the recorded mass of stitched glass reinforcement and ρ_r the density of glass. A glass density of 2540 kg/m^3 is used throughout this text. The volume of the stitched mat is termed V_{SM} and is calculated from the product of the in-plane area of the tested specimen and the measured thickness of the burned stitched reinforcement. The roving filled fraction was determined by

$$(V_f)_r = \frac{m_g - m_{SM}}{(V_g - V_{SM}) \cdot \rho_r} \quad \textbf{(4.5)}$$

with m_g designating the total mass of glass reinforcement and V_g the total volume of reinforcement in the specimen. This calculation assumes that the total thickness of the specimen is the sum of the roving thickness and the thickness of the stitched reinforcement.

Table 7: Fibre fill fraction of various parts of the section.

Material	Flange volume fill fraction			Web volume fill fraction		
	Average [%]	**Mat [%]**	**Roving [%]**	**Average [%]**	**Mat [%]**	**Roving [%]**
Triax Transverse 450gsm	48.6	29.7	60.9	52.4	30.1	69.1
Continuous Filament Mat 300gsm	49.2	28.5	68.5	55.4	28.3	75.9
Random Stitched Mat 450gsm	49	33.7	59.0	Not tested		

The results clearly show a disparity between the average amount of reinforcement in the flange and web, with more fibre in the web. The average fibre distribution stays constant between the different types of woven reinforcement. The volume fill fraction of the stitched reinforcement itself also shows little variation. However, there is noticeably more roving present in both the web and flange in the specimens with CFM reinforcement. This explains the higher longitudinal tensile modulus of this material. The centre reinforcement also forces the stiffer rovings further from the neutral axis thus improving the flexural modulus substantially. This is a very effective method of improving the longitudinal flexural modulus while keeping the total amount of reinforcement constant.

Figure 9: Close-up of fired Triax specimen.

Figure 10: Close-up of fired CFM specimen, notice the irregular roving distribution.

Figure 11: Close-up of fired RSM specimen.

Further it is speculated that the low tensile strength of CFM may be attributed to the interlaminar shear failure due to the increased interfaces between the roving and mat. However no supporting calculations are performed.

4.6 Modulus estimates using micromechanics and classical laminate theory

Due to the high cost associated with development of pultruded composites it would be advantageous to use the available theoretical tools to estimate the performance of a lay-up sequence. In this section it is attempted to calculate laminate properties from fibre and matrix properties with a combination of micromechanics and classical laminate theory. The *Matlab*® computer code used for these calculations is presented in Appendix D.

Micromechanics is a simple tool to use during the development of composite lay-ups. It provides a method to extend the useful range of experimental lamina properties. The lamina properties can be used with Classical Laminate Theory to give us an estimate of the laminate properties such as tensile or flexural modulus. The only difficulty arises from the fact that fibre fill fraction varies through-out the pultruded section (see Figure 10 for an example of physical fibre distribution).

Tsai (**1988**) reports that micromechanical estimates of lamina properties based on the properties of the various constituents of the composite do not give the absolute accuracy needed. Tsai (**1988**) only uses these theoretical predictions to predict the relative change in stiffness when changing a single variable such as volume fill fraction.

4.6.1 Lamina properties calculated with Micromechanics

Various micromechanical theories exist, ranging from simple rule of mixtures relations to more complex, elasticity theory based models such as the concentric cylinders model and the three phase cylinder model as shown by Swanson (**1997**). As suggested by Herakovich (**1998**), as well as Agarwal and Broutman (**1990**), the rule of mixtures is used for the longitudinal stiffness and longitudinal Poisson's ratio. The rule of mixtures for calculating the longitudinal stiffness of unidirectional lamina is:

$$E_1 = E_f \cdot V_f + E_m \cdot (1 - V_f) \tag{4.6}$$

And both prefer the Tsai-Halpin equations to calculate transverse stiffness and shear modulus of an unidirectional lamina as seen in the equations below. The Tsai-Halpin relations are curve fitted expressions fitted to the exact elasticity solutions.

$$E_2 = E_m \left[\frac{1 + 2\eta \cdot V_f}{1 - \eta \cdot V_f} \right] \tag{4.7}$$

where

$$\eta = \frac{(E_f / E_m) - 1}{(E_f / E_m) + 2} \tag{4.8}$$

It is interesting to note that Tsai (**1988**) does not use this relation in his text book but rather chooses the Hahn stress partitioning parameter to correct the rule of mixtures. The stress partitioning parameter uses test data to achieve better correlation, by increasing the apparent stiffness of the matrix. Tsai (**1988**) also uses this method to extract difficult-to-measure fibre

properties, such as the transverse and shear moduli, from unidirectional composite test data. The following constituent properties are used for the micromechanical lamina estimates.

Table 8: The lamina constituent properties used with micromechanics.

Property	Value
Matrix Young's modulus	4.027 GN/m^2
Matrix Poisson's ratio	0.35
Fibre Young's modulus	72.4 GN/m^2
Fibre Poisson's ratio	0.2

4.6.2 Laminate properties using Classical Laminate Theory

Theoretical lamina properties form the input to classical laminate theory which is used to determine the response of laminated material. Pultruded material is a non-laminated composite, but can be modelled as laminated if the following is noted. Most of the longitudinal reinforcement is uniaxial and the transverse reinforcement is usually limited to stitched mats on the outer layers of the section. The position of reinforcement layers in the centre of the section is not as well defined as those on the outer layers and should be avoided if possible. This is due to the problems with fibre positioning as discussed before. Inaccuracies will result when modelling the flexural response and also the tensile response for unsymmetrical lay-ups. The three pultruded materials which were tested are modelled using the following logic.

The CFM reinforced material is modelled with a total of nine layers with transverse reinforcement on the top, centre and bottom layer of the laminate. The remainder of the thickness is made up of a number of uniaxial layers with the same thickness as the transverse reinforcement layers. The RSM material is modelled with a total of eighteen layers, of which the top two and the bottom two represent the woven reinforcement. The Triax material is described with a total of eighteen separate layers. With the top three and the bottom three layers constituting the tri-axial reinforcement with the correct fibre angles. The remainder of the lay-up is made up of layers of uniaxial roving.

An alternative route is to model the specimens with simple finite element models to determine the laminate performance, especially the more cumbersome bending stiffness. However the theoretical modelling of pultruded material can form a research field of its own.

This thesis is limited to the calculation of the tensile stiffness of a known pultruded lay-up using classical laminate theory with lamina properties as predicted with a rule of mixtures approach and the Tsai-Halpin relations.

4.6.3 Results of modulus estimates

In Table 9 the results from the modulus estimates can be seen. It is clear that the correlation between the experimental and theoretical data is not very good and the errors range between 7.6 percent and 32.6 percent. This should be expected as explained in the introduction of section 4.6 on page 22. Other sources, Davalos *et. al.* (**1996**), have found good correlation between experimental data and rule of mixtures micromechanical models. The discrepancy could be caused by error in matrix properties as provided by the manufacturer. Further research on theoretical stiffness prediction should qualify actual resin properties. In addition the use of strain gauges must be made to increase confidence in the experimental results.

Table 9: Theoretical and experimental material properties.

Material	**Section**	**Material Direction**	**Tensile Modulus [GN/m^2] Percentage error given in brackets**		
			Experimental data	**Theoretical prediction with Tsai-Halpin**	**Theoretical prediction without Tsai-Halpin**
Triax	Flange	Long	31.5	37.1 (17.8)	36.6 (16.2)
CFM	Flange	Long	35.7	38.8 (8.7)	38.4 (7.6)
RSM	Flange	Long	29.8	39.5 (32.6)	39.1 (31.2)
Triax	Web	Long	31.8	39.9 (25.5)	38.3 (204)
CFM	Web	Long	31.4	41.6 (32.5)	41.5 (32.2)
RSM	Web	Long	33.5	-	-

The data does, however, give insight into the magnitude of errors associated with absolute accuracy of the micromechanics/CLT approach. All theoretical estimates are higher than the experimentally determined moduli. Errors due to the experimental methods used will influence the results, but these errors will be less than 5 percent which still leaves a large discrepancy between the results. It is interesting to note that the Tsai-Halpin correction is only in the order of a few percent and increases the modulus estimates.

4.7 Fatigue properties of CFM reinforced pultruded material

Fatigue tests were performed to establish a stress-amplitude versus cycles-to-failure curve for the CFM material. The data will be used with the finite element results to calculate a total structural lifespan of the trailer.

The tests were executed in a MTS810 material test system. The test frame dates from 1971 and hence the data acquisition of the frame was replaced with more modern equipment, however the PID controller was still used to control the test frame. Load was measured with a 10000 lb MTS 621.22 load cell. Signal conditioning and data acquisition was handled by a HBM Spider8. Due to the maximum load limitation on the test frame of 26 kN, specimen width was reduced from 25 mm as used in the material characterization test to 12 mm. The tensile failure load was re-characterised (see Table 11) as the specimen geometry was now changed and the half-cycle failure load (tensile test forms half of a fatigue cycle) is needed to complete the Stress/Cycles-to-Failure graph.

Table 10: Fatigue test equipment.

Description	**Model**	**Serial number**
Test frame	MTS 312.31	#170
Controller	MTS 810	
Load cell	MTS661.21 10 000lb	#470
Extensometer	HBM DD1 +/- 2.5mm	44904
Bridge amplifier	HBM Spider8-30	F04083
	HBM Scout55	

Table 11: Ultimate strength results of fatigue specimens.

Specimen number	**Failure stress [MPa]**
T4	372
T5	339
T6	371
Average	**360.6**
Standard deviation	18.6

Seven specimens were tested under sinusoidal tensile loads with the stress amplitude varying between zero and a set value. Test frequency was set to 8 Hertz. The following fatigue data were recorded.

Table 12: Tabulated fatigue results.

Specimen	Load amplitude [MPa]	Cycles	Comments
Static average T4-T6	360	0.5	Average of three quasi-static tests
F2	172.4	93683	
F3	172.4	120871	
F4	210.7	2175	Failure due to Eskom electricity interruption
F5	210.7	6461	
F6	125	4278540	
F7	150	615210	
F8	240	1842	

All specimens demonstrated identical failure characteristics except specimen F4 which failed during an electricity interruption and is still included in the analysis of the results. The results were plotted on a linear/log graph which is shown in Figure 12. A logarithmic trend line was fitted to the fatigue data, including specimen F4, which shows close correlation between the data and the trend line which gives good confidence in the results. The effect of the premature failure of specimen four is very small and hence it is included for the sake of transparency. All data points are included in Table 12 for the reader to use further. More reference will be made to these results during the discussion of the finite element analyses.

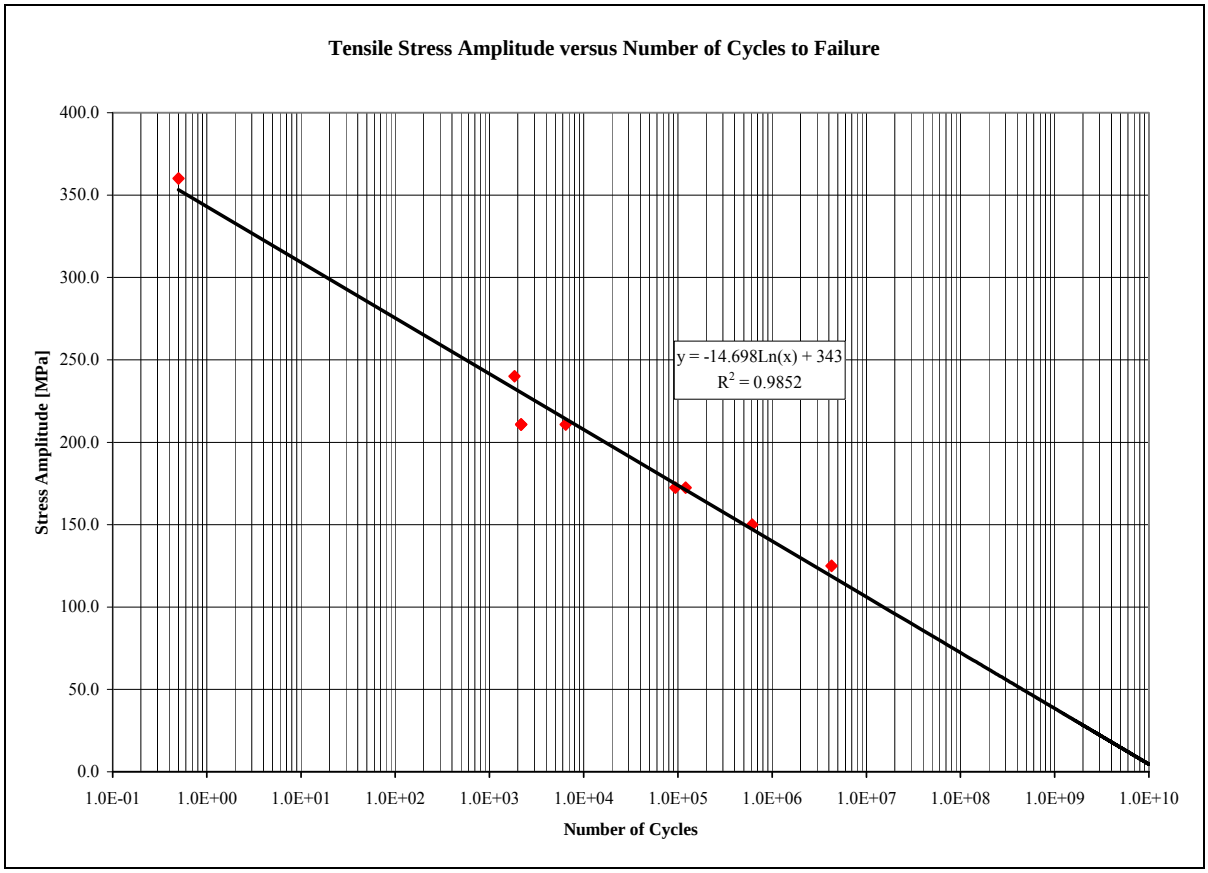

Figure 12: Stress amplitude versus Cycles to Failure graph.

Equation (4.11) results from a trend line fitted to the plot of the stress ratio, ΔS, versus cycles-to-failure, N where:

$$\Delta S = \frac{\sigma_F}{\sigma_{UT}} \tag{4.9}$$

$$\Delta S = 343 - 14.698 \cdot \log N \tag{4.10}$$

Which corresponds to the form

$$\Delta S = \sigma_{UT} - B \cdot \log N \tag{4.11}$$

From which the strength loss per decade, LF, can be calculated as

$$LF = \frac{B}{\sigma_{UT}} \tag{4.12}$$

$$LF = 4.3\%$$

The results presented here supports Kellerman *et. al.* (**2005**) who report strength depreciation for pultruded composites of 3-5 percent of UTS per decade. Kellerman's postulate differs from the Mandell's accepted value of 10 percent per decade.

Furthermore Kellerman's data was generated from full scale specimens with a coupon size of 100×300 mm. These results show that the 3-5 percent loss rate is also applicable to small coupon geometries.

Agarwal and Broutman (**1990**) present fatigue data in the following form:

$$\frac{\Delta S}{\sigma_{UT}} = -m \log N + b \qquad \textbf{(4.13)}$$

If equation

$$\Delta S = 343 - 14.698 \cdot \log N \qquad \textbf{(4.10)}$$

is rewritten in this form, we have

$$\frac{\Delta S}{\sigma_{UT}} = -0.0408 \cdot \log N + 0.9528 \qquad \textbf{(4.14)}$$

where m and b are material constants with the values close to 0.1 and 1.0 respectively. This data seems to partially support such a classification. This representation is useful and will later be used to calculate the total lifetime of the trailer.

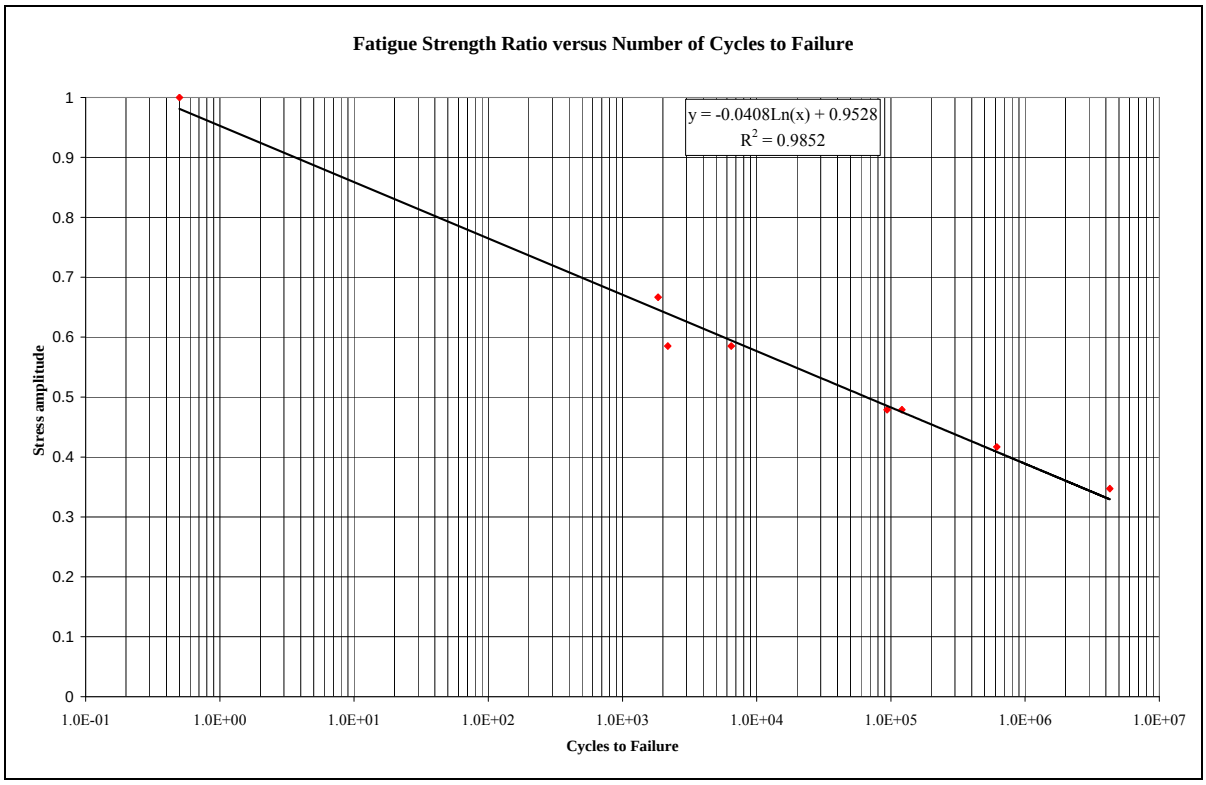

Figure 13: Fatigue strength ratio versus number of cycles-to-failure.

4.8 Orthotropic material properties for finite element analysis

For the finite element analysis of the trailer structure an orthotropic material must be defined to give a departure point. The CFM material is chosen due to the fact that fatigue data is available. The flexural properties will be used although the material will mostly be placed under tensile load. The reason for this is that only the flexural transverse modulus was determined due to the physical size of the specimens. The shear modulus was determined by the correlation of a finite element model to experimental data from an on-edge three point bending test. Good correlation was obtained between FEA results of flexure in the longitudinal and transverse directions. This gives reasonable confidence in the results of the shear experiment.

Table 13: Correlation results between FE analyses and experimental data.

Material	**Orientation**	**Predicted FEM deflection [mm]**	**Measured deflection [mm]**	**Error [%]**
CFM	Transverse flexure	1.775	1.768	0.4
	Longitudinal flexure	2.710	2.589	4.7
	Shear experiment	0.538	0.538	0

The following material properties will be used in the finite element analyses.

Table 14: Material properties for FE analysis.

Property	**Value**	**Property**	**Value**
E_1	28.2 GN/m^2	G_{12}	2.8 GN/m^2
E_2	6.9 GN/m^2	G_{13}	1.55 GN/m^2
υ_{12}	0.3	G_{23}	1.55 GN/m^2
σ_{UT1}	490 MPa	σ_{UC1}	490 MPa
σ_{UT2}	98 MPa	σ_{UC2}	98 MPa
τ_{U12}	23.4 MPa	σ_{UIL}	36.5 MPa

Maximum shear strength was taken from the online material property specification of a structural profile made by the company *Creative Pultrusions (www.creativepultrusions.com)*. The material shows a lower tensile strength and modulus compared to the *Fibretek* pultrusions tested. This leads to the conclusion that less reinforcement is used. Therefore the assumption of the likely lower shear strength is a conservative approach. Interlaminar shear

strength is equated to the shear strength of the matrix material and the Poisson's ratio was taken from literature.

4.9 Recommendations for future pultrusion testing programmes

For future testing programmes it is advised that uniaxial test samples be made to characterise the lamina properties for each resin and fibre combination. If woven reinforcement is to be used then these should be tested in the same weight and weave as would be used in production. All samples should have approximately the same fibrefill fraction as would be achieved in production. Tensile and shear tests should be performed according to ASTM 3039 and ASTM 5379 to properly characterise all the necessary orthotropic parameters as listed in Table 4. The experimental ply data can be used with finite element models to evaluate various lay-ups structurally. Micromechanics can be conservatively used if necessary to expand the properties for a range of fill fractions if the isotropic resin properties are experimentally determined.

4.10 Conclusion

In this chapter three pultruded materials from an 84×35 mm channel section were tested and analysed. Each material used different transverse reinforcement. Tensile moduli ranged between 29.8 GN/m^2 and 35.7 GN/m^2. A comparison was made between the tensile and flexural properties of the flange and web for each material and no preference could be found between the sections.

Further, fibre fill fractions in the flange and web was quantified for the flange and web and separately for the roving and mat reinforcement. The woven reinforcement showed considerably lower fill fractions at 30 percent compared to the 60 percent of the rovings. Fibre fill data was used with micromechanical and CLT theory to give a prediction of the tensile modulus for each material and each part of the section. Poor correlation was achieved with errors of between 8.7 percent and 32.6 percent. This may be due to error in matrix properties as supplied by the manufacturer or inaccuracies in the experimental programme.

A stress-amplitude versus cycles-to-failure graph was generated for the CFM material from tensile fatigue test data. A strength loss rate of 4.3 percent per decade was calculated from the data which correlates to the 3-5 percent found by Kellerman *et. al.* (**2005**). Correlation was also found with the fatigue data of Agarwal and Broutman (**1990**) who represent the data in equation form. Finally some recommendations are made regarding future testing of pultruded composites.

Chapter 5 Service Load Verification

5.1 Introduction

Loading on semi-trailers is comprised of the static loads of its own weight, the loading due to the cargo it carries, quasi-static loading due to manoeuvring of the vehicle and finally dynamic fatigue loads imposed on the structure due to interaction with the road surface. These four loading types are discussed and quantified in this chapter. The quasi-static loading on the trailer is expanded to include tyre scuffing and curb stepping loads.

Current design practise involves designing the steel chassis of a vehicle to limit stresses below the infinite life stress. This method frees the designer from the need to know the dynamic loads imposed on the structure and only the static loads are considered with a certain factor of safety. With materials which do not exhibit an infinite fatigue life, such as aluminium (used here for the chassis) and composites (used for the load box), it is necessary to know the fatigue performance of the material as well as the dynamic load profile. In the previous chapter the fatigue properties of CFM pultruded composite were determined. In addition to quantification of static and quasi-static loads, this chapter also list the results of measurements performed to quantify the fatigue loads to which a trailer is subjected.

5.2 Static and body loads

The South African Road Transport Act 93 of 1996 sets the maximum static axle load to 9 tonnes. This effectively limits the sum of the weight of the trailer and the payload. Hence what can be lost in trailer weight, can be gained in freight weight. Current three axle trailers have a mass of around 9 t with a maximum payload of 30 t depending on load distribution and axle placement.

5.3 Quasi-static manoeuvring loads

Quasi-static loads arise during manoeuvring and separate analyses are performed to evaluate the performance of the structure. Five manoeuvres are considered:

- Emergency breaking.
- High speed cornering.
- Step input from the road surface.
- Curb stepping.
- Tyre scuffing in tight, low speed turns.

The causes of the first three loads are quite well known and understood. The magnitude of these loads is taken from *The European Agreement concerning the International Carriage of Dangerous Goods by Road* (ADR), a specification used for design of tanker semi-trailers. These vehicles have the same total mass and use the same suspensions as refrigerated semi-trailers. More specifically the loads are taken from section 6.8.2.1.2 of ADR which specifies the loads the structure must be able to absorb. Some comment may be necessary to describe the last two manoeuvres.

Curb stepping occurs during wide turning where three rear wheels on one side of the trailer steps onto the pavement. The wheels are thus lifted approximately 200 mm resulting in torsion of the structure. Some of this movement is taken up by the suspension and the remainder resisted by the structure. The specific amount will depend on the specific suspension set-up used. A conservative figure of 50 mm will be applied in the finite element analysis.

Tyre scuffing is seen when tight turns are performed and is very pronounced in three axle trailers. During the turn, the trailer rotates around the centre bogie of the three axle set causing the outer wheels to move sideways on the road surface. This is not a rolling action but a scuffing action which causes a moment couple. The following conservative approach is used to calculate the magnitude of the reaction forces causing the moment.

The assumption is made that the trailer is fully laden with 90 kN per axle. The maximum couple will result when the load on the king pin is at 90° to the axial direction of the trailer. Hence the reaction moment at the centre bogie, produced by the scuffing tyres, can be

calculated by assuming a static friction coefficient of 1 and a distance between the bogies of 1.25 m.

The maximum reaction moment generated at the bogies is thus:

$$F_{scuff} = \mu_s \cdot N_{axle} \quad \textbf{(5.1)}$$

$$F_{scuff} = 1 \cdot 90 \quad \textbf{(5.2)}$$

$$F_{scuff} = 90\text{kN} \quad \textbf{(5.3)}$$

$$M_{bogie} = 2 \cdot 1.25 \cdot F_{scuff} \quad \textbf{(5.4)}$$

$$M_{bogie} = 225\text{kNm} \quad \textbf{(5.5)}$$

Now the force applied by the truck to turn the trailer can be calculated. The distance between the king pin and the centre bogie is 11.283m.

$$M_{bogie} = 225\text{kNm} \quad \textbf{(5.6)}$$

$$F_{king} = \frac{M_{bogie}}{L_{k\_b}} \quad \textbf{(5.7)}$$

$$F_{king} = \frac{225}{11.283} \quad \textbf{(5.8)}$$

$$F_{king} = 19.941\text{kN} \quad \textbf{(5.9)}$$

This force will be used in the finite element analysis to simulate tyre scuffing.

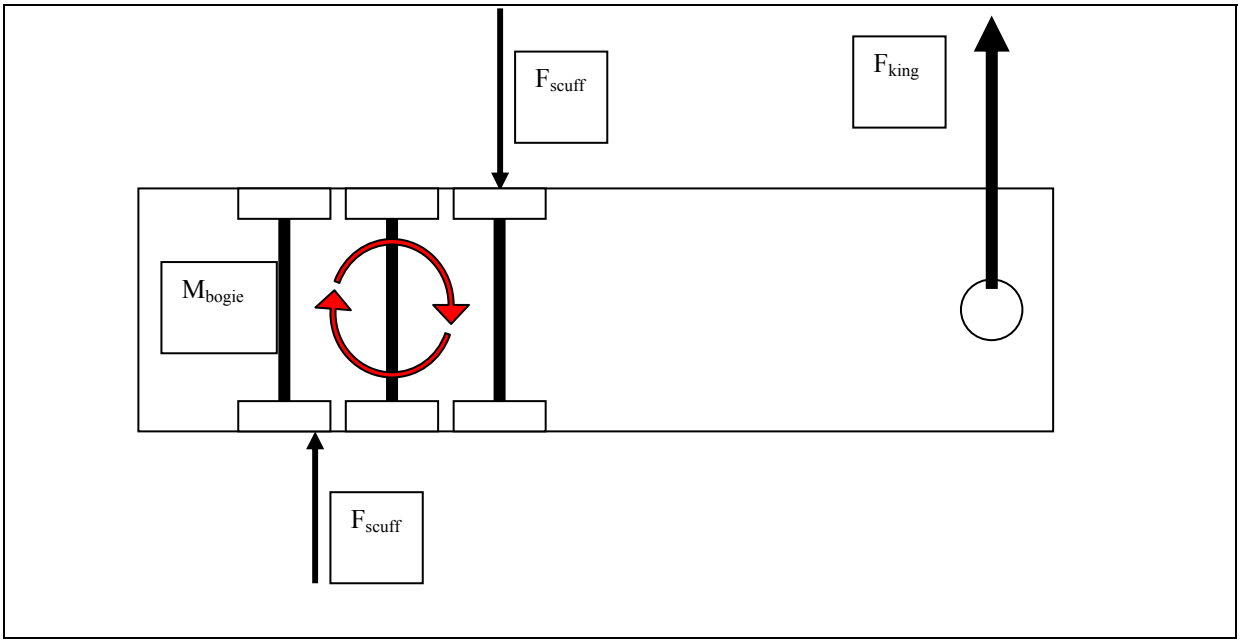

Figure 14: Scuffing loads on the trailer as viewed from above.

Table 15: Summary of loads imposed due to manoeuvring.

Manoeuvre	**Imposed force under maximum permissible load**	**Reference**
Emergency stop	Twice the total mass in the direction of travel. (2 g axial).	ADR 6.8.2.1.2.
High speed cornering and suspension roll.	The total mass at right angles to the direction of travel. (1 g transverse).	ADR 6.8.2.1.2.
Step input from road surface, such as pot holes	Total mass upwards and twice the total mass downwards. (1 g upwards, 2 g downward).	ADR 6.8.2.1.2.
Curb stepping	Torsion, 50 mm wheel displacement on one side.	Observed in the field.
Low speed tight turns	Scuffing of rear tyres, 90 kN, opposing, on each of the outer axles.	Observed in the field.

5.4 Fatigue loads

Body and quasi-static loads implies that the load is continuous or occurs slowly. The number of occurrences, during the life span of the trailer, of these loads is relatively few and is not the major cause of fatigue. The primary cause of fatigue of the trailer structure is the dynamic loading due to input from the road surface. The actual profile of the load is dependent on a number of variables. These include speed profile, suspension type, vehicle and cargo mass, damping of the structure and of course road surface. It is beyond the scope of this thesis to

qualify all these variables and their relative importance. Therefore measurements were performed on two refrigerated semi-trailers deemed to be representative of the current fleet of refrigerated trailers in South Africa. This generalisation is based on the following arguments.

Many heavy transport vehicles built in South Africa utilise *BPW* air suspension and axle systems. Hence the candidate trailers must be equipped with *BPW* suspension systems. The transfer functions of the different suspension models are not known and are only of use if the direct loadings due to road surface imperfection are known. Even then the transfer function of the tyres must also be considered. The approach of qualifying each sub-system is impractical due to the sheer number of possible combinations that must be investigated. It was decided to do direct measurements on the load box which eliminates the need to model suspension elements in the finite element analysis and substantially simplifies the model.

Further questions surround the cargo load of the candidate trailers. Trailers rarely run completely empty, thus no-load is not a valid condition in the consideration of fatigue life of a trailer. From discussions with operators two load scenarios seem typical. Heavy loads to transfer goods between major centres and heavy loads on the outbound leg and lighter loads on the return leg from lower populated areas.

With these considerations in mind, two return trips were made from Cape Town to East London and Johannesburg respectively covering a total of 5008 kilometres. These trips formed part of the operations of *Fast'n Fresh*, cargo carriers for *Woolworths*. On both legs of the East London trip the trailer was lightly loaded. For the Johannesburg journey the trailer was heavily loaded in both directions, however due to operational considerations no weigh bridge data is available for either trip.

Figure 15: Fast'n Fresh semi-trailer at load bay.

5.4.1 Experimental setup

The two trailers were instrumented with two *HBM B200* accelerometers. These were placed at the front and at the rear of the trailer. Data acquisition was performed with a *HBM Spider 8* unit. This is a 4.8 kHz transfer frequency bridge amplifier with a simultaneous sampling 12 bit analogue to digital converter. Data was sampled at 300 Hz.

5.4.2 Data analysis and results

A total of 1 Gigabyte of data was analysed. The data was broken into packets covering approximately 200 km each. The analysis consisted of calculating the acceleration peaks and sorting them into bins corresponding to the absolute vibration level. Twelve bins were used in a range of ±1.2 g resulting in a bin level of 0.2 g. The data of both trips were analysed separately and were normalised to a distance of 1000 km.

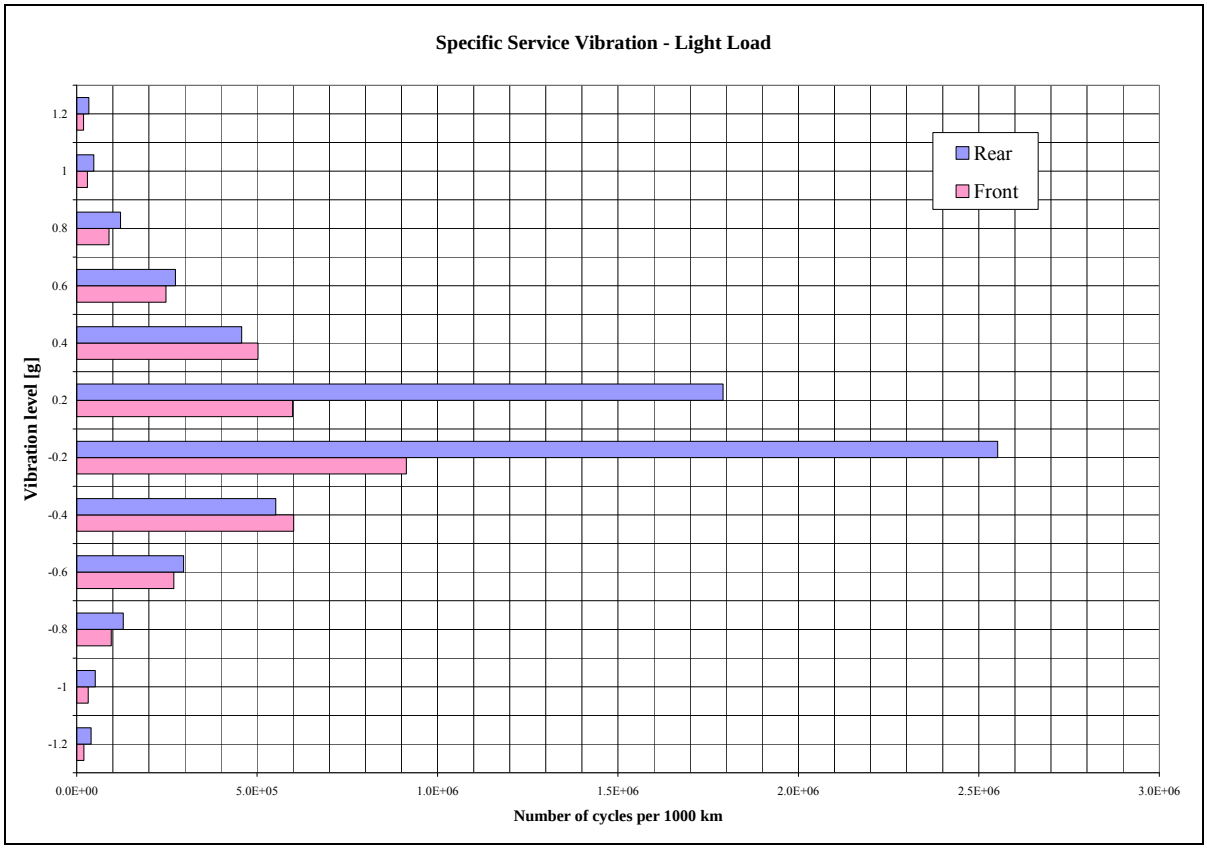

Figure 16: Specific 1000 km service vibration - light load.

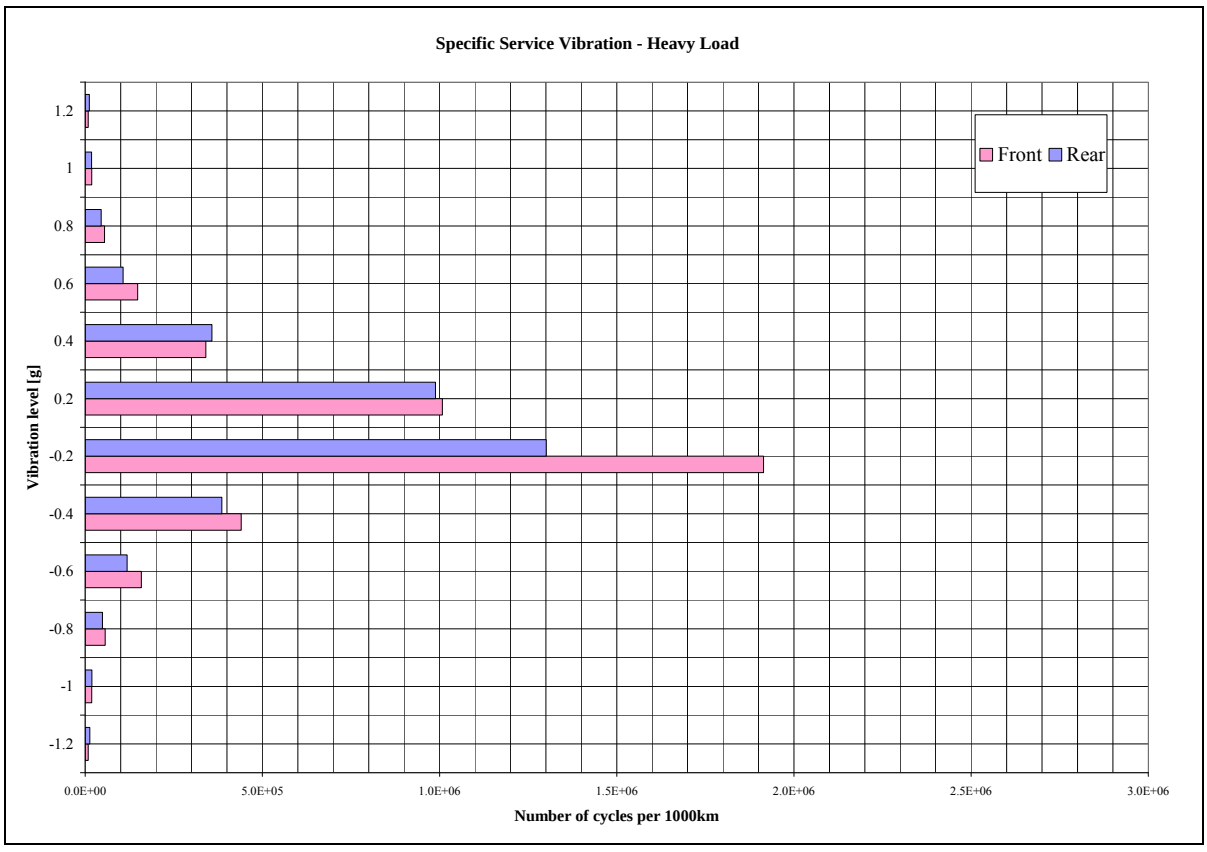

Figure 17: Specific 1000 km service vibration - heavy load.

When compared to the heavy load measurements the light load vibration levels are higher. The cause of this can be either due to rougher road surface or the lower mass, but is most likely a combination of the two.

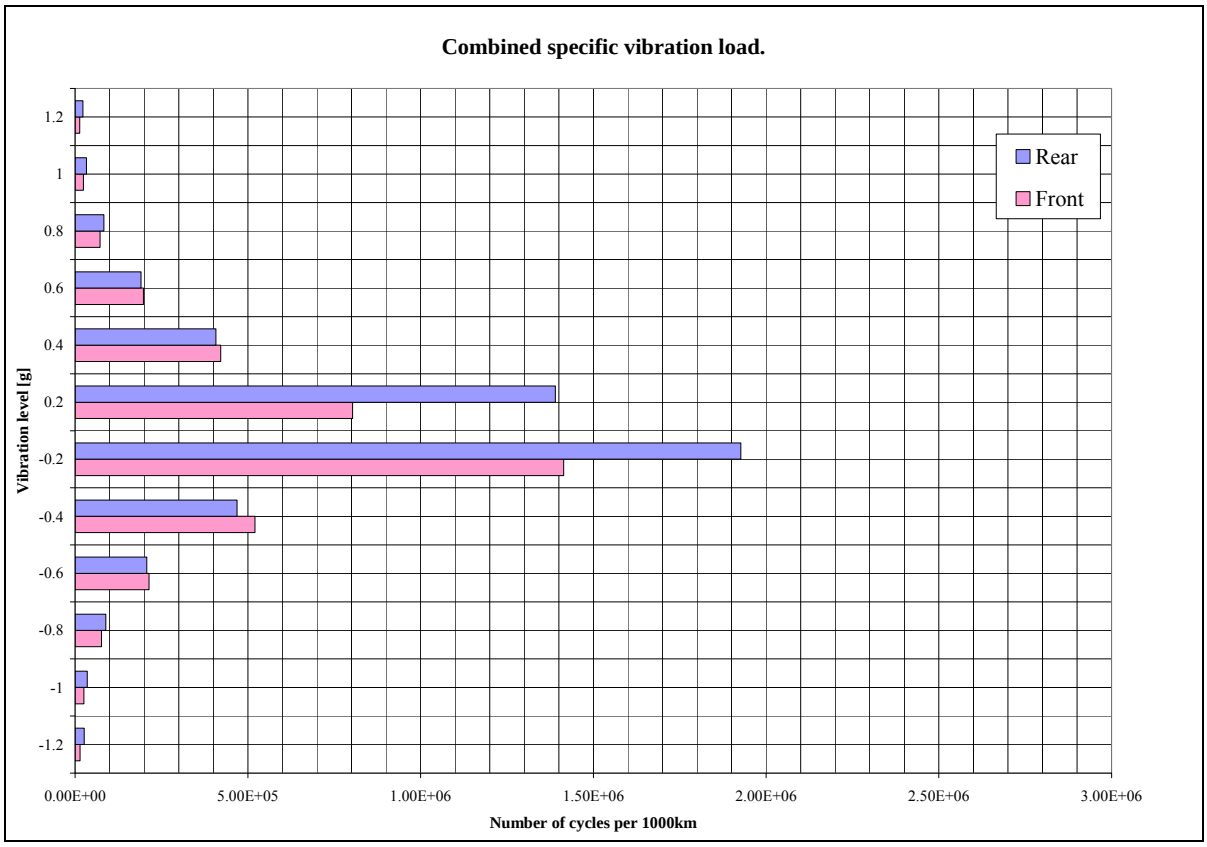

Figure 18: Combined specific vibration load.

The two sets of measurements were combined to form the figure above. The actual number of cycles is presented in Table 16. The vibration levels will later be used as load cases in a finite element analysis and the number of cycles will be used to calculate the life span of the proposed trailer.

Table 16: Combined specific service load.

Vibration level [g]		**-1.2**	**-1**	**-0.8**	**-0.6**	**-0.4**	**-0.2**
Cycles per 1000km	Front	14278	25179	75904	213865	520782	1413937
	Rear	26286	35320	88974	207079	468705	1926490
Vibration level [g]		**1.2**	**1**	**0.8**	**0.6**	**0.4**	**0.2**
Cycles per 1000km	Front	13598	23958	71983	197657	421250	803073
	Rear	22420	32652	83335	190363	407270	1390075

The Fast Fourier Transform (FFT) of the data was also calculated with a Hanning window for a frequency range of 0-150 Hz with a resolution of 0.07 Hz. The following plots show typical frequency spectra of the two trips.

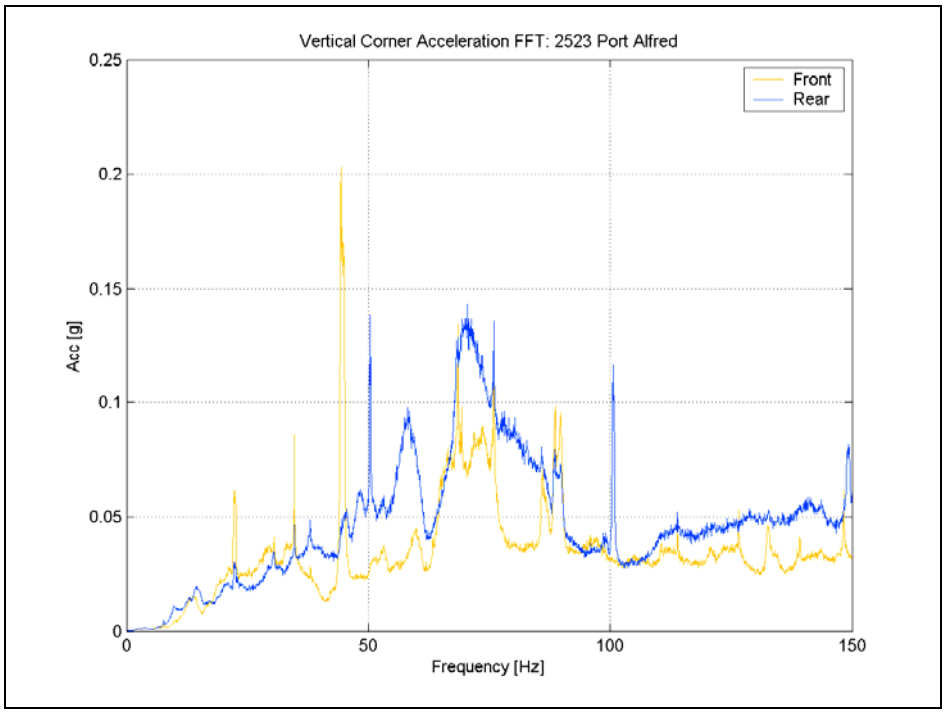

Figure 19: Typical frequency spectrum of vibration, Cape Town - East London.

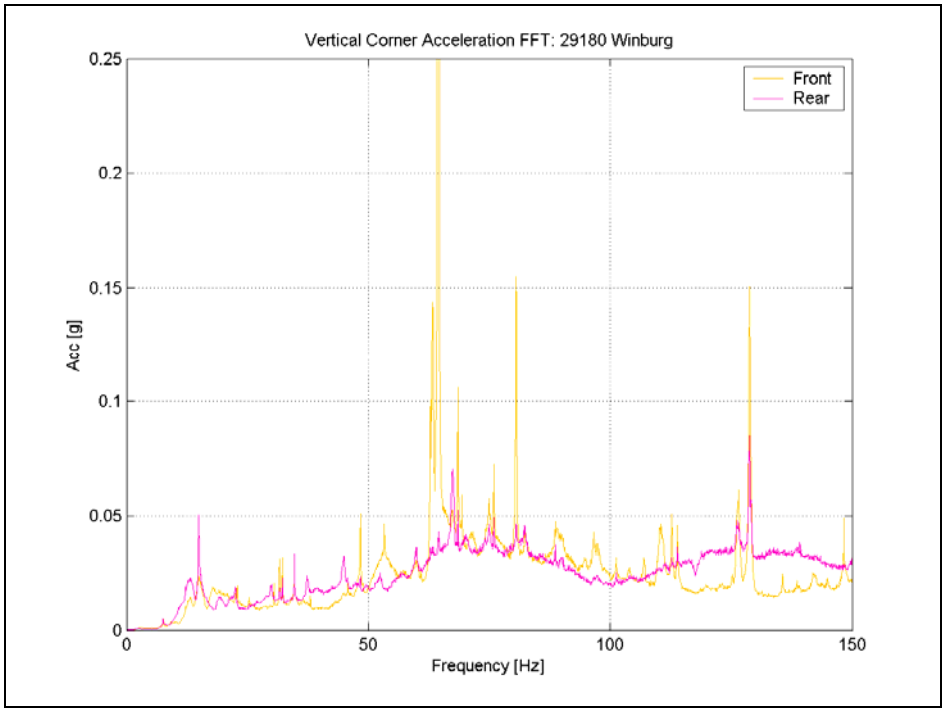

Figure 20: Typical frequency spectrum of vibration, Cape Town - Johannesburg.

Both figures have similar profiles although the Cape Town – East London journey shows significantly higher levels between 50 Hz to 80 Hz and the difference between the front and rear is more pronounced. The high acceleration of the rear may be attributed to the lower mass of the rear when compared to the combined mass of the front of the trailer which is attached to the fifth wheel of the tractor. Peaks at 50 Hz and 100 Hz are typical of electromagnetic interference. However the origin of this noise is not known as there is no 50 Hz systems onboard the trailer or tractor.

5.5 Conclusion

This chapter concerned itself with defining loads that act on a refrigerated semi-trailer. The loads were broken down into static, quasi-static and fatigue loads. Static loads were defined from the trailer and cargo weight. The quasi static loads were sourced from an European specification concerning the transport of dangerous goods and some additional manoeuvring loads as seen in practise. Finally the fatigue loads acting on trailers were measured and processed to give a histogram of the number of cycles at different vibration levels the trailer is exposed to over a distance of 1000 km.

These loads will be used as load cases for finite element analyses which is documented in the following chapter.

Chapter 6 Structural Analysis of the Proposed Trailer Design

6.1 Introduction

The material properties and loads as defined in previous chapters are used in a finite element analysis of the proposed load box. A conceptual chassis design is presented and included in the analysis. Detail chassis design is included but many aspects still need to be considered. These include fixings needed to produce a commercial semi-trailer such as light boxes, spare wheel stowage hangers and landing legs. It was found that static structural performance of the chassis and load box are very much inter-dependent and many design iterations were performed.

The chapter starts with a description of the finite element model. This includes the load box elements and properties, chassis elements and properties, constraints and load cases. The static performance of the trailer is first reported with the load box design as described in Chapter 3. For the sake of brevity only the results of the final concept will be presented here.

Once reasonable stresses are attained for static load cases, the initial fatigue performance of the load box is presented. Changes are proposed to increase the fatigue performance and results from a fatigue analysis incorporating these changes are presented with further comments. The chapter concludes with some general comments and conclusions.

6.2 Description of finite element model

The design was modelled in *Nastran for Windows® 4.5* a product of the *McNeal-Schwendler Corporation* on a PC with an *Intel* 3.0 GHz Pentium4 processor with 1.0 GB of RAM and a 300 GB SATA hard disk. Each analysis used about 30 GB of hard disk space and the model had 2.4 million degrees of freedom. The complete model consisted of 400 613 nodes defining 537 885 elements. A typical static analysis took six hours to complete.

6.2.1 Load box

The Snap 750 design was modelled using shell elements. All material properties were defined as single layer orthotropic laminates with the appropriate thicknesses and care was taken to

properly align the material directions. Material properties that were summarised on page 29 are again presented below. All laminate properties will be evaluated according to the Hill failure criteria. Element size was chosen to fit two elements in the height of the ribs of the Snap 750 System profiles. This dictated a very fine mesh of the complete structure.

Table 17: Pultruded material properties for FE analysis.

Property	**Value**	**Property**	**Value**
E_1	28.2 GN/m^2	G_{12}	2.8 GN/m^2
E_2	6.9 GN/m^2	G_{13}	1.55 GN/m^2
υ_{12}	0.3	G_{23}	1.55 GN/m^2
σ_{UT1}	490 MPa	σ_{UC1}	490 MPa
σ_{UT2}	98 MPa	σ_{UC2}	98 MPa
τ_{U12}	23.4 MPa	σ_{UIL}	36.5 MPa

The trailer was modelled without doors as their structural contribution is small due to play in the hinges and elastic seal between the load box and the doors. The cooling unit was approximated with beams and mass elements. In Figure 21 the Corner 65 sections can be seen in light blue with the Snap 750 side profiles in purple.

Where the elements of the corner sections and the floor sections overlap, the elements of both sections were generated on a single set of nodes but with offset mid-plane stress recovery positions. Nastran allows the user to off-set the mid-plane of a shell element from the plane formed by the nodes used to define it, this method is referred to, in Nastran, as off-set mid-plane stress recovery. This method was also used to join the bottom floor plate and the top flanges of the chassis I-beams. Since, in practice this interface will be joined with structural adhesive and clamps spaced along the length of the trailer, this simplification is valid.

The payload was evenly distributed on the top floor plate elements by means of non-structural mass. Please take note of the definition of the coordinate frame as this will be referred to later.

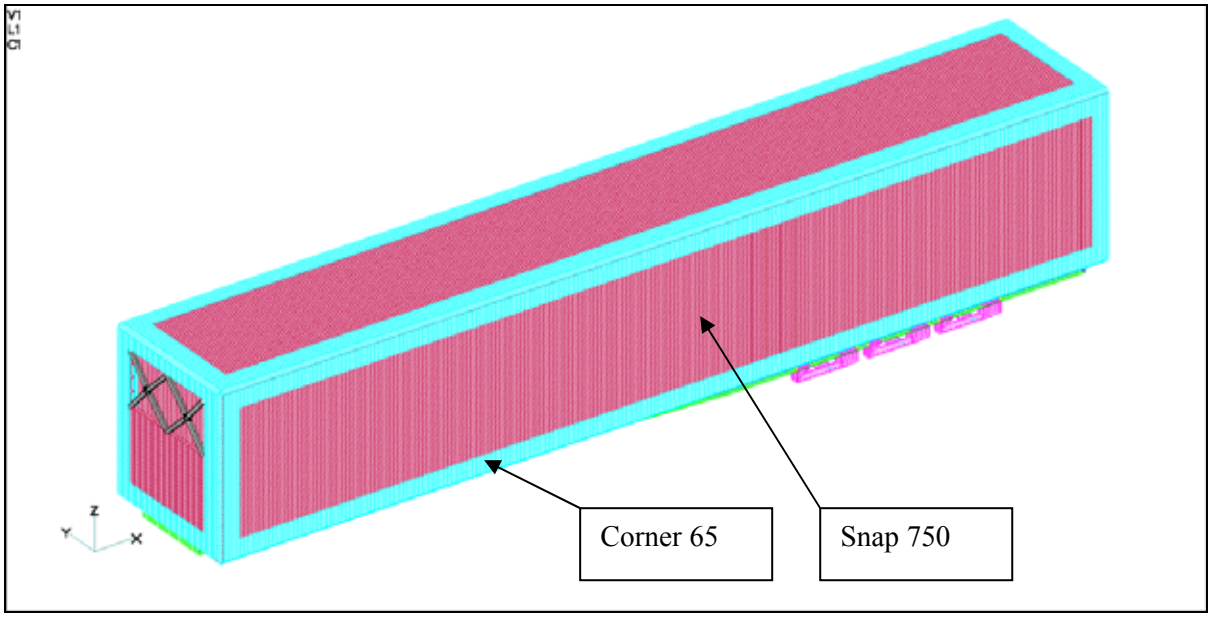

Figure 21: Complete semi-trailer model.

6.2.2 Chassis

The chassis will be made of aluminium and the design was extensively modified from similar steel structures to incorporate solutions to structural problems identified in initial analyses. One of the first design iterations is presented in the appendices to give an idea of the evolution of the design.

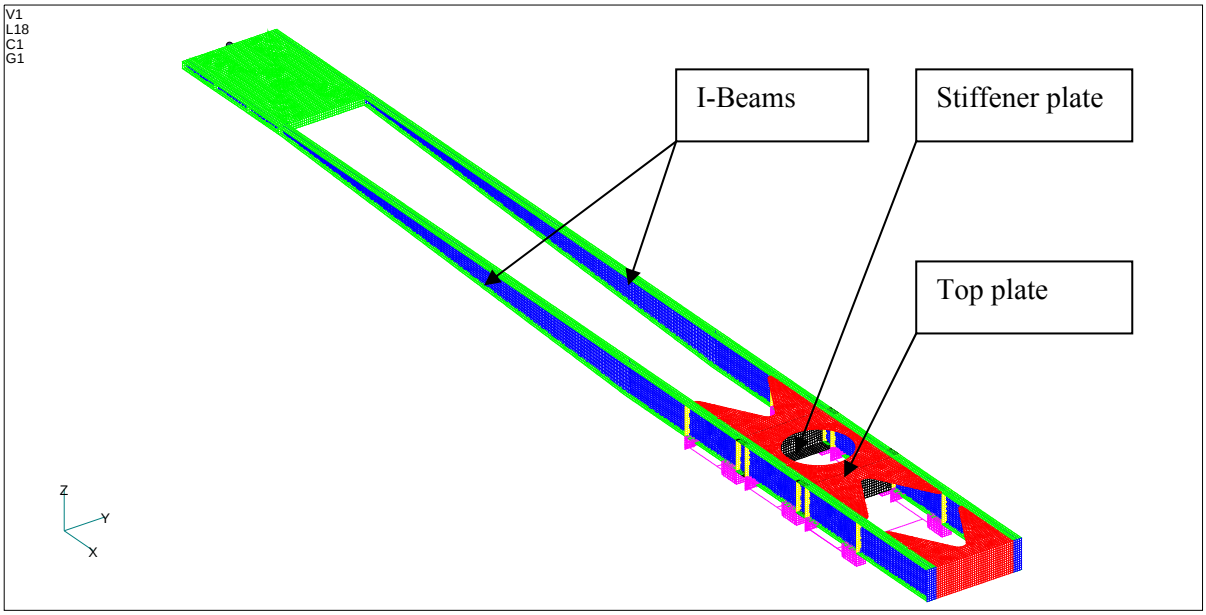

Figure 22: Complete chassis structure.

The chassis is manufactured from two I-beams connected by transverse stiffener plates (shown in black), which provide the torsion stiffness, and the top plate which gives the

chassis transverse shear stiffness. The flanges of the I-beams are 8mm thick with a 5mm web. Vertical web stiffeners were placed on the suspension mounting points to distribute the load between the flanges. The stiffeners can be seen in yellow and is 8 mm thick. Doubler plates were used between the rear web stiffeners to relief high local stresses seen in preliminary analyses. The doubler plates are 5 mm thick and can be seen in black in Figure 24.

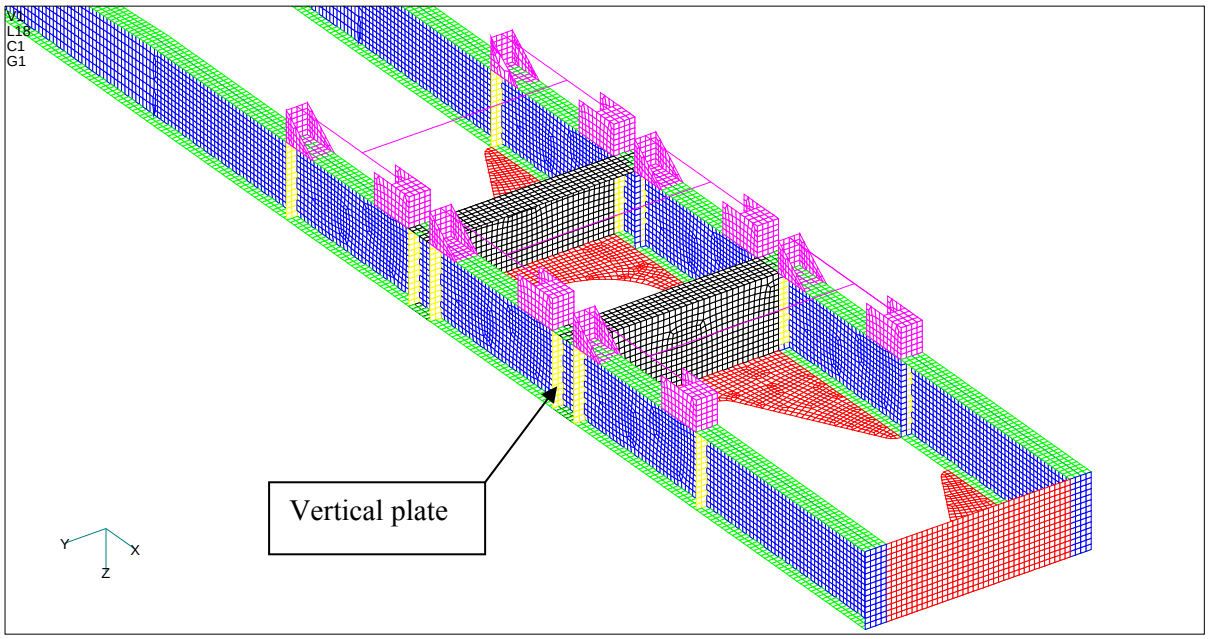

Figure 23: FEM detail of the chassis rear as viewed from underneath.

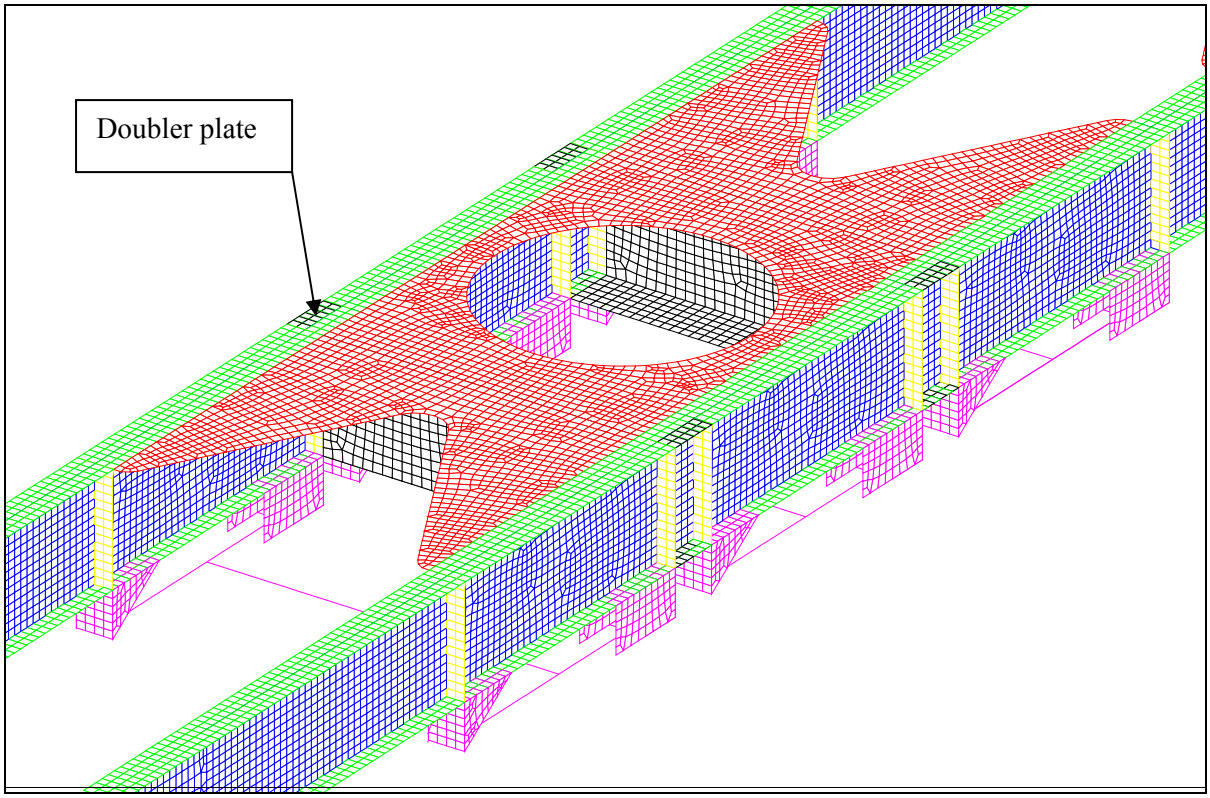

Figure 24: FEM detail of the chassis rear as viewed from the top.

The goose neck is a major structural part. The top goose neck plate is 10 mm thick with internal stiffener plates also of 10 mm aluminium. These stiffeners run longitudinally and transverse to distribute bending loads. The diagonal stiffeners provide torsional stiffness to the goose neck. The bottom goose neck plate is 12 mm thick to reduce the high stresses around the king pin. In production a steel wear plate is usually fitted, this is not included in the FEM as more detail design is needed to determine the actual mounting points. This model with only aluminium plates is considered a worst case scenario and will give a fair indication if such a design is structurally viable.

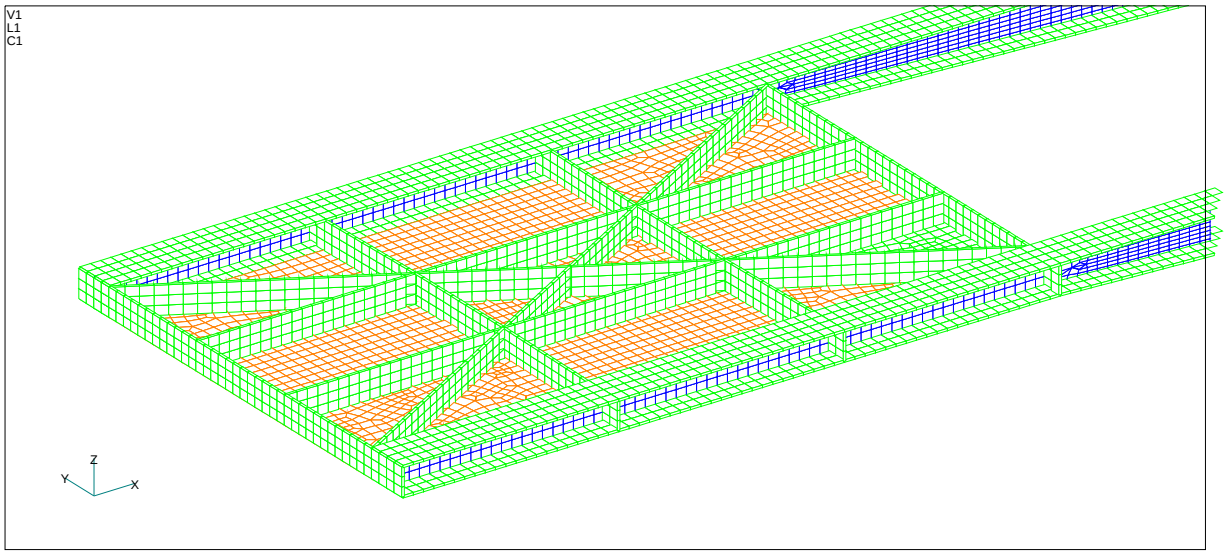

Figure 25: FEM detail of the goose neck with top plate removed.

Preliminary finite element analyses have shown that the low stiffness aluminium is a better combination with the pultruded load box than steel. With a steel chassis the low stiffness composite load box is not strained sufficiently to carry much of the load, resulting in most of the load being carried by the chassis. The aluminium chassis allows the load box to be strained to the extent that it performs as a structural member, a situation that is highly desirable.

Thus decision was made to use aluminium *X-TRAL 728,* which is made by the *Alcan* company, for the chassis construction. This material has a guaranteed 0.2% yield stress of 135 MPa although acceptance testing of new material batches shows a consistent yield stress of 150 MPa.

The change of chassis construction material also reduces the total mass of the trailer. Du Toit (**2000**) has documented a chassis weight of 1507 kg with a load box weight of 4319 kg with a combined total weight of 5826 kg. The pultruded load box with aluminium chassis bring this down to 3563 kg. To this must be added the insulation foam weight and adhesive weight calculated at 301 kg and 180 kg respectively. This gives a reduction of 1782 kg or 30.6%. Running gear is not included in this weight analysis as major improvements have been made in this area since 2000 when Du Toit did his analysis. It must also be said that the pultruded trailer design does not have a rear steering axle which is included in Du Toit's analysis. Additionally there will be trimming and detail added to a production trailer which is not accounted for in the weight calculated from the finite element model. The impact of these

additions on the overall weight of the trailer will not be more than a few percent and a conservative estimate of the increase in payload over Du Toit's trailer will be in the order of 600 kg or 2% which is still good.

6.2.3 Suspension

BPW suspensions are very popular with South African semi-trailer manufacturers. A suitable nine tonne air suspension was chosen from their product range and included in the FE model. The suspension was simplified by modelling the air spring as solid, since the dynamic behaviour of suspension is not under consideration.

Hanger brackets were modelled with shell elements and are a functional copy of the *BPW* design. The foot print of the air spring was used to construct a box which contains a pivot point completing the suspension set-up.

6.3 Load cases and constraints

Six static load cases were applied to the structure. The loads have been discussed in the previous chapter and are listed in Table 15. Three constraint sets were used.

- Normal static describes the conditions when the vehicle is driving on the road in a straight line. The nodes around the king pin which would have made contact with the fifth wheel were held by constraints defined in cylindrical coordinates with the local Z axis coinciding with the global Y axis. Nodes defined in this coordinate frame were allowed to rotate around local Z axis on a fixed radius and were also fixed in Z translation. Constraints on the rear bogies were defined in terms of the global frame of reference. One side of suspension was fixed in Z and Y translation with the other side only fixed in Z translation. All rotational degrees of freedom were left unconstrainted.
- The normal braking constraint set is applicable to analyses concerned with the forces induced during an emergency stop. The king pin constraint was identical to that of the normal static constraint set. One side of the rear bogies were pinned and the opposite side fixed in translation in X and Z.
- To simulate scuffing all rear bogies were fixed in Y and Z translation. The fifth wheel nodes were constrained in global X and Z. The scuffing force of 19941.5 N was then applied at the fifth wheel.

A list of the analyses is presented in Table 18.

Table 18: FEM load cases.

Load Case	**Load**	**Constraint**
1	1 g in +Z	Normal static
2	2 g in -Z	Normal static
3	2 g in -X	Normal braking
4	1 g in +Y	Normal static
5	Scuffing	Scuffing
6	Curb stepping	Normal static

6.4 Static and quasi-static load results

The results from the analyses were evaluated on the basis of material type. All elements with orthotropic material properties were evaluated according to the Hill failure criteria. The following equation shows Hill's failure criteria, where σ_1 and σ_2 are stresses in the principal material directions and τ_{12} the in-plane shear stress. Hill assumes the ultimate tensile and compressive stresses to be equal and hence only the tensile values, σ_{UT1} and σ_{UT2} are used.

$$H_{fe} = \frac{\sigma_1^2}{\sigma_{UT1}^2} - \frac{\sigma_1 \cdot \sigma_2}{\sigma_{UT1}^2} + \frac{\sigma_2^2}{\sigma_{UT2}^2} + \frac{\tau_{12}^2}{\tau_{U12}^2} \quad \textbf{(6.1)}$$

Further the Hill failure index is related to the safety factor (SF) by:

$$SF = \sqrt{\frac{1}{H_{fe}}} \quad \textbf{(6.2)}$$

The Von Mises failure theory was used for isotropic materials.

6.4.1 Load case 1: 1g Positive vertical acceleration

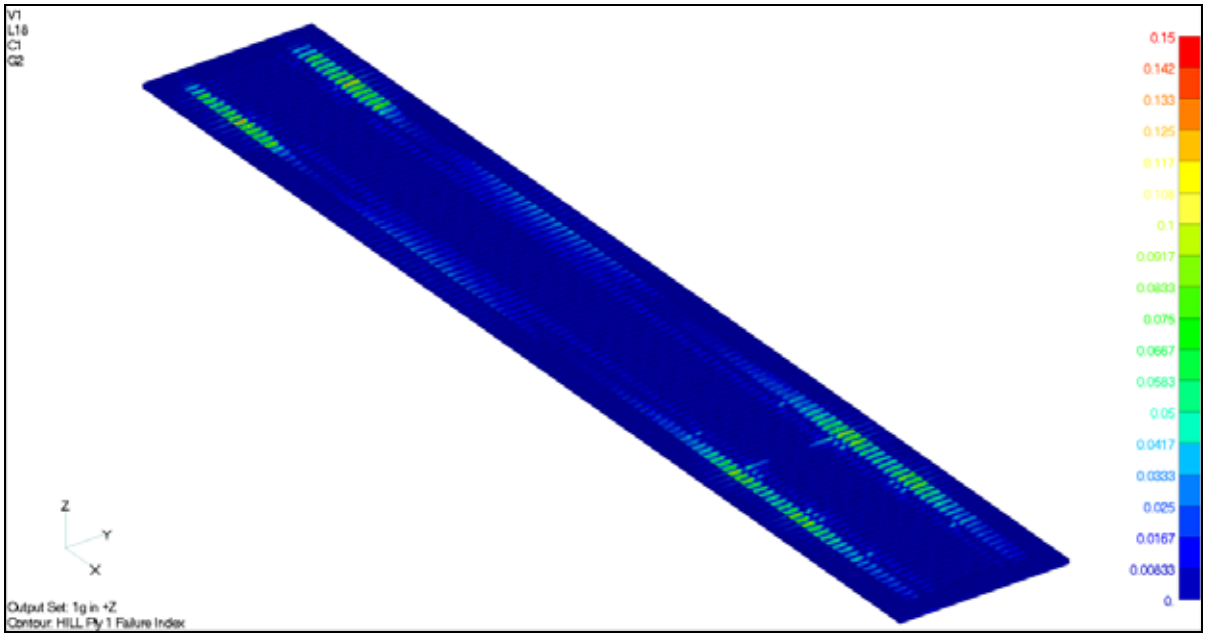

Figure 26: Hill failure index of the pultruded floor webs at 1g in +Z.

Stresses in the composite parts are very low in this load case with a peak failure index of 0.145 in the floor webs. This is caused by the high shear loads at the point where the load box drops of the chassis I-beams.

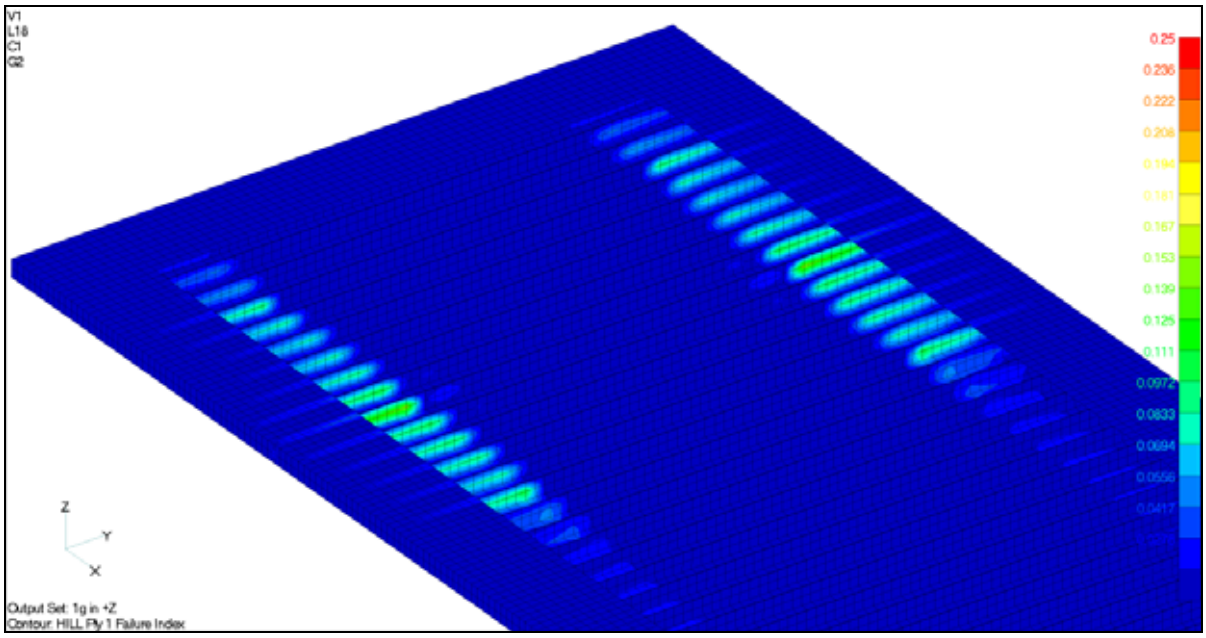

Figure 27: Hill failure index of floor webs at 1g in +Z.

Stresses in the chassis are more pronounced with a peak Von Mises stress of 74.5 MPa shown in the goose neck top plate. Average element stresses of 67.0 MPa are seen at the connection points of the flange stiffeners in the goose neck. Stresses in the rest of the chassis are below 45 MPa.

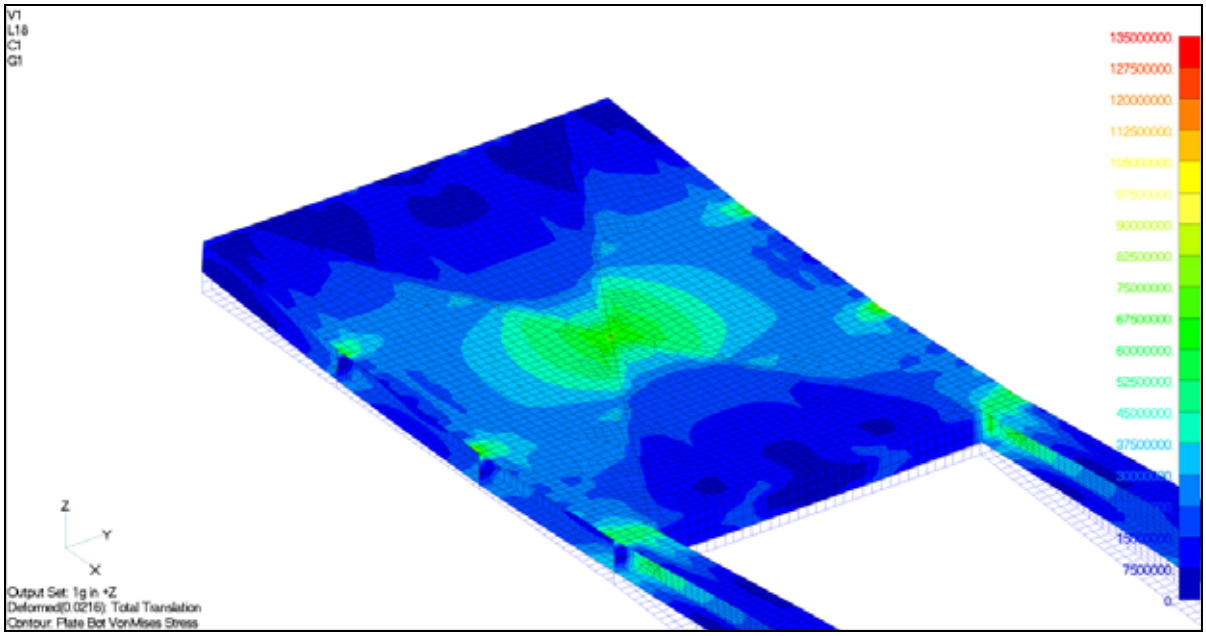

Figure 28: Stresses in goose neck at 1g in +Z.

6.4.2 Load case 2: 2g Negative vertical acceleration

In this load case the structure is highly stressed. Once again it is noted that the webs of the floor is under high shear stress with a failure index of 0.58. The highest stresses occur at the outer edge of the chassis flanges. Which in effect means that the part of the floor outside the I-beams, act as a cantilever, which explains the position of high stress. High stresses also occur on the leading edge of the floor. These higher stresses are the result of a modelling inaccuracy. The nodes on the front plate of the chassis and those on the front edge of the load box are not all joined. The three areas of high stress coincide with positions where the nodes are joined (see Figure 30). In practice the load box and chassis will be fixed together by an adhesive which will distribute the loading properly and hence lower peak stresses will be seen but and higher average which should be at an acceptable level.

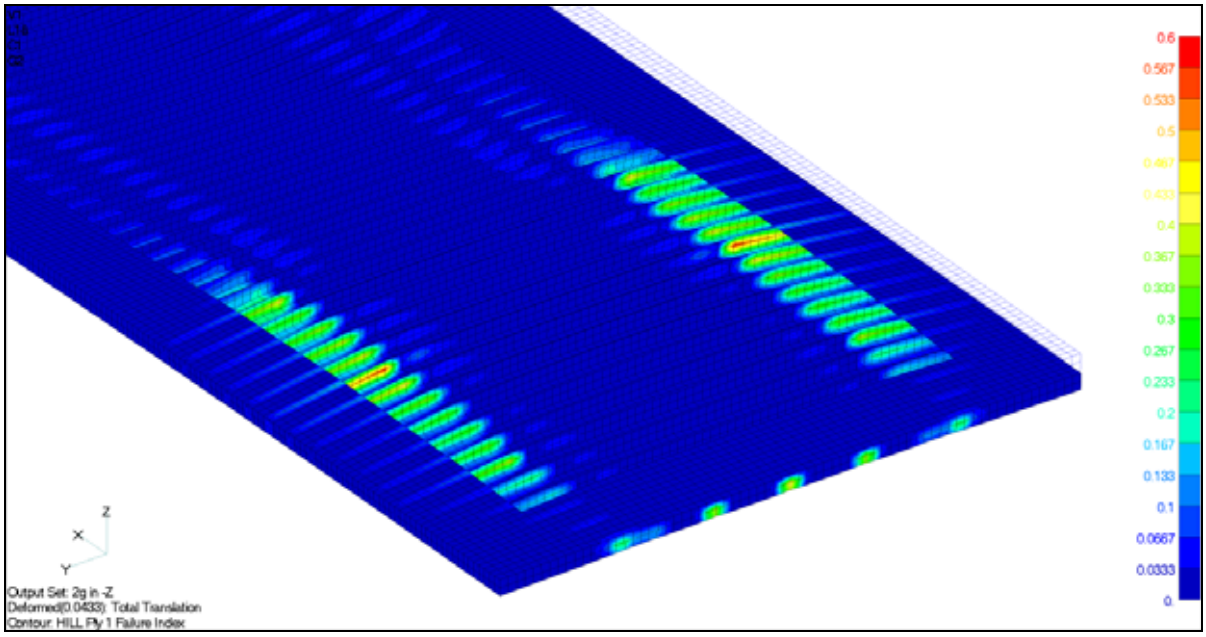

Figure 29: Floor failure index near the front at 2g in –Z.

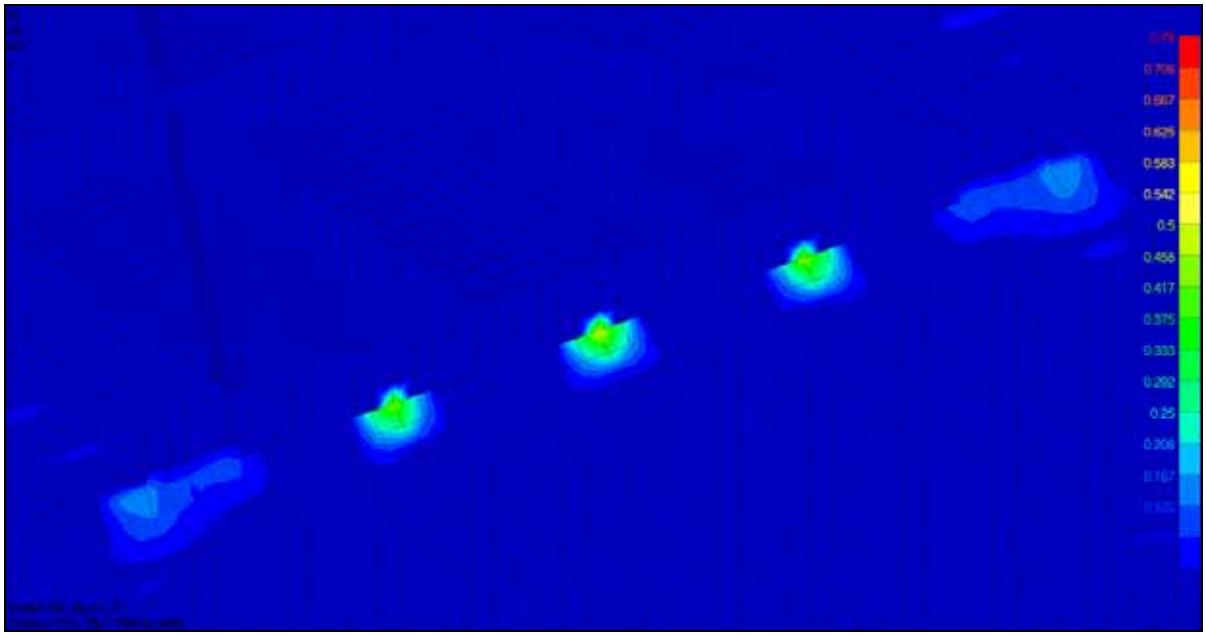

Figure 30: Modelling inaccuracy on the leading edge of the floor.

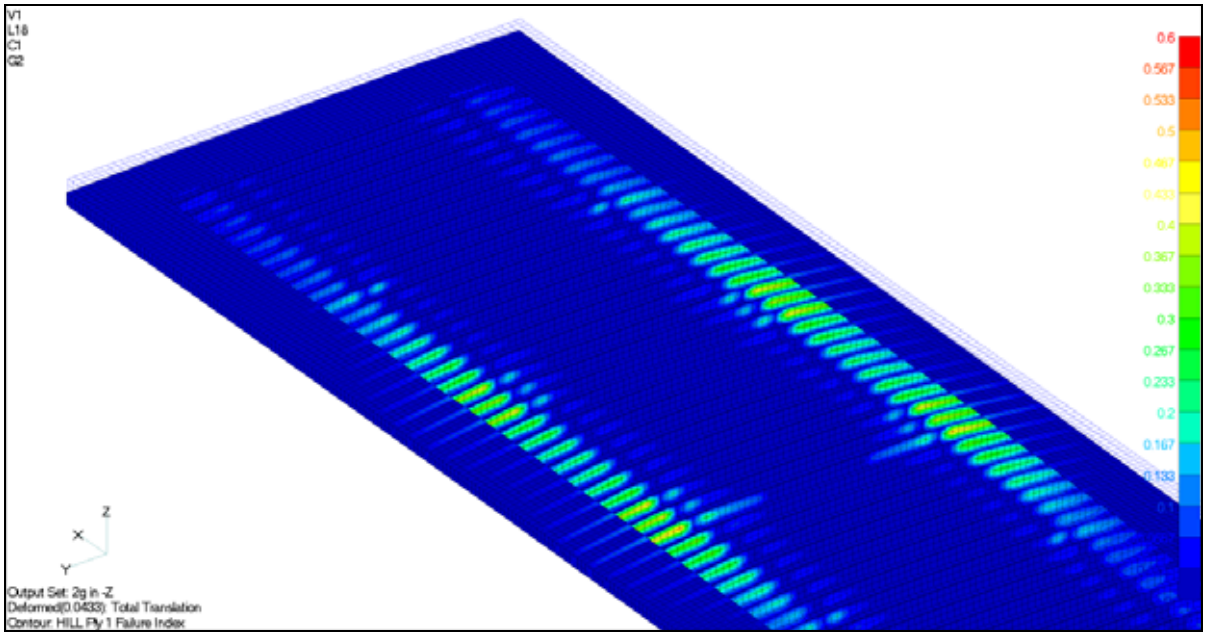

Figure 31: Rear floor failure index at 2g in –Z.

High web stresses also occur at the rear of the composite floor. The highest stress points occur at the positions where the load from the two axles is applied with a failure index of 0.51. This is an acceptably low stress level for a static load case.

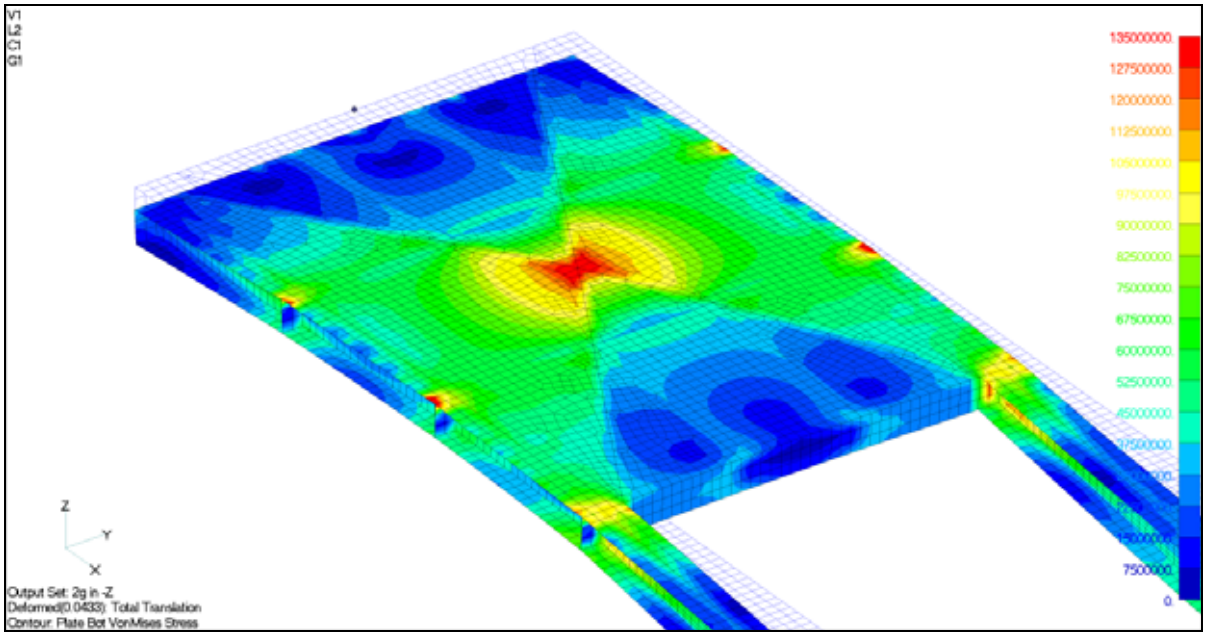

Figure 32: Stresses in the goose neck at 2g in -Z.

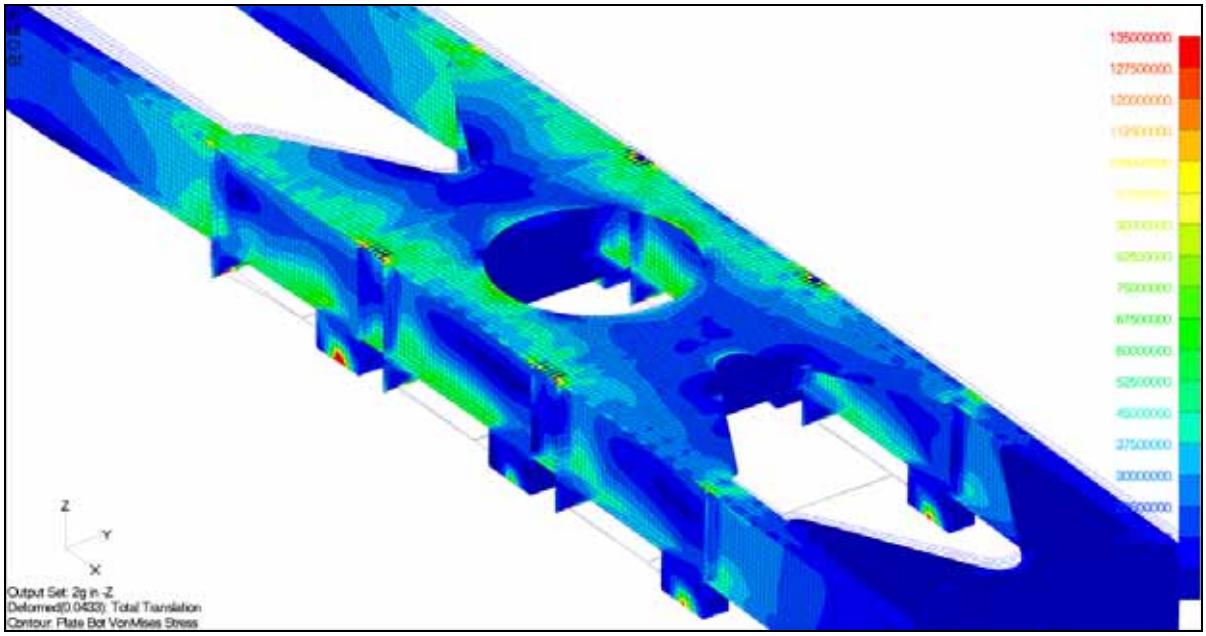

Figure 33: Stresses in the rear of the chassis at 2g in -Z.

Chassis stresses are acceptable in general, but high stresses of 146.7 MPa are generated in the king pin area where the actual king pin will be mounted. Hence the stresses will be lower due to the amount of material added. High stresses also occurred at all web stiffeners, these stresses are quite localised and can be lowered with some detailed investigation. This is included in the recommendation for further development.

6.4.3 Load case 3: 2g Axial acceleration

According to this analysis low stresses are generated during braking. The highest stresses were found at the points where the refrigeration unit is mounted. This model approximate the refrigeration unit with mass elements and beams mounted on only six points. In practice the load is distributed much better and hence the stresses will be lower.

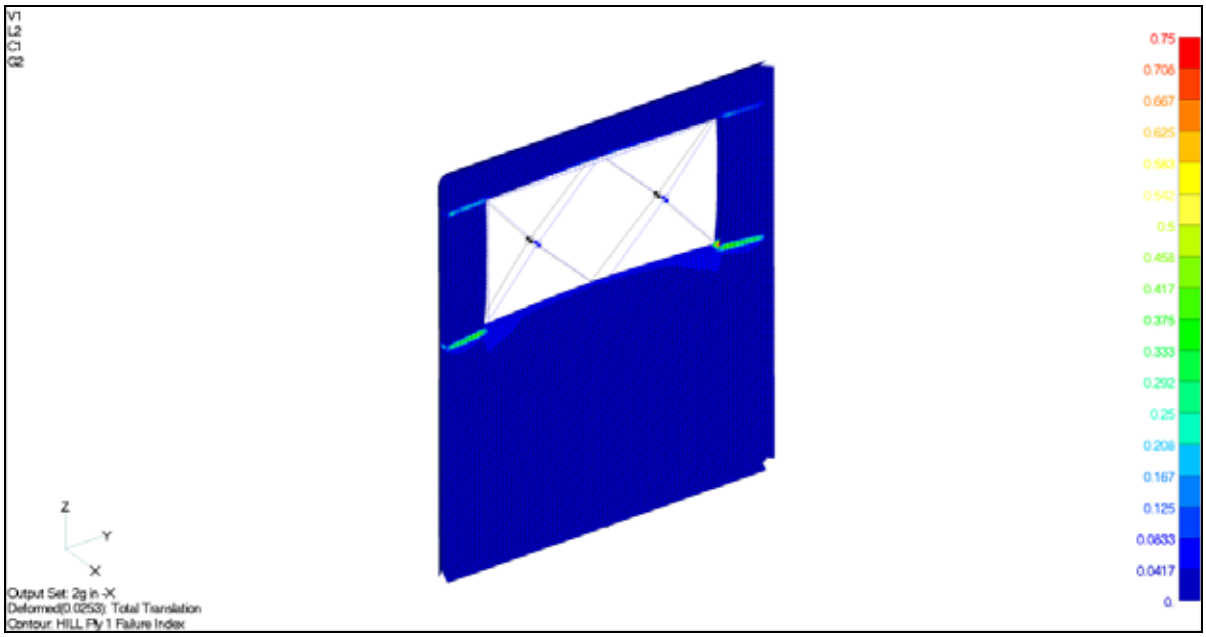

Figure 34: Hill failure index of load box bulkhead at 2g in –X.

Low stresses are generated in the bottom floor plate with a peak failure index of 0.14 where the bottom plate is joined to the chassis.

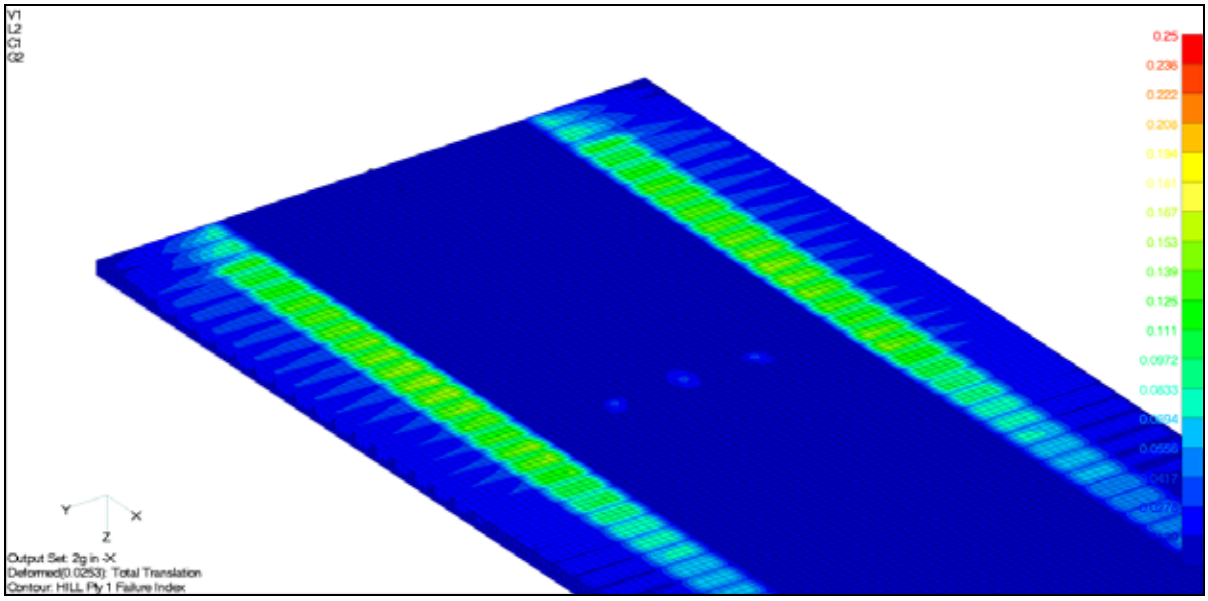

Figure 35: Failure index plot of floor at 2g in -X.

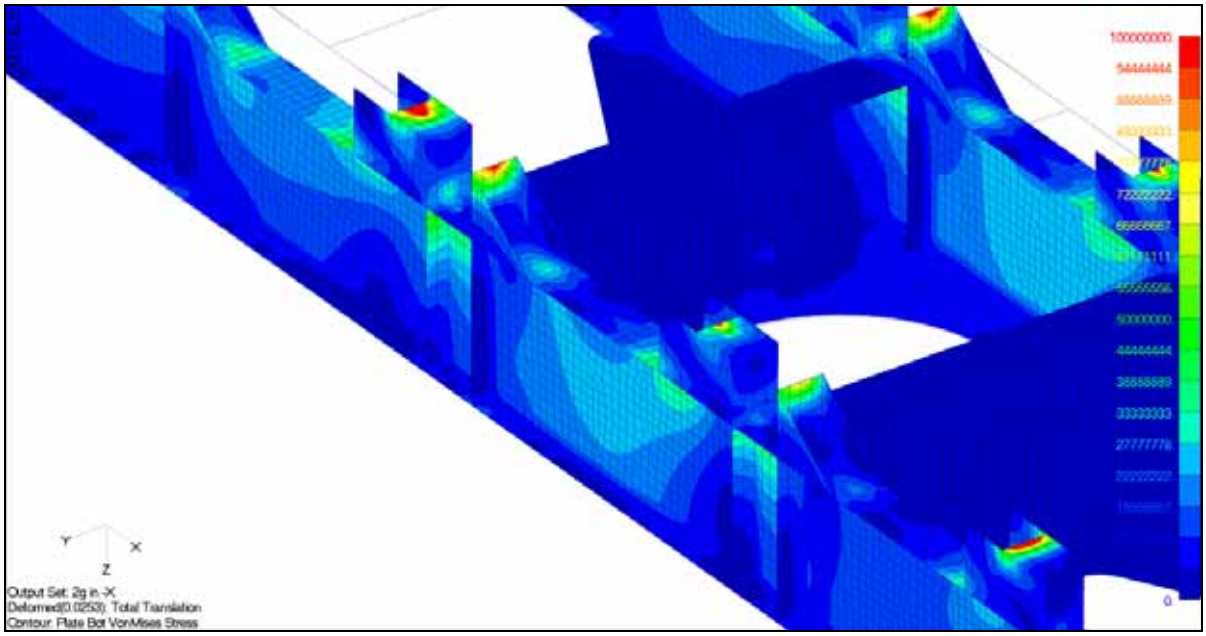

Figure 36: Von Mises stresses in chassis at 2g in -X.

The chassis also performs well in this load case with peak stresses of 58.2 MPa near the bogie mounting points.

6.4.4 Load case 4: 1g Negative transverse acceleration

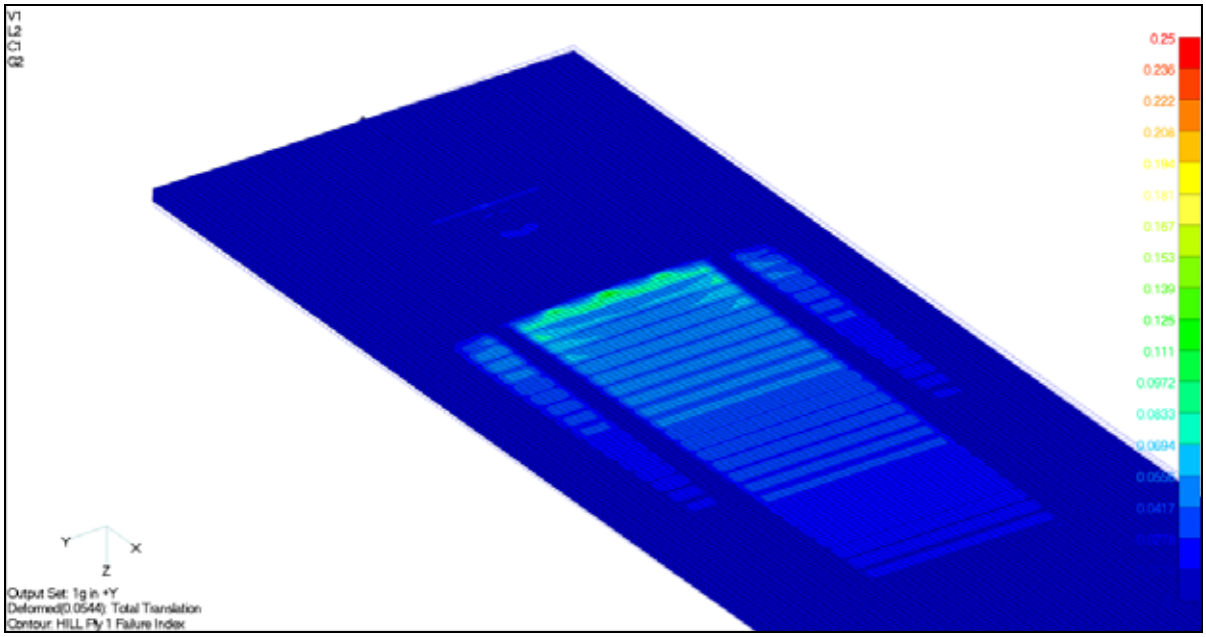

Figure 37: Failure index of the floor for load case 4.

Composite stresses are low with the maximum failure index of 0.18. This can be seen in the bottom floor plate. The chassis stresses are high and the structure will fail at numerous

positions. Torsion of the main I-beam web is the main cause of the high stresses. The highest stresses occur in the web stiffener plates. It is recommended that the web stiffener thickness be increased from 5 mm to 10 mm. Additional analyses have shown that this will lower the stress in the stiffener from 160 MPa to 80 MPa, which is acceptable. A concept that can also be investigated is to box the web stiffener plates. This would alleviate the stresses on both sides of the I-beams. Care will have to be taken as this change may add too much stiffness and cause a stress concentration.

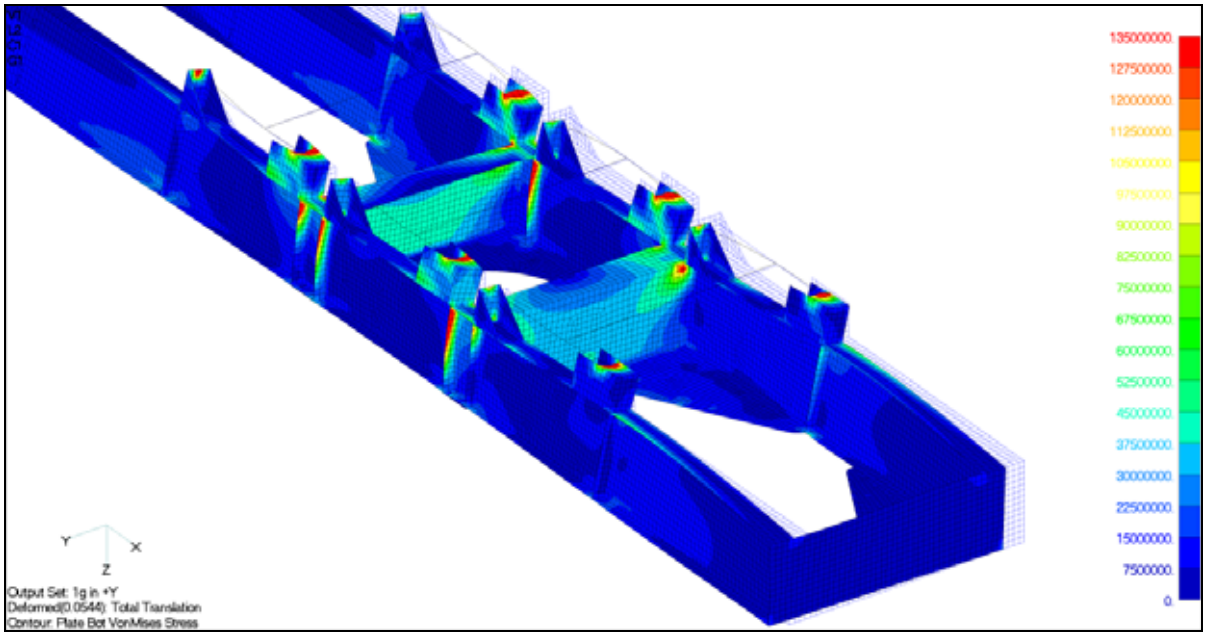

Figure 38: Von Mises stresses in chassis during transverse acceleration.

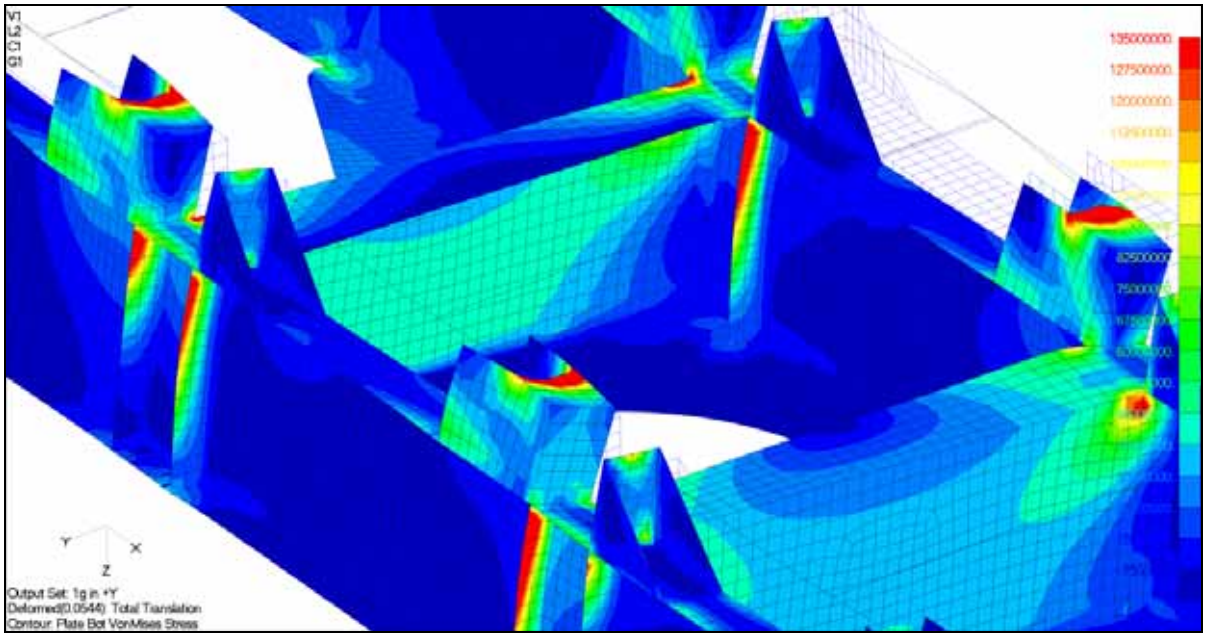

Figure 39: Bottom view of highest chassis stress areas at 1g transverse accelaration.

6.4.5 Load case 5: 19.95kN Scuffing load

Tyre scuffing is also a severe load case and high stresses are generated in the chassis. The load box however is not highly stressed, with a peak failure index of 0.22 found in the floor webs at positions corresponding to the outer hanger bracket mounting points.

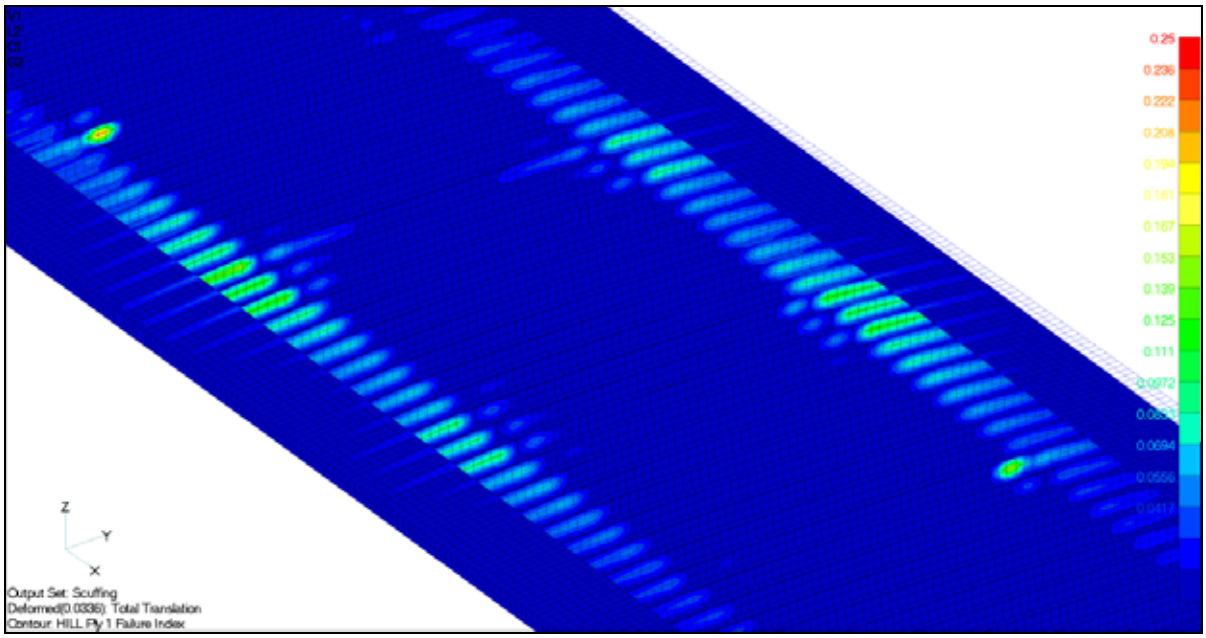

Figure 40: Failure index of composite floor exposed to tyre scuffing.

Stresses in the goose neck exceeded the yield point of the material. A peak stress of 148 MPa is seen in the top plate. It is difficult to satisfactorily explain why the high stresses present themselves in the top plate of the goose neck and not in the bottom plate where the load is applied. The only reason which seems possible is because the constraint set simulates the truck facing in the negative X direction and not in the positive Y direction as it would in practise. However from investigating the high shear stress areas this also does not seem plausible. This matter needs further attention.

High stresses near the bogie mounting points in the transverse stiffening plates are also seen. A peak stress of 166 MPa is caused by high shear loading of the chassis at this point. This problem should be alleviated by thickening of the web stiffener plates.

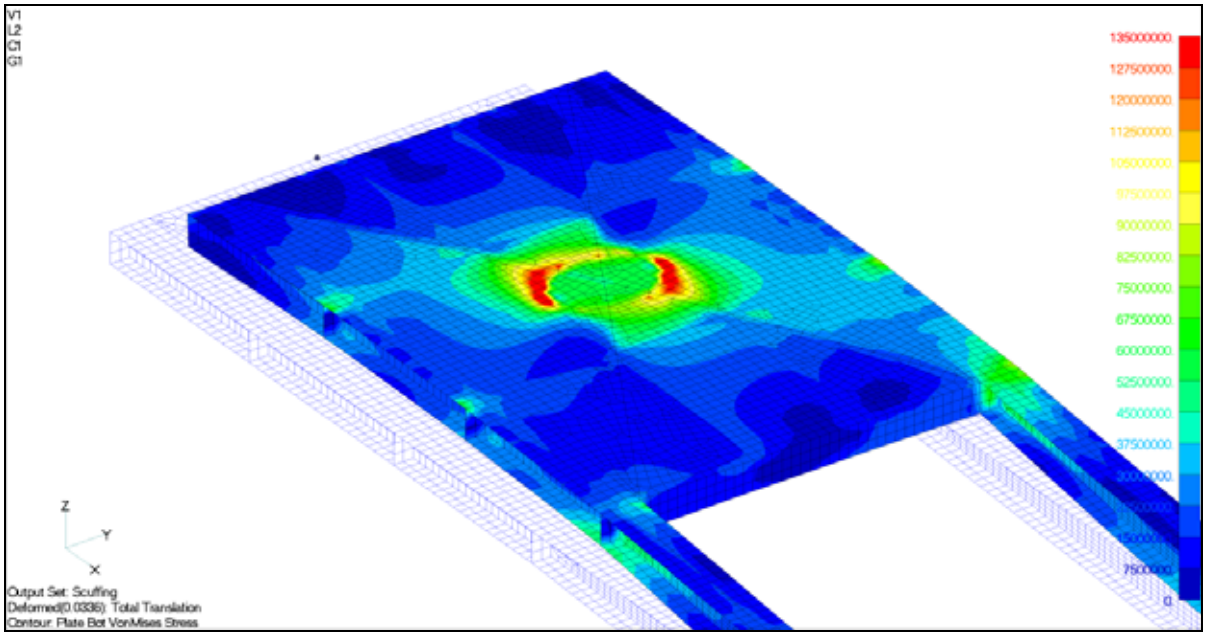

Figure 41: High stresses in goose neck caused by tyre scuffing.

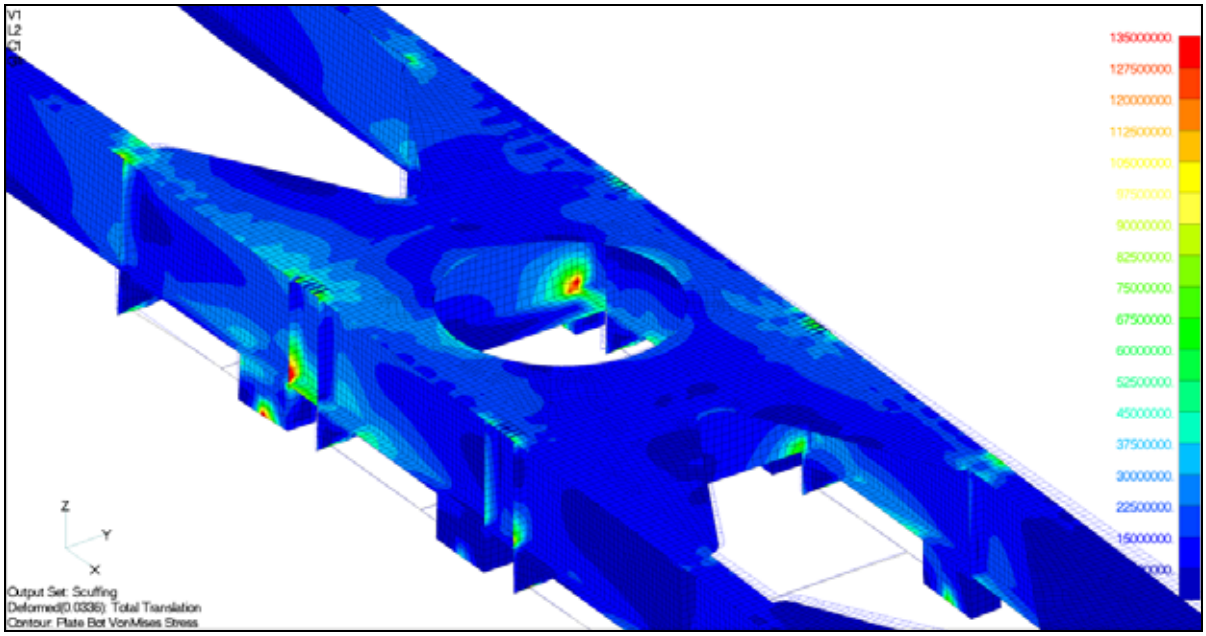

Figure 42: Von Mises stresses in the rear chassis for the tyre scuffing load case.

6.4.6 Load case 6: 50 mm Curb stepping

This torsional displacement load gives the highest stresses in the composite load box. However these stresses are localised giving the impression that they might be caused by constraint forces. These high stresses are caused where the structure is rigidly fixed by the constraints. In practice the fifth wheel is rubber mounted giving a small amount of flexibility in the actual constraint which will relieve the high stresses seen. This flexibility is not included in this FEA model as there is no data available on non-linear stiffness response of the fifth wheel. Hence the stresses at these locations are deemed acceptable.

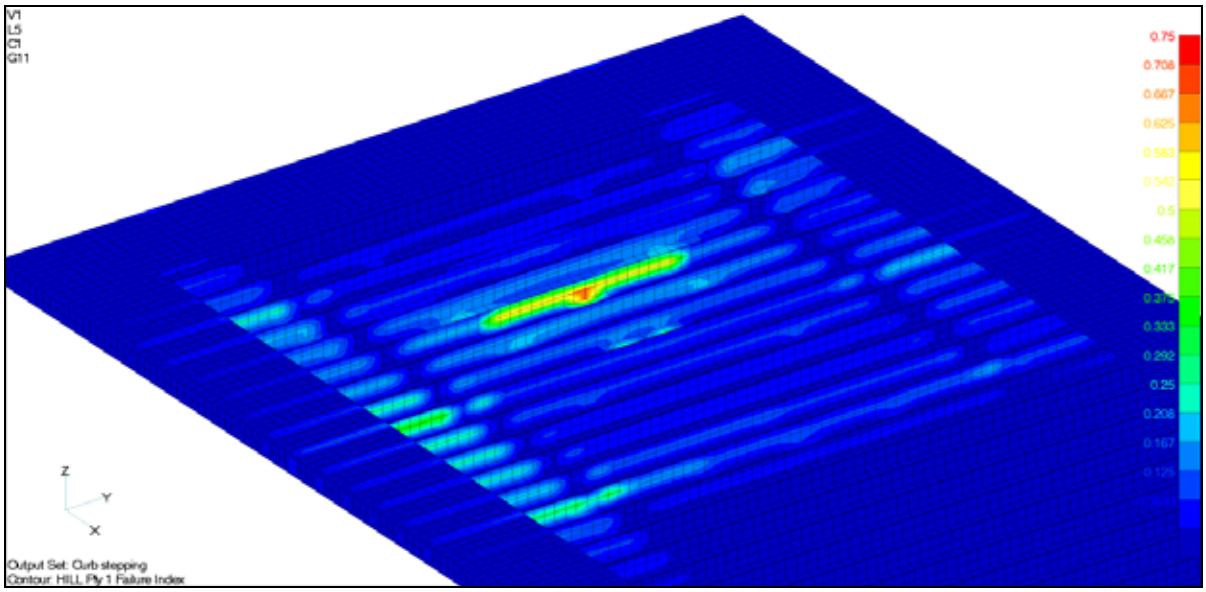

Figure 43: Failure index in the floor webs for torsion load.

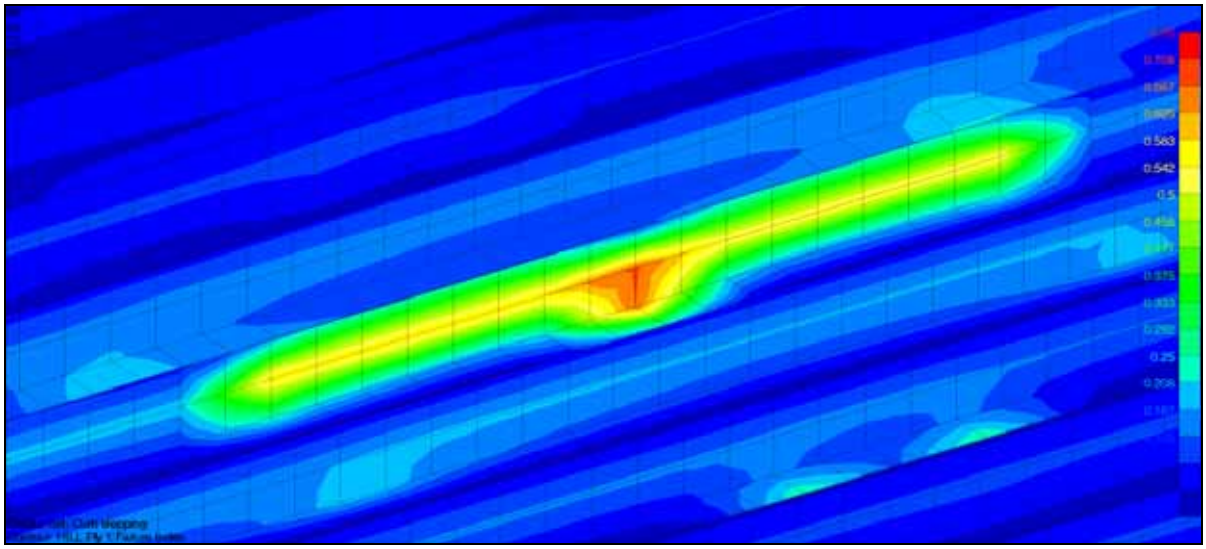

Figure 44: Detail of floor failure index.

Very high stresses of up to 268 MPa are seen in the goose neck. Shear stress load paths are clearly seen in Figure 45. To increase the shear path length it is advised to increase the distance between the axial goose neck stiffener plates. This should distribute the shear loading by exposing more material to a lower average load. Also thicker internal stiffeners can be used, which will lower the stress levels.

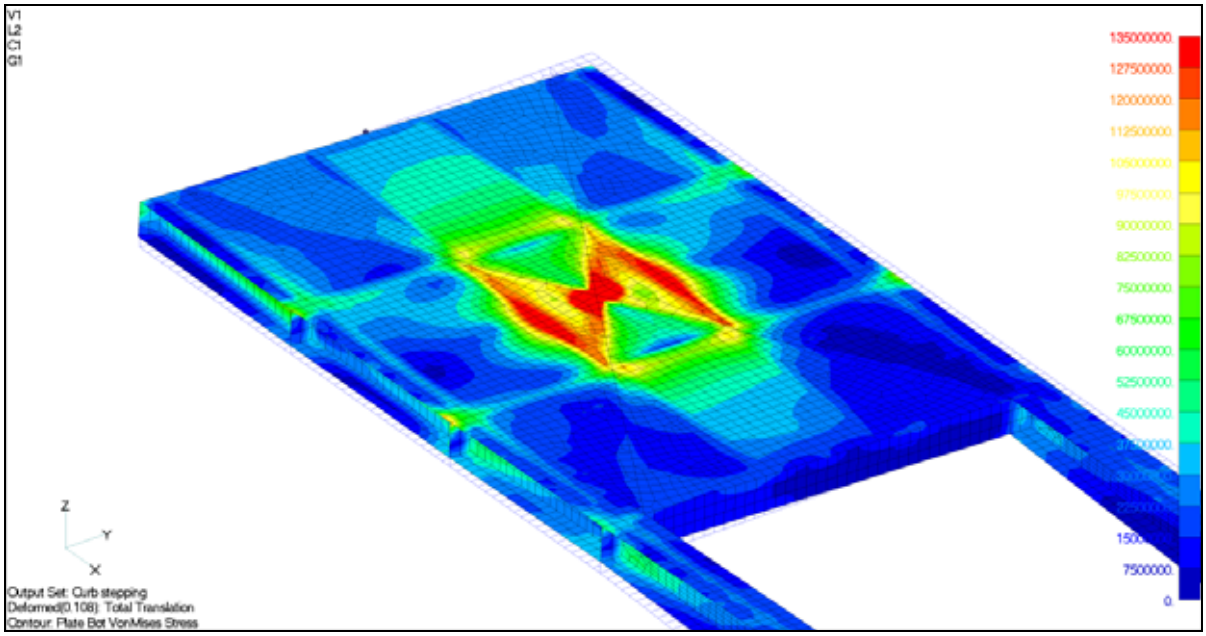

Figure 45: Goose neck stiffener plate stresses for the curb stepping.

Stresses near the bogie mounting point are at an acceptable level and the only area of concern is the web stiffener plates where stresses peak at 118 MPa. These stresses can be lowered with a redesign of the web stiffener plates.

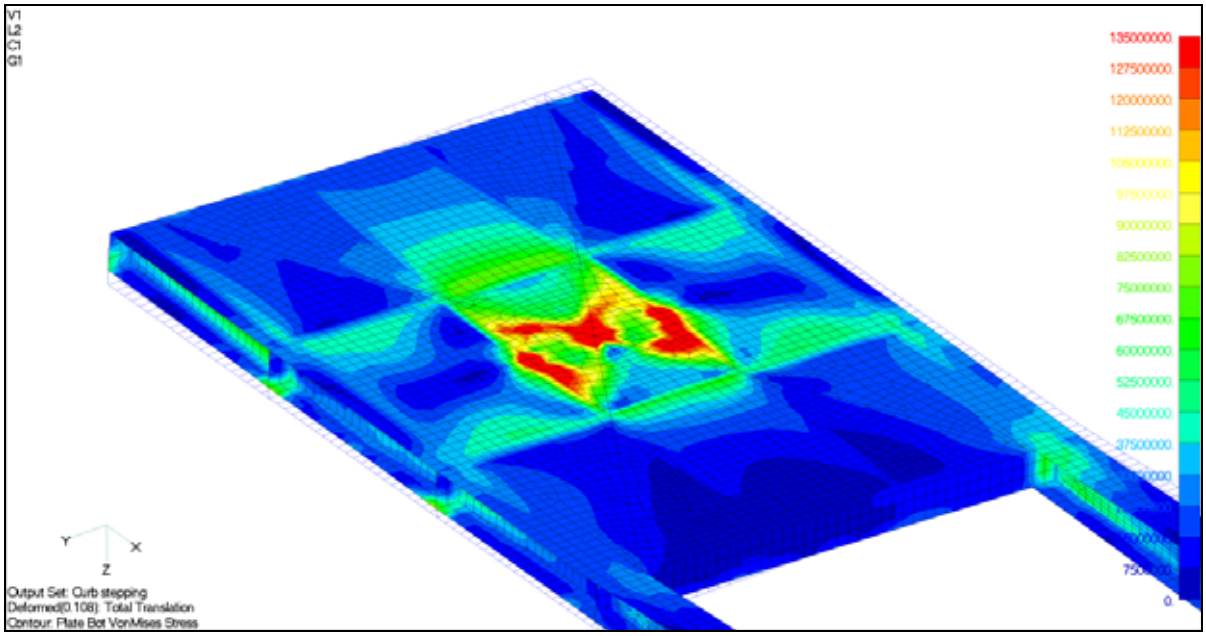

Figure 46: Goose neck bottom plate stresses for the curb stepping load case.

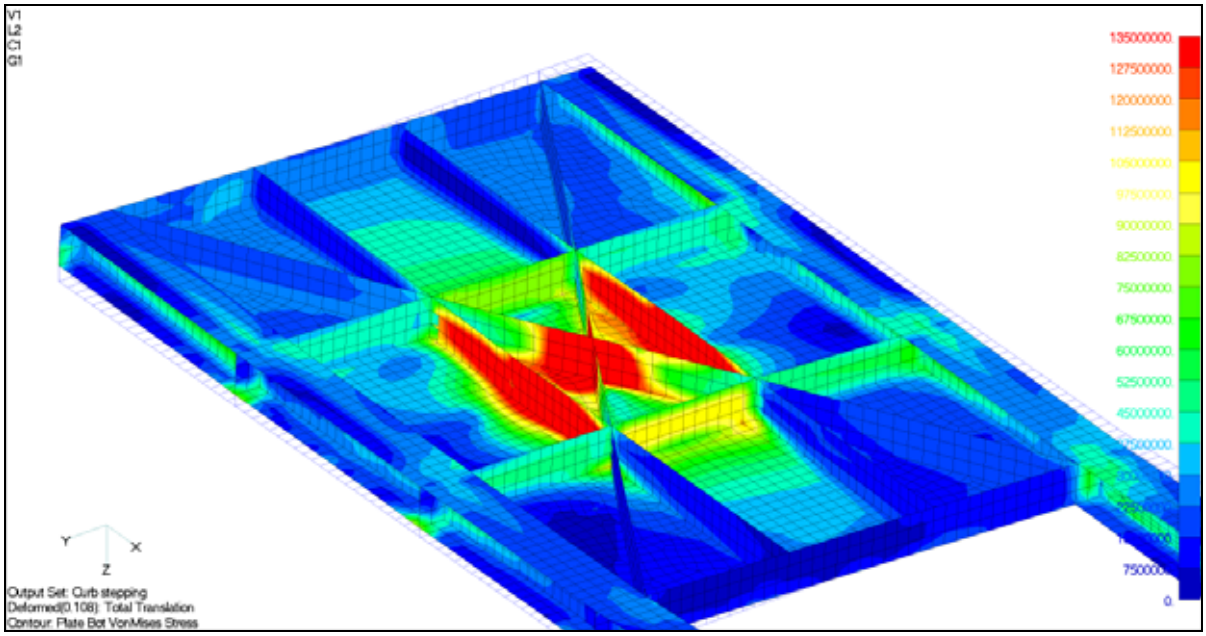

Figure 47: Goose neck stiffener plate stresses for curb stepping load case.

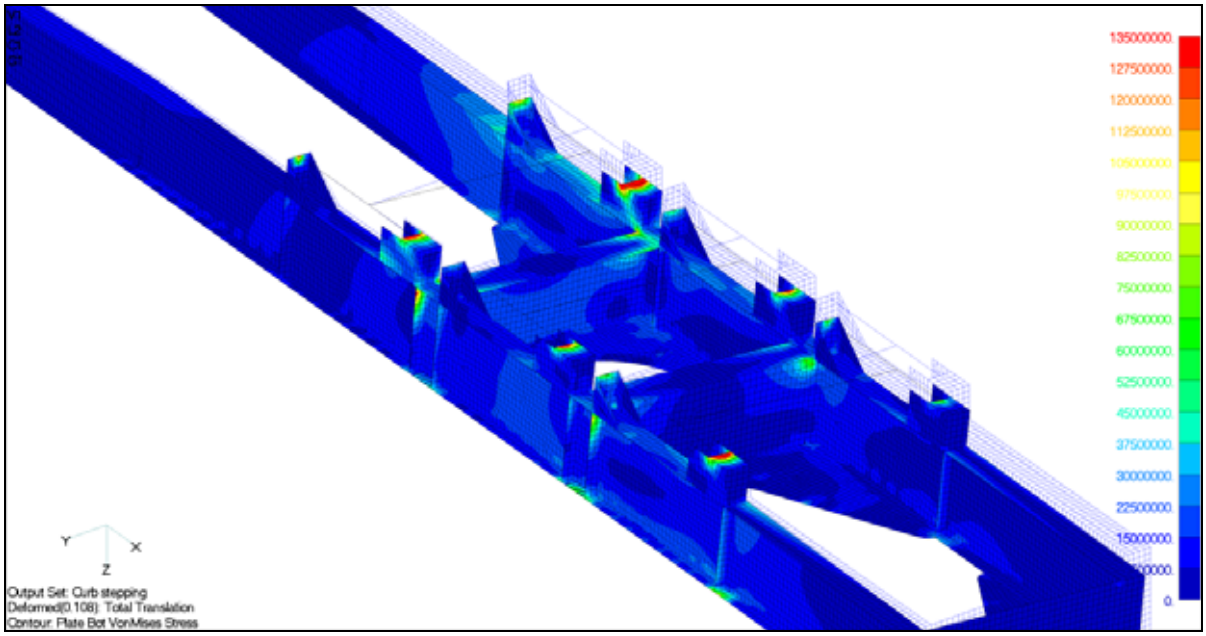

Figure 48: Rear chassis stresses for curb stepping load case.

6.5 Structural critique of the design and proposed solutions

- High stresses occur in the top flange of the main I-beam around the goose neck web stiffeners. Use 5 mm doubler plates to increase the local stiffness of the top flange around the attachment points.
- It is recommended that the rear web stiffener thickness should be increased from 5 mm to 10 mm. Analyses have shown that this will lower the stress in the stiffener from 160 MPa to 80 MPa which is acceptable. A concept that can also be investigated is to box the web stiffener plates. This would alleviate the stresses on both sides of the I-beams but may cause stress concentrations due to a sudden change in stiffness.
- Re-model the goose neck with proper attention given to the detail integration of the king pin. Further specific attention should be given to the gooseneck and load box interface.
- Widen the distance between the axial goose neck stiffeners. Increase the goose neck stiffener thickness to 12 mm.
- Use a higher specification aluminium for instance *Herkal HK34* with a 0.2 percent yield stress of 240 MPa. This material is also made by *Alcan*.

6.6 Fatigue analysis results

A fatigue analysis of the load box was performed. This entailed application of vertical acceleration to the finite element model in 0.2g steps between -1.2g to 1.2g. Each step corresponds to the bin size of the peak count performed to establish the 1000km service vibration load of the semi-trailer. The number of cycles counted in each bin is assigned n_i where i range from 1 to 12 corresponding to -1.2g and 1.2g respectively.

From the FEA data an element was identified with the highest Hill failure index in each of the analyses, we designate it H_{fei}. Evaluation of literature provided no preferred failure criterion for the evaluation of fatigue. Its use here is merely a practical consideration as it has been used for static stress evaluation. The following equation shows Hill's failure criteria, where σ_1 and σ_2 are stresses in the principal material directions. Hill assumes the ultimate tensile and compressive stresses to be equal and only the tensile values, σ_{UT1} and σ_{UT2} are used.

$$H_{fe} = \frac{\sigma_1^2}{\sigma_{UT1}^2} - \frac{\sigma_1 \cdot \sigma_2}{\sigma_{UT1}^2} + \frac{\sigma_2^2}{\sigma_{UT2}^2} + \frac{\tau_{12}^2}{\tau_{U12}^2} \quad \textbf{(6.3)}$$

This index is then equated to the Hill index of a tensile fatigue specimen and the equivalent tensile stress, σ_{1i}, is calculated.

$$\sigma_{1i} = \sigma_{UT1} \cdot \sqrt{H_{fe}} \quad \textbf{(6.4)}$$

The fatigue life N_i at σ_{1i} is determined from the equation (4.10)

$$\frac{\Delta S}{\sigma_{UT}} = -0.0408 \cdot \log N + 0.9528$$

Consequently n_i and N_i were used with Miner's Rule to calculate C_0, the 1000km fatigue life index of the trailer:

$$C_i = \frac{n_i}{N_i} \quad \textbf{(6.5)}$$

$$C_0 = \sum_{i=1}^{12} C_i \quad \textbf{(6.6)}$$

To estimate the total lifetime of the trailer in kilometres the following relation is used:

$$L_t = \frac{1000}{C_0} \quad \textbf{(6.7)}$$

The peak Hill index was predicted in the webs of the floor. This has been the area with the highest Hill failure index in most of the static load cases analysed. This is due to the reasonably high shear stress of 10.7 MPa present in this element, which is about 46 percent of the ultimate shear strength. This corresponds well with the calculated tensile stress with the same Hill failure index of 165 MPa which is 46 percent of the ultimate tensile stress. The good correlation is due to the fact that the element is primarily under shear stress. The following fatigue results are calculated.

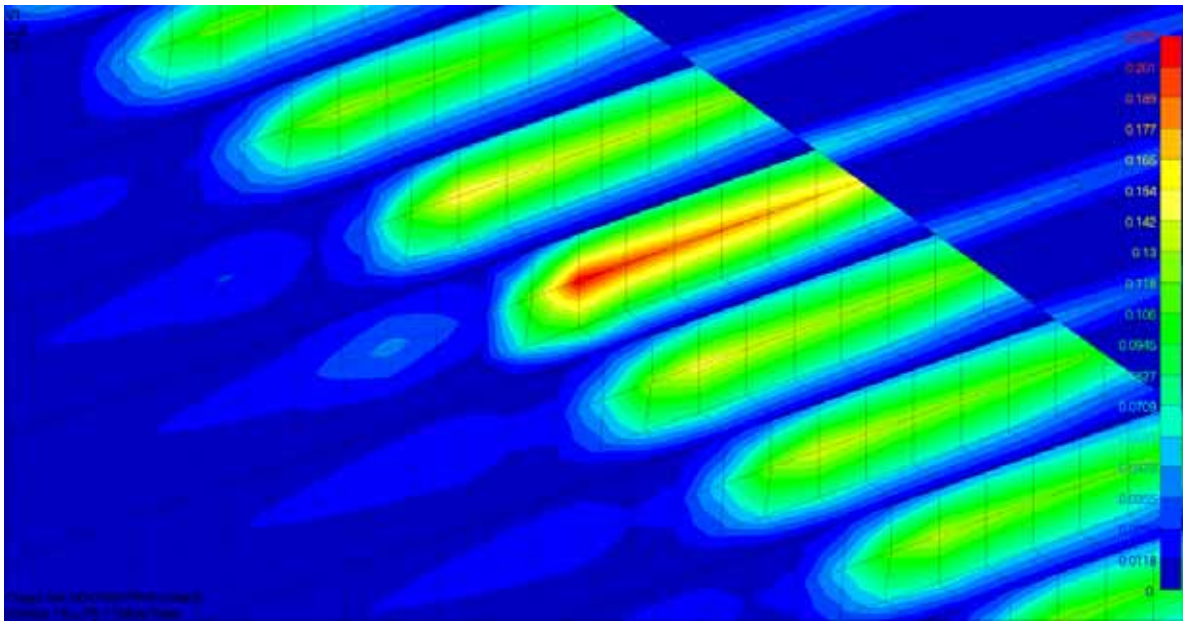

Figure 49: Plot of Hill failure index for 1.2g, vertical acceleration, fatigue load.

Table 19: Initial fatigue life results.

Bin	Vibration level	Failure index, H_{fei}	Equivalent tensile stress σ_{1i} [MPa]	Number of cycles n_i	Fatigue life N_i	Fatigue index C_i
1	-1.2	0.2088	165	14.3E+3	162.7E+3	87.8E-3
2	-1.0	0.145	137	25.2E+3	1.0E+6	24.6E-3
3	-0.8	0.0928	110	75.9E+3	6.4E+6	11.8E-3
4	-0.6	0.0522	82	213.9E+3	40.3E+6	5.3E-3
5	-0.4	0.0232	55	520.8E+3	253.4E+6	2.1E-3
6	-0.2	0.0058	27	1.4E+6	1.6E+9	888.2E-6
7	0.2	0.0058	27	803.1E+3	1.6E+9	504.5E-6
8	0.4	0.0232	55	421.3E+3	253.4E+6	1.7E-3
9	0.6	0.0522	82	197.7E+3	40.3E+6	4.9E-3
10	0.8	0.0928	110	72.0E+3	6.4E+6	11.2E-3
11	1.0	0.145	137	24.0E+3	1.0E+6	23.3E-3
12	1.2	0.2088	165	13.6E+3	162.7E+3	83.6E-3
Total 1000 km fatigue life index						**257.6E-3**

With C_0, the 1000 km fatigue index, the life span of the trailer is calculated.

$$L_t = \frac{1000}{257.6 \times 10^{-3}} \quad \textbf{(6.8)}$$

$$L_t = 3882 \text{ km} \quad \textbf{(6.9)}$$

This is an extremely low mileage for a refrigerated trailer and is unacceptable. Shear stresses in the webs of the floor must be lowered to more acceptable levels and a material with higher shear strength must be used.

A further set of fatigue analyses was performed. Ultimate shear stress was increased to 72 MPa from 23.4 MPa and the shear stiffness to 4.14 GN/m^2 from 2.8 GN/m^2. These values were taken from Agarwal and Broutman (**1990**) for a uniaxial glass reinforced epoxy with a fibre fill fraction of 0.45 and can easily be obtained, in a polyester matrix, with more shear

reinforcement in the webs. The fill fraction is conservative for pultruded composites. Floor web thickness was increased from 3.5 mm to 8 mm. the following results can be reported.

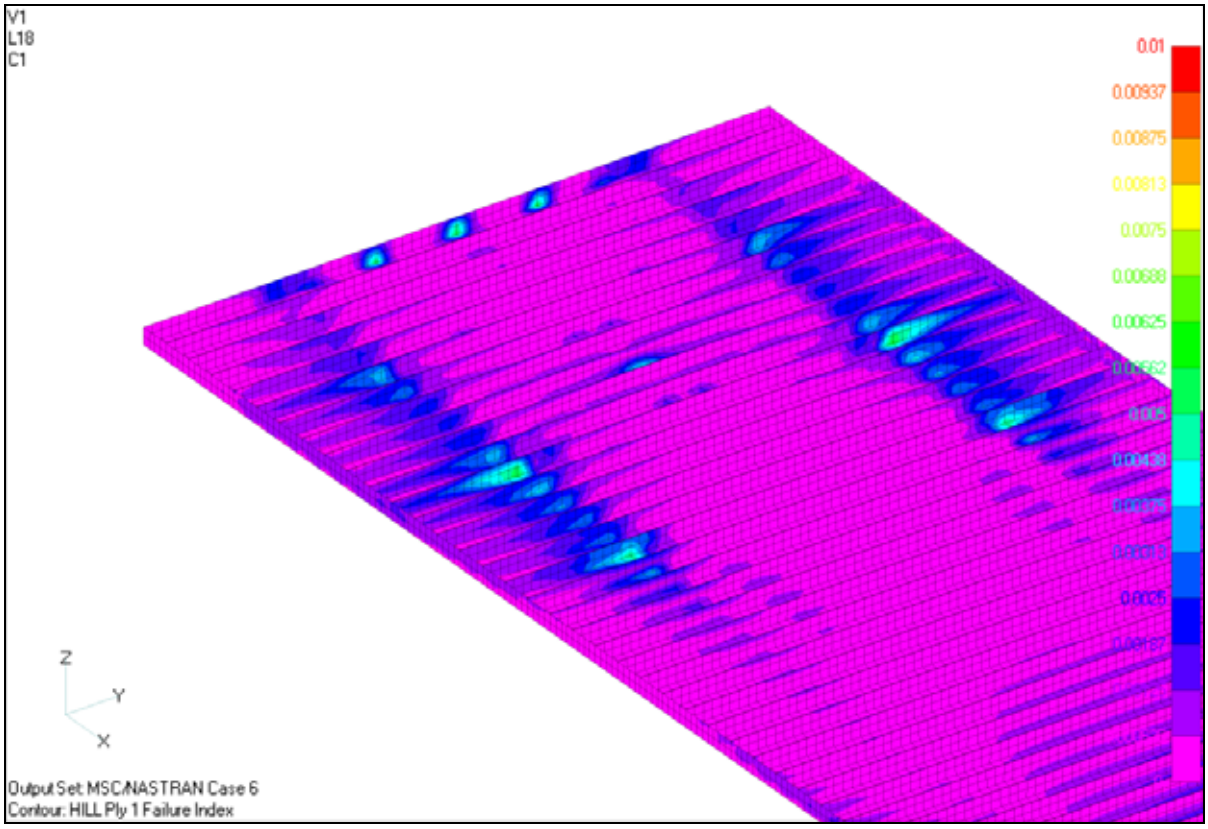

Figure 50: Hill failure criteria for improved fatigue model.

The Hill failure index of the floor webs were lowered considerably to 0.0031 and an equivalent tensile stress of 20 MPa was calculated. The total life time of the load box would be increased to 1.758 million kilometres or 9.16 years which exceeds the desired 8 year life span.

The fatigue performance of the load box is governed by the shear strength of the web of the floor section. It is therefore advised that the shear strength and shear fatigue performance of pultruded composites be qualified in a manner similar to the methods used by Degallaix *et. al*. (**2002**). The use of qualified properties will lead to more confidence in the results of the fatigue analysis.

Table 20: Fatigue performance with adjusted material properties.

Bin	Vibration level	Failure index, H_{fei}	Equivalent tensile stress σ_{1i} [MPa]	Number of cycles n_i	Fatigue life N_i	Fatigue index C_i
1	-1.2	0.0031	20	14.3E+3	2.6E+9	5.5E-6
2	-1	0.0021	16	25.2E+3	3.3E+9	7.6E-6
3	-0.8	0.0014	13	75.9E+3	4.1E+9	18.7E-6
4	-0.6	0.0008	10	213.9E+3	5.1E+9	42.3E-6
5	-0.4	0.0003	6	520.8E+3	6.6E+9	79.1E-6
6	-0.2	0.0001	4	1.4E+6	7.9E+9	180.0E-6
7	0.2	0.0001	4	803.1E+3	7.9E+9	102.2E-6
8	0.4	0.0003	6	421.3E+3	6.6E+9	64.0E-6
9	0.6	0.0008	10	197.7E+3	5.1E+9	39.1E-6
10	0.8	0.0014	13	72.0E+3	4.1E+9	17.8E-6
11	1	0.0021	16	24.0E+3	3.3E+9	7.2E-6
12	1.2	0.0031	20	13.6E+3	2.6E+9	5.2E-6
1000km life						**568.7E-6**
Total life						**1 758 320 km**

Furthermore it was noted that there was a significant distribution change in the contribution to the fatigue damage. This is due to the quadratic nature of the Hill failure criteria, it severely penalises encroachment on the ultimate stress. In this case the high shear stresses are penalised. The interesting feature of this change in distribution is that it shows that the ultimate shear stress can be varied to optimise the fatigue performance of the structure for the load profile. Changes to the ultimate shear stress will also influence the stiffness of the lay-up and hence, the stress distribution at the point in question. Thus, an iterative process will have to be performed in which:

- The lay-up constitution is changed and the ultimate stress and stiffness calculated.
- A finite element analysis is performed to determine the new stress at the point of interest.
- The contribution to the fatigue life is calculated.
- The process is repeated until a linear distribution is achieved over the load profile.

This process will lead to a lay-up optimised for a certain load profile.

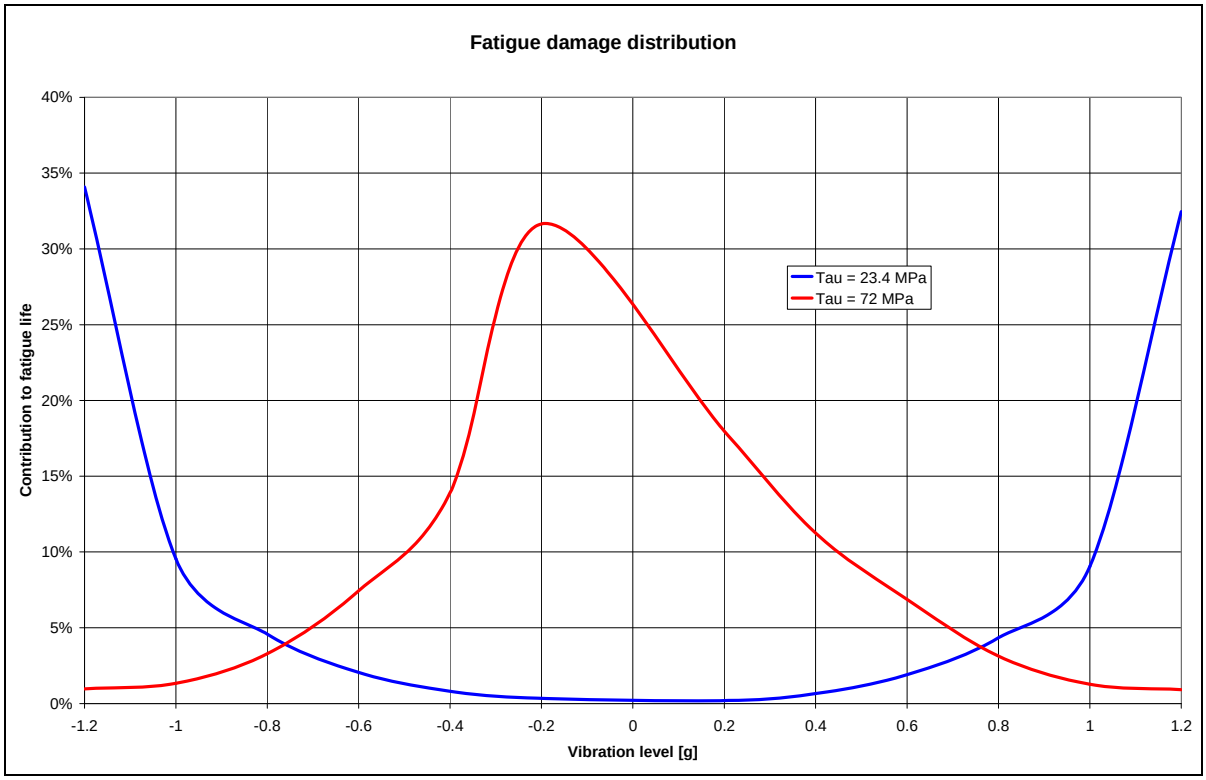

Figure 51: Fatigue damage distribution.

Presented in the Figure 51is a plot showing the contribution to fatigue life by the spectrum of the dynamic load profile. For low shear strength the Hill failure criteria induced high penalties for the high-load, low cycle count, part of the spectrum. However the reverse situation occurs when a high shear strength material is used. In this scenario the major contribution to the fatigue damage is caused by the high cycle count of the low load part of the spectrum. Hence the contribution of each of the bins of the dynamic load profile to the total fatigue damage of the structure can be used as an objective function for the optimisation techniques.

6.7 Conclusion

In this chapter a detail structural analysis of the trailer was performed using the finite element technique. A description of the proposed load box was given and a design for an aluminium chassis was presented. The load cases and constraints for the six static analyses and the fatigue analyses were explained. A short comparison was furnished between the weight of the proposed trailer and one analysed by Du Toit (**2000**). It was concluded that a 2% increase in payload can be realistically expected. Results from the static load cases analyses showed that there is still development that needs to be performed before the design will be ready for production and the necessary changes to the structural design were listed.

Even though the static performance of the trailer was acceptable the fatigue analysis showed great shortcomings in the load box design. High shear stresses in the floor webs were identified which caused a very short fatigue life span of 3882 km. The FEA model was re-analysed with more appropriate material properties and increased web thickness. This caused calculated equivalent stresses to come down to 20 MPa or 4% of the ultimate tensile stress. This resulted in an acceptable fatigue life of 9.16 years which exceeds the desired lifetime of 8 years.

The fatigue life of the trailer is governed by isolated areas of high shear stress. All efforts must be made to relieve the stresses at these points. Also further investigation into the shear fatigue performance of pultruded composites would give more confidence in a fatigue analysis as presented here. It is further postulated that the lay-up sequence can be optimised for a certain fatigue loading profile. This is achieved by changing the lay-up until each part of the load profile contributes equally to the total fatigue life.

Further, in future work efforts must be made to characterise the natural frequencies and mode shapes of the semi-trailer. This will aid in evaluating the dynamic structural performance of the trailer.

Chapter 7 Cost evaluation

7.1 Introduction

There are two facilities in South Africa where these sections can be produced. However, they have limited experience producing advanced structures. If one realistically looks at the available technology one must come to the conclusion that there is much development that needs to be done to mature the technology in South Africa. Especially in the pultrusion die design and manufacturing sector much improvement can be made. Most dies are imported and therefore the cost is very high. The high die cost in turn leads to very little development in the local die manufacturing capabilities.

7.2 Production facility cost

For the purposes of the thesis, two major international pultrusion manufacturers were approached to give budgetary quotes on the delivery of a pultrusion system and costing for the Snap 750 sections.

Table 21: Pultrusion facility cost.

Product description	Creative Pultrusion	Strongwell
Exchange rate Rand to the Dollar	**R 7.50**	
Dies		
Floor	R 1,275,000.00	R 487,500.00
Roof	R 600,000.00	R 487,500.00
Side	R 750,000.00	R 487,500.00
Corner	R 810,000.00	R 150,000.00
Total die cost	**R 3,435,000.00**	**R 1,612,500.00**
Pultrusion Machine	**R 2,522,812.50**	**R 2,625,000.00**
Ancillary equipment	To be advised	R 3,000,000.00
Technology license		
Lump sum	R 1,875,000.00	R 7,500,000.00
Minimum yearly fee	R 187,500.00	To be advised
Duration of agreement (years)	5	To be advised
Total license cost	R 2,812,500.00	R 7,500,000.00
Total facility cost	**R 8,770,312.50**	**R 14,737,500.00**
Cost of Snap 750 profiles		
Floor/m	R 678.83	R 492.13
Roof/m	R 453.68	R 418.31
Side/m	R 515.48	R 442.91
Corner/m	R 381.30	R 196.85
Load box material cost		
Floor	R 33,371.04	R 24,192.91
Roof	R 32,022.20	R 29,525.79
Side	R 60,385.39	R 51,884.65
Corner	R 31,316.93	R 16,167.72
Total load box material cost per trailer	**R 157,095.55**	**R 121,771.06**

To successfully produce these sections in South Africa a transfer of technology would have to take place. This will most probably take the form of a partnership between a company willing to develop this product and one of the pultrusion companies already established. Further, to ensure financial viability of the project, an adequate amount of these sections would have to be produced. Investigation has indicated that an annual sale of 80 trailers is quite attainable.

If the load box is sold for R150 000.00, the current selling price, the total yearly revenue from the sale of 80 load boxes comes to R 12 000 000.00. The actual material cost can be

calculated from the load box weight of 2962 kg and an average fibre fill fraction of 55%. The cost of woven glass products is about R22 per kg and that of polyester about R24 per kg. The raw material cost can now be calculated as:

Table 22: Raw material cost of Snap750 load box.

Component	**Weight of component**	**Component price per kg**	**Cost of component**
Glass	1629kg	R22.00	R35 838.00
Polyester resin	1333kg	R24.00	R31 992.00
		Total material cost	**R 67 830.00**

For a yearly production of 80 trailers the total raw material cost is R5 426 400.00. The labour cost for assembly of the load boxes is estimated at R15 000.00 per trailer or ten percent of the sales price giving a total of R1 200 000.00 on yearly labour cost. This leaves the remainder of R5 373 600.00 for operation of the pultrusion plant, recovery of the capital expenditure and return on investment. If that seems plausible that a capital expenditure of R6 000 000.00, for the dies and the pultrusion plant, should be recovered within the first three years of full production.

This simple calculation should suffice to prove that the financial viability is at least worth exploring further. A more detailed cost and risk analysis will need to be performed. However, these figures are presented to show that the pultruded load box concept is most likely viable.

Chapter 8 Conclusion

The design of a semi-trailer load box using pultruded composites was described in this thesis. This was achieved by listing the areas where improvement is necessary from manufacturing and operational points of view. These shortcomings were addressed with a modular design using pultruded composites with a detail characterisation of the materials used in the design. The loading on the structure was quantified and structural analyses were performed to determine the longevity of the structure.

The current state of semi trailer-design in South Africa was compared to first world countries. Data was presented to show that the refrigerated load box accounts for 38 percent of the refrigerated trailer cost and that 48 percent of labour is spent on it. A reduction in manufacturing cost must be addressed with the new design. Poor durability of the load box is the main operational concern. Multi material construction, fixing between the side wall and floor as well as damage caused by forklifts were listed as the major problems that need to be addressed.

A modular set of pultruded sections were presented with an assembly configuration that increases the design options available to the manufacturer while reducing the manufacturing cost. The new design achieves better joint between the floor and sides and provide a scuffing barrier for forklifts. Only pultruded composites are used which eliminates the problems associated with multi-material construction.

To understand the nature of pultruded composites, the properties of three pultruded materials was explored. The material taken from an 84×35 mm channel section was tested and analysed. Each material used different transverse reinforcement. Tensile moduli ranged between 29.8 GN/m^2 and 35.7 GN/m^2. A comparison was made between the tensile and flexural properties of the flange and web for each material and no preference could be found between the sections.

Further, fibre fill fractions in the flange and web was quantified for the flange and web and separately for the roving and mat reinforcement. The woven reinforcement showed considerably lower fill fractions at 30 percent compared to the 60 percent of the rovings.

Fibre fill data was used with micromechanical and classical laminate theory to give a prediction of the tensile modulus for each material and each part of the section. Poor correlation was achieved with errors of between 8.7 percent and 32.6 percent.

A stress-amplitude versus cycle-to-failure graph was generated for the CFM material from tensile fatigue test data. A strength loss rate of 4.3% per decade was calculated from the data which correlates to the 3-5% found by Kellerman *et. al.* (**2005**). Correlation was also found with the fatigue data of Agarwal and Broutman (**1990**) who represent the data in equation form. Finally some recommendations are made regarding future testing of pultruded composites.

To properly evaluate the structural performance of the refrigerated semi-trailer the operational loads were quantified. These were broken down into static, quasi-static and fatigue loads. Static loads were defined from the trailer and cargo weight. The quasi-static loads were sourced from an European specification concerning the transport of dangerous goods and some additional manoeuvring loads as seen in practise. Finally the fatigue loads acting on trailers were measured and processed to give a histogram of the number of cycles at different vibration levels the trailer is exposed to over a distance of 1000 km.

The loads measured and calculated were used to perform a detail structural analysis of the trailer using the finite element technique. A description of the proposed load box was given and a design for a new aluminium chassis was presented. The load cases and constraints for the six static analyses and the fatigue analyses were explained. A short comparison was furnished between the weight of the proposed trailer and one analysed by Du Toit (**2000**). It was concluded that a 2% increase in payload can be realistically expected. Results from the static load case analysis showed that there is still development that needs to be performed before the design will be ready for production and the necessary changes to the structural design was listed.

Even though the static performance of the trailer was acceptable the fatigue analysis showed great shortcomings in the initial load box design. High shear stresses in the floor webs were identified which caused a very short fatigue life span of 3882 km. The model was reanalysed with more appropriate material properties and increased web thickness. This caused calculated equivalent stresses to come down to 20 MPa or 4% of the ultimate tensile stress.

This delivered acceptable fatigue life of 9.16 years which exceeds the desired lifetime of 8 years.

The fatigue life of the trailer is governed by isolated areas of high shear stress. All efforts must be made to relieve the stresses at these points. Also further investigation into the shear fatigue performance of pultruded composites would give more confidence in a fatigue analysis. It is further postulated that the lay-up sequence can be optimised for a certain fatigue loading profile. This is achieved by changing the lay-up till each part of the load profile contributes equally to the total fatigue life.

Finally an economic breakdown was given of the capital investment needed and the yearly production cost involved in producing 80 load boxes a year. This simple calculation should suffice to prove that the financial viability is at least worth exploring further. A more detailed cost and risk analysis will need to be performed. However figures were presented to show that the pultruded load box concept is most likely viable.

References

Agarwal, B D and Broutman, L J, **1990**, *Analysis and Performance of Fibre Composites*, Second Edition, John Wiley and Sons, Inc, New York

Benham, P P, **1999**, Crawford R J and Armstrong C.G, *Mechanics of Engineering Materials*, Second Edition, Addison Wesley Longman Limited, Essex

Brandt Goldsworthy W, **1990**, *Reinforced Plastics, Pultrusion: Handbook of Plastic Materials and Technology*, Edited by I.I. Rubin, John Wiley and Sons, Inc., New York.

Davalos, J F, Salim, H A, Qiao, P, Lopez-Anido, R, Barbero, E J, **1996**, *Analysis and Design of Pultruded FRP Shapes under Bending*, Composites Part B 27B (1996) 295-305, Elsevier Science Ltd

Degallaix, G, Hassaı¨ni, D, and Vittecoq, E, **2002**, *Cyclic Shearing Behavior of a Unidirectional Glass/Epoxy Composite*, International Journal of Fatigue 24 (2002) 319–326, Elsevier Science Ltd

Du Toit, J F, **2000**, *The Design evaluation and Redesign of a Refrigerated Semi-Trailer Structure using the Finite Element Technique*, Masters Thesis, University of Stellenbosch, 2000

Herakovich, C T, **1998**, *Mechanics of Fibrous Composites*, John Wiley and Sons, Inc, New York

Lahey, R S, Miller, M P, and Reymond, M, **1995**, Editors, *MSC/NASTRAN Version 68 REFERENCE MANUAL*, The MacNeal-Schwendler Corporation, Los Angeles

Liao, K, Schultheisz, C R, Hunston, D L, **1999**, *Long-Term Environmental Fatigue of Pultruded Glass-Fiber-Reinforced Composites under Flexural Loading*, Journal of Fatigue 21 (1999) 485–495, Elsevier Science Ltd

Kellerman, T, Tirelli, T, Zhou, A, **2005**, *Tensile Fatigue Performance of Pultruded Glass Fibre Reinforced Polymer Profiles*, Composite Structures 68 (2005) 235-245, Elsevier Science Ltd

Shigley, J E and Mischke, C R, **1989**, *Mechanical Engineering Design*, Fifth Edition, McGraw-Hill, New York

Strydom, O J, **2002**, *The Feasibility of Pultruded Composites as Construction Material for Refrigerated Trailers,* Final year project, University of Stellenbosch, 2002

Swanson, S R, **1997**, *Introduction to Design and Analysis with Advanced Composite Materials*, Prentice Hall, New Jersey

Tsai, S W, **1988**, *Composites Design*, Fourth Edition, THINK COMPOSITES, Dayton

Appendix A Side impact tests.

An investigation was done to cultivate a better understanding of the use of the materials currently employed in trailer sides. This involved impact tests on side wall constructions.

A comparative study was done to determine the impact strength of three refrigerated semi-trailer side wall designs. The major mode of failure of trailer sidewalls is damage caused by forklifts used during loading and unloading of the cargo. In these cases either the edge of a pallet or the tip of the fork penetrates the fibreglass inner skin of the trailer. Thus the designs were compared by dropping a simulated forklift tip onto them and evaluating the level of penetration.

A.1 Test set-up.

The simulated forklift tip was made of a six millimetre thick washer with a diameter of 117 mm (see Figure 53). This was connected to a steel rod which brought the mass of the indenter to 7.75 kg. The indenter was subsequently suspended, by means of a nylon rope, and dropped onto the specimen from a measured height (see Figure 52).

Care was taken to prevent the indenter from bouncing, as the secondary impact may vary and cause skewed results. The indentation was photographed and the results are compared in the following section. The drop height ranged from 500 mm to 800 mm.

Figure 52: Test Set-up.

Figure 53: Indenter and test specimen.

A.2 Test Results.

Table 23: Impact test results 500 mm.

Inner skin lay up	Drop Height	Comments
2×450gsm CSM 4 mm Plywood	500 mm	Slight indentation, some visible damage to the skin. Damage local with no damage further than a 50mm radius.
2x450gsm CSM 6 mm Plywood	500 mm	Slight indentation, some visible damage to the skin. Damage local with no damage further than a 50mm radius.
300gsm CSM Woven Roving 300gsm CSM	500 mm	Slight indentation, moderate visible damage to the skin. Damage local with no damage further than a 25mm radius. Force distribution limited.

Table 24: Impact test results 600 mm

Inner skin lay up	Drop Height	Comments
2×450gsm CSM 4 mm Plywood	600 mm	Slight indentation, some visible damage to the skin. Damage local with no damage further than a 50mm radius.
2×450gsm CSM 6 mm Plywood	600 mm	Slight indentation, some visible damage to the skin. Damage local with no damage further than a 50mm radius.
300gsm CSM Woven Roving 300gsm CSM	600 mm	Penetration of the skin and foam. Layers of the skin torn. Damage very local.

Table 25 Impact test result 700 mm

Inner skin lay up	Drop Height	Comments
2×450gsm CSM 4mm Plywood	700 mm	Penetration of the skin. Damage more spread out. Foam does not seem to be penetrated.
2×450gsm CSM 6 mm Plywood	700 mm	Partial penetration of the skin. Impact was well distributed. No penetration of the foam.
300gsm CSM Woven Roving 300gsm CSM	700 mm	Penetration of the skin and foam. Layers of the skin torn. Damage more spread out.

Table 26 Impact test results 800 mm

Inner skin lay up	Drop Height	Comments
2×450gsm CSM 4mm Plywood	800 mm	Full penetration of the skin. Ply board also seems damaged, further investigation needed.
2×450gsm CSM 6mm Plywood	800 mm	Full penetration of the skin. Ply board also seems damaged, further investigation needed.
300gsm CSM Woven Roving 300gsm CSM	800 mm	Full penetration of the skin. Damage still very local. Easy to repair.

From the figures it can be seen that the 6 mm plywood lay-up, currently used, offers the best resistance to the impact loads. The force is distributed very well by the ply wood. However, the 4 mm plywood reinforcement delivers virtually identical performance. If a failure of the

wall is defined as, penetration of the skin, then the 4mm ply compares quite favourably with the 6 mm ply.

The specimen with woven roving reinforcement does not offer the same level of impact resistance. To absorb impact loads there must be a mechanism to absorb or distribute the energy. This is usually achieved by either plastic or elastic deformation of the structure. In the previous cases, the wood absorbed the impact by cell collapse and the partial distribution of the force to a large area of underlying foam for absorption by elastic deformation. With only fibreglass skins the force is not distributed well, because the normal plane stiffness of thin membranes is too low, and hence all the energy is absorbed by fracture of the glass fibre skin. These tests are a little crude to put a percentage to the performance of the specimens. But will suffice as a first iteration design comparison.

Appendix B Floor Beam Bending Tests

A comparative study was done to determine the relative bending strength of three proposed trailer floor beams. This was done by subjecting specimens to a four point bending test and measuring the maximum bending moment sustained. The beams tested were a S.A. pine beam with a cross-section of 85×32 mm, a Saligna beam with an 85×32 mm cross-section and a composite beam which measured 80×80 mm. The composite beam is made of wood, steel, poly-urethane foam and glass fibre reinforced polyester and is the design which is currently used in the manufacture of refrigerated trailers floors.

B.1 Test set-up.

As stated the beams were tested in the four point bending configuration, the force was applied by servo controlled hydraulic actuator and measured by means of two 5 t HBM Z6 load cells on which the specimens rested. The displacement was measured with a HBM 500WA LVDT and all the measurements were sampled with a HBM Spider 8. The reason for choosing the four point bending test, instead of the three point variant, is the fact that a constant bending moment is applied over the section of the beam between the two points of load application. It is therefore easier to expose weak areas or defects in the beam. In the three point bending test, the moment is a maximum at the mid point and failure usually occurs at this point. One can therefore extract more information from the four point test than the three point test. The bending arm was 500 mm for all the beams, see Figure 54.

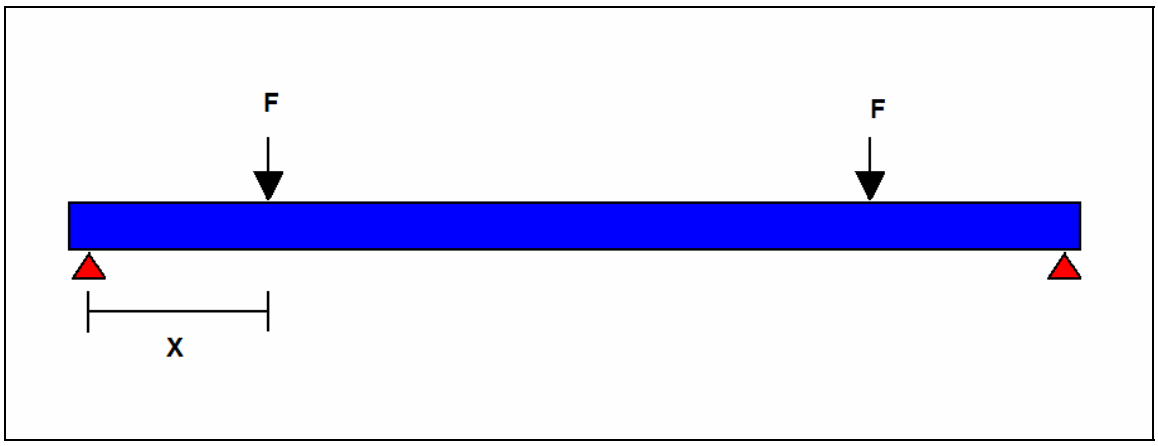

Figure 54: Four point bending test set-up

B.2 Test Results.

Because this is a comparative study the maximum force that the beams could withstand were used as the performance measurement criteria. The maximum bending moment can be calculated by multiplying the half maximum force by the bending arm. It is also assumed that these are the only suitable sizes of beams available thus the comparison is not done on maximum stress levels but on maximum load.

The two wood beams performed very much to expectations, especially when one is considering the manner in which failure occurred. The pine beam fractured on knot in the wood, located in the high bending moment area. The Saligna beam is of higher quality than the pine, as no visible knots or defects could be seen, this is reflected in the maximum force that the beams could carry. The failure here was in shear as expected, which would indicate that the failure was not caused by a defect but rather reflect the true shear strength of the material.

Figure 55: Failure of Pine beam

Figure 56: Failure of Saligna beam

Figure 57: Delamination in composite beam

Figure 58: Failure comparison of the different designs

Failure in the composite beam was more complex. There was no catastrophic failure as was the case with the wood specimens. The beam rather underwent plastic deformation resulting in permanent bending of the beam. This would suggest that the steel in the composite carried most of the bending load. It seems that the fibre reinforcement only serves to wrap the steel around the poly-urethane foam and lend little to the beam in terms of bending strength. As can be seen from Figure 57, the outer layer of reinforcement did delaminate. This could be related to the blips in Figure 59 at around 10 kN.

Figure 59: Test **results**

B.3 Test Analysis

The Pine beam ruptured at 5850 N, about 40% of the 14500 N and 15400 N reached by the Saligna beam and Composite beam respectively. Unless the Pine beams lend an exceedingly good financial argument to the topic, one would be hard pressed before using pine as the main structural members of a trailer floor. The tussle between the Saligna and Composite beams are much closer. The Saligna beam could easily be used as a replacement of the composite beam, if detail design could resolve the problems with securing the box to the chassis. The Saligna beam also weights less than the composite beam and would certainly cut down on manufacturing time. The ultimate decision between the two beams would be a financial one, as they are almost identically in a structural sense. The only advantage that the composite beam has over the Saligna is the fact that failure here occurs as a result of large deflection and not catastrophic failure. From a safety point of view this is highly desirable.

B.4 Conclusion

Three refrigerated trailer floor beams was tested in a four point bending test. The Pine beam had the worst performance with the Saligna and composite beams being almost identical is in a structural sense. The decision between the two beams should be made on financial grounds.

Appendix C 1st Iteration Structural Evaluation

C.1 Introduction

Design is an iterative process and to give an idea of the process used an earlier version of the design is presented. The following is the finite elements analysis results of one of the first chassis designs with the initial load box design. The model was essentially identical to that presented in the main text but here use was made of thinner top and bottom goose neck plates with a thickness of 8 mm. The internal stiffeners were also thinner at 8 mm. No doubler plates were used at the web stiffener connection points and the web stiffeners were 5 mm thick.

C.2 Load box

The Snap 750 design was modelled using shell elements. All material properties were defined as single layer orthotropic laminates with the appropriate thicknesses and care was taken to properly align the material directions. Material properties were summarised on page 29. All laminate properties will be evaluated according to the Hill failure criteria. Element size was chosen to fit two elements in the height of the ribs of the Snap 750 profiles. This dictated a very fine mesh of the complete structure. The complete model consisted of 400 613 nodes defining 537 885 elements.

The trailer was modelled without doors as their structural contribution is small due to play in the hinges and elastic seal between the load box and the doors. The cooling unit was approximated with beams and mass elements. In Figure 21 the Corner 65 sections can be seen in light blue with the Snap 750 side profiles in purple.

The corner elements used the same nodes than the floor and the side elements but with and property with offset mid-plane stress recovery positions. This method was also used to join the bottom floor plate and the top flanges of the chassis I-beams. In practice this interface will be joined with structural adhesive and clamps spaced along the length of the trailer. The payload was evenly distributed on the top floor plate elements by means of non-structural mass. Please take note of the definition of the coordinate frame as this will be referenced to later.

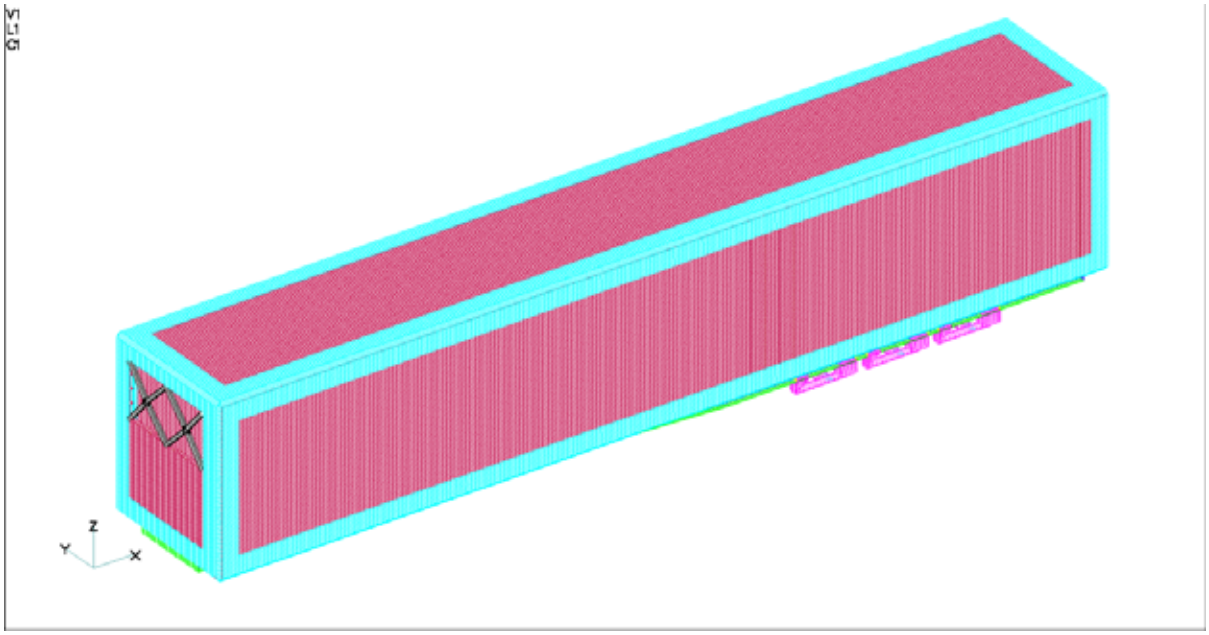

Figure 60: Complete semi-trailer model.

C.3 Chassis

This aluminium chassis design was extensively modified from similar steel structures. The chassis is made of two I-beams connected by vertical connection plates which provided the torsion stiffness and the top plate which gives the chassis transverse shear stiffness. The flanges of the I-beams are 8 mm thick with a 5 mm web. Stiffeners were placed on the suspension mounting points to distribute the load between the flanges. The stiffeners can be seen in yellow.

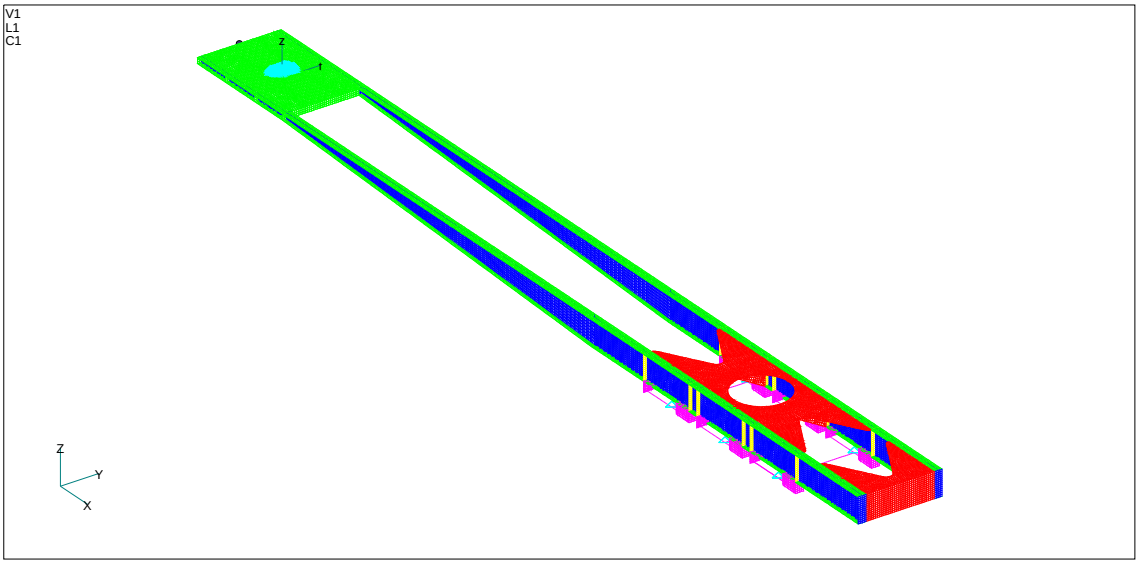

Figure 61: Complete chassis structure.

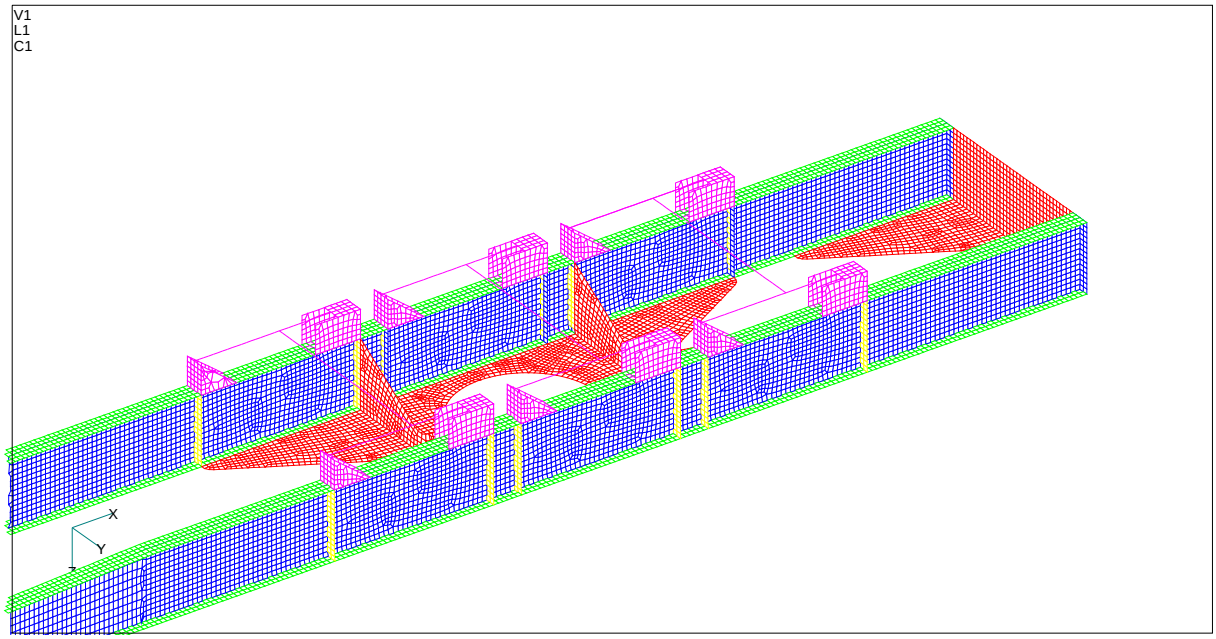

Figure 62: FEM detail of the chassis rear as viewed from underneath.

The goose neck is a major structural part. The top and bottom goose neck plates are 8 mm aluminium with internal stiffener plates also of 8 mm Xtral 728. These stiffeners run longitudinally and transverse to distribute bending loads. The diagonal stiffeners provide torsional stiffness to the goose neck.

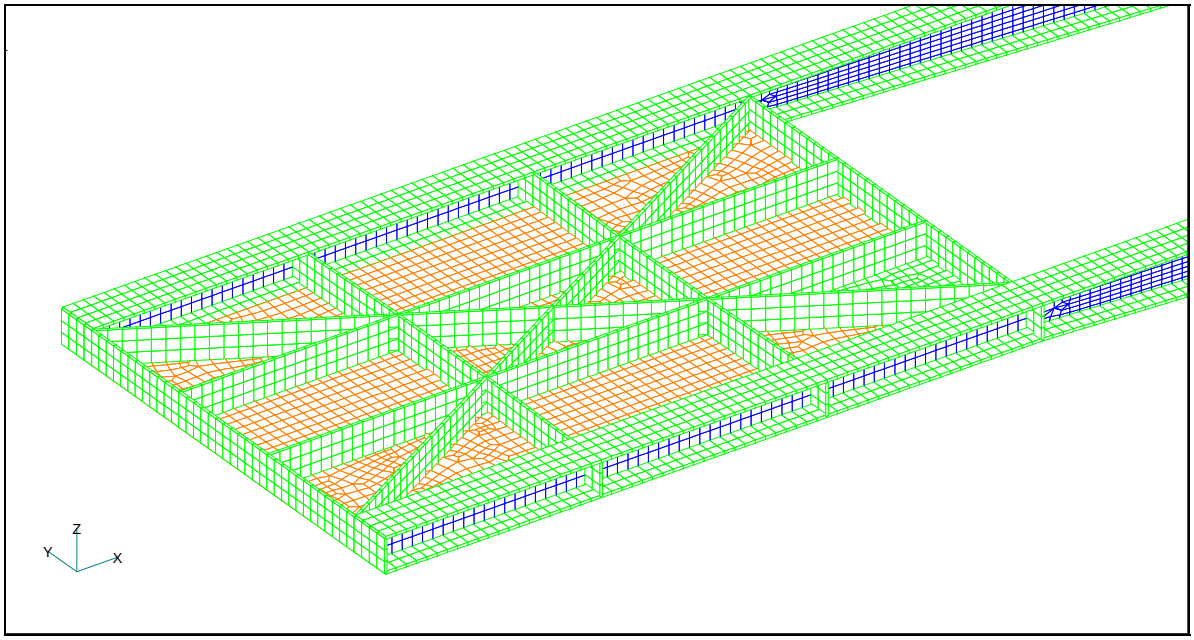

Figure 63: FEM detail of the goose neck.

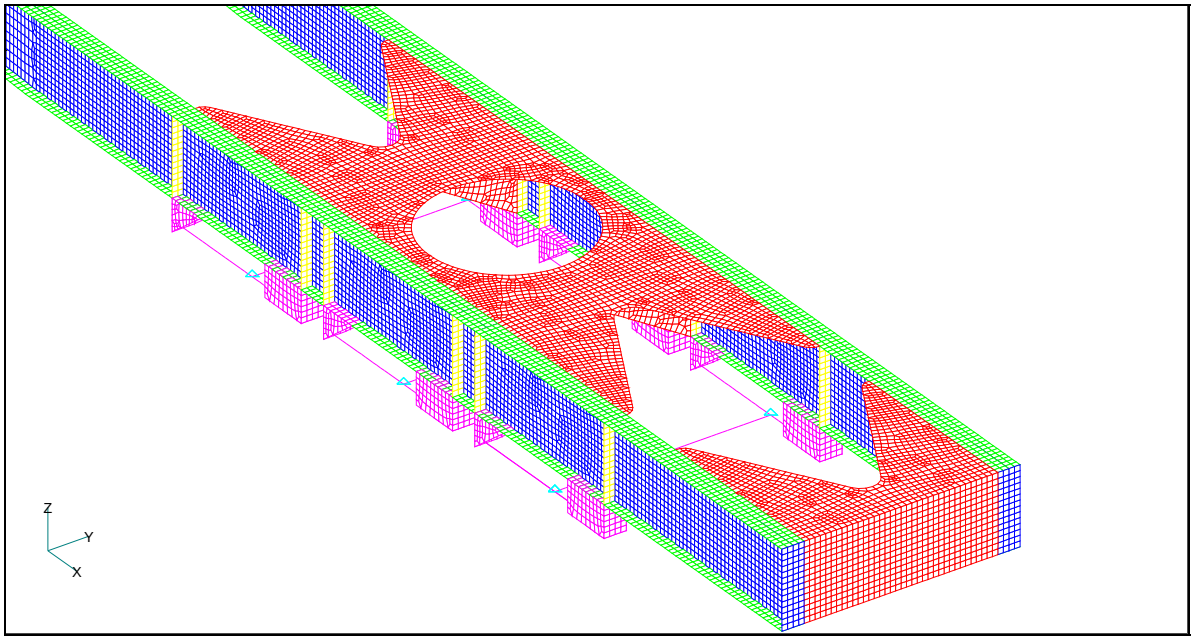

Figure 64: FEM detail of the chassis rear as viewed from the top.

C.4 Suspension

BPW suspensions are very popular with South African semi-trailer manufacturers. A suitable 9 tonne air suspension was chosen from their product range and included in the FE model. The suspension was simplified by modelling the air spring as solid, since the dynamic behaviour of suspension is not under consideration.

Hanger brackets were modelled with shell elements and are a functional copy of the *BPW* design. The foot print of the air spring was used to construct a box which contains a pivot point completing the suspension set-up.

C.5 Load cases and constraints

Six static load cases were applied to the structure. The loads have been discussed in the previous chapter and are listed in Table 15. Three constraint sets were used.

- Normal static, describes the conditions when the vehicle is driving on the road in a straight line. The nodes around the king pin which would have made contact with the fifth wheel were held by constraints defined in a cylindrical coordinates with the local Z axis coinciding with the global Y axis. Nodes defined in this coordinate frame were allowed to rotate around local Z axis on a fixed radius and were also fixed in Z translation. Constraints on the rear bogies were defined in terms of the global frame of

reference. One side of suspension was fixed in Z and Y translation with the other side only fixed in Z translation. All rotational degrees of freedom were left unconstrained.

- The normal braking constraint set is applicable to analyses concerned with the forces induced during an emergency stop. The king pin constraint was identical to that of the normal static constraint set. One side of the rear bogies were pinned and the opposite side fixed in translation in X and Z.
- To simulate scuffing all rear bogies were fixed in Y and Z translation. The fifth wheel nodes were constraint in global X and Z. The scuffing force of 19941.5N was then applied at the fifth wheel.

A list of the analyses is presented in Table 18.

Table 27: FEM load cases.

Load Case	**Load**	**Constraint**
1	1 g in +Z	Normal static
2	2 g in -Z	Normal static
3	2 g in -X	Normal braking
4	1 g in +Y	Normal static
5	Scuffing	Scuffing
6	Curb stepping	Normal static

C.6 Static and quasi-static load results

The results from the analyses were examined on the basis of material. All elements with orthotropic material properties were evaluated according to the Hill failure criteria. The Von Mises failure theory was used for isotropic materials.

C.6.1 Load case 1: 1g Positive vertical acceleration

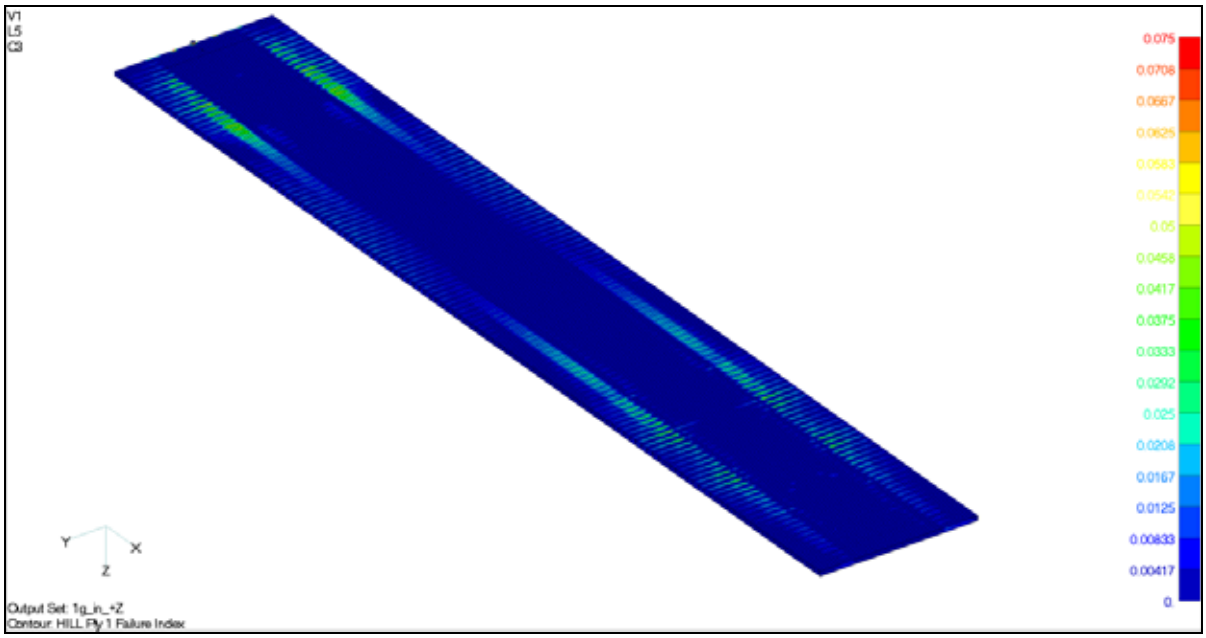

Figure 65: Hill failure index of the pultruded floor webs at 1g in +Z.

Stresses in the composite parts are very low in this load case with a peak failure index of 0.13 in the floor webs. This is cause by the high shear loads at the point where the load box drops of the chassis.

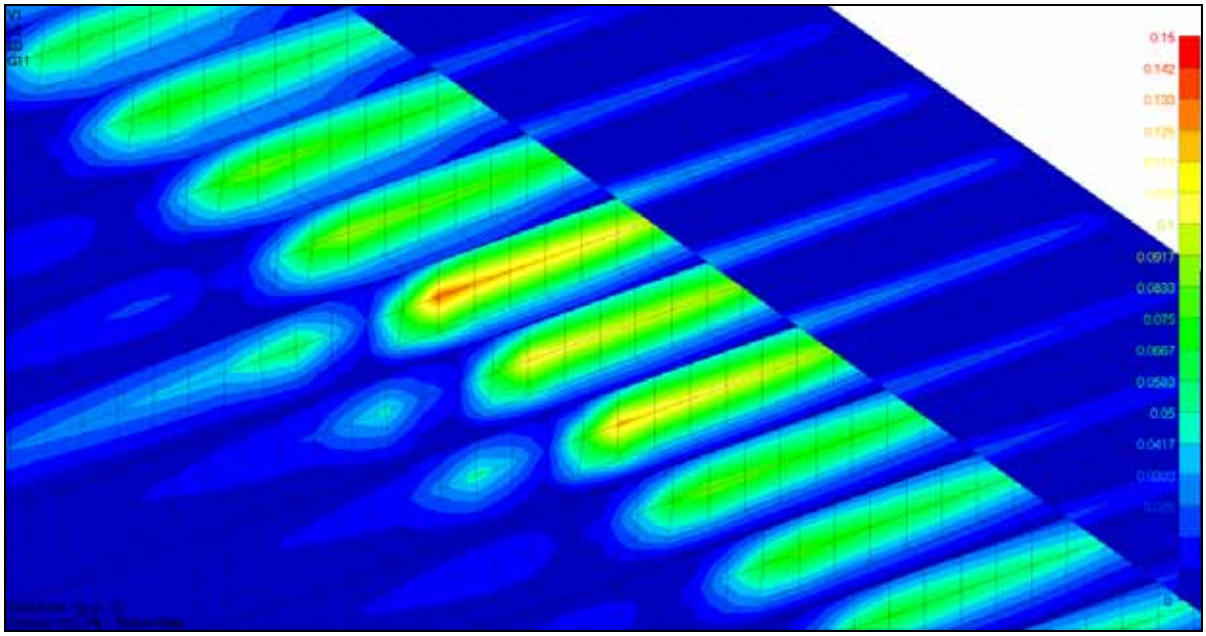

Figure 66: Hill failure index of floor webs at 1g in +Z.

Stresses in the chassis are more pronounced with a peak von Mises stress of 87.9 MPa shown in the internal stiffener webs near the king pin. Average element stresses of 64.4 MPa are seen at the connection points of the flange stiffeners in the goose neck. Stresses in the rest of the chassis are below 45 MPa.

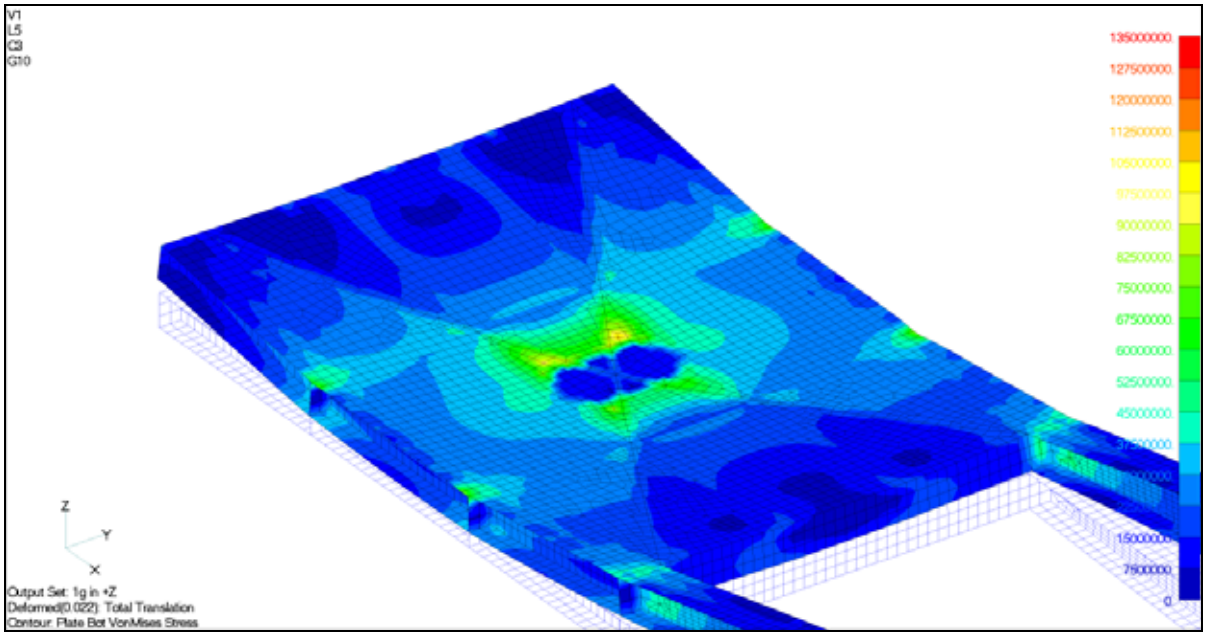

Figure 67: Stresses in goose neck at 1g in +Z.

C.6.2 Load case 2: 2g Negative vertical acceleration

In this load case the structure is highly stressed. Once again it is noted that the webs of the floor is under high shear stress with a failure index of 0.53. The highest stresses occur at the outer edge of the chassis flanges which in effect mean that the rest of the floor sides overhang act as cantilever, which explains the position of high stress. High stresses also occur on the leading edge of the floor. These higher stresses are the result of a modelling inaccuracy. The nodes on the front plate of the chassis and those on the front edge of the load box are not all joined. The three areas of high stress coincide with positions where the nodes are joined (see Figure 30). In practice the load box and chassis will be fixed together by an adhesive which will distribute the loading properly and hence lower peak stresses will be seen but a higher average which should be at an acceptable level.

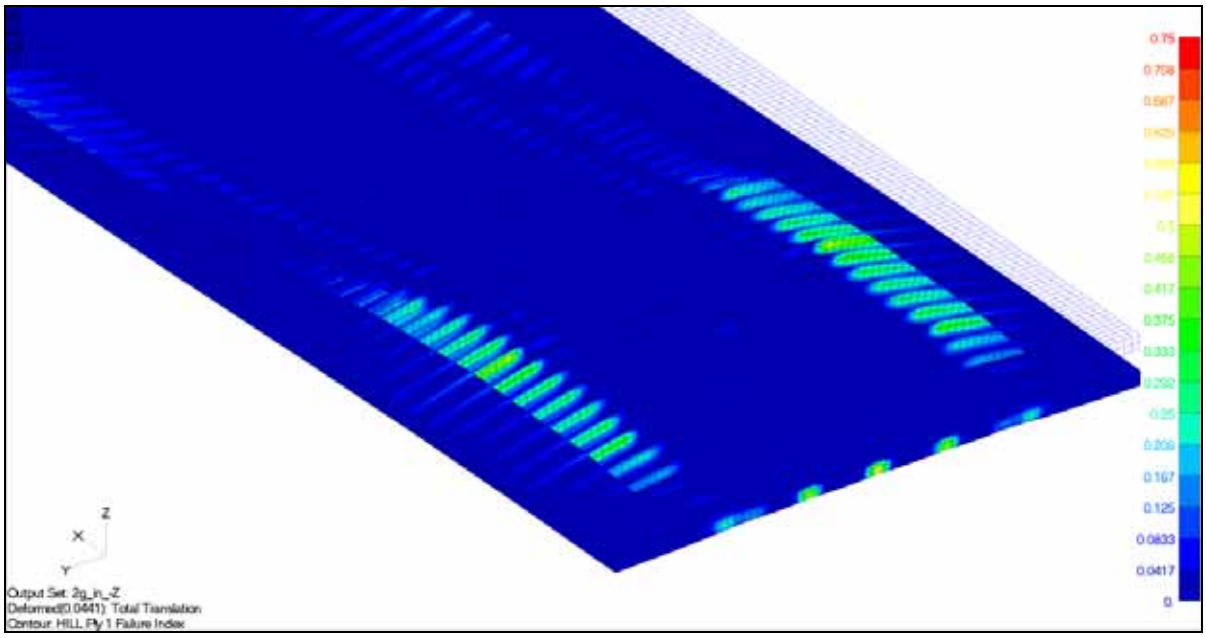

Figure 68: Floor failure index near the front at 2g in –Z.

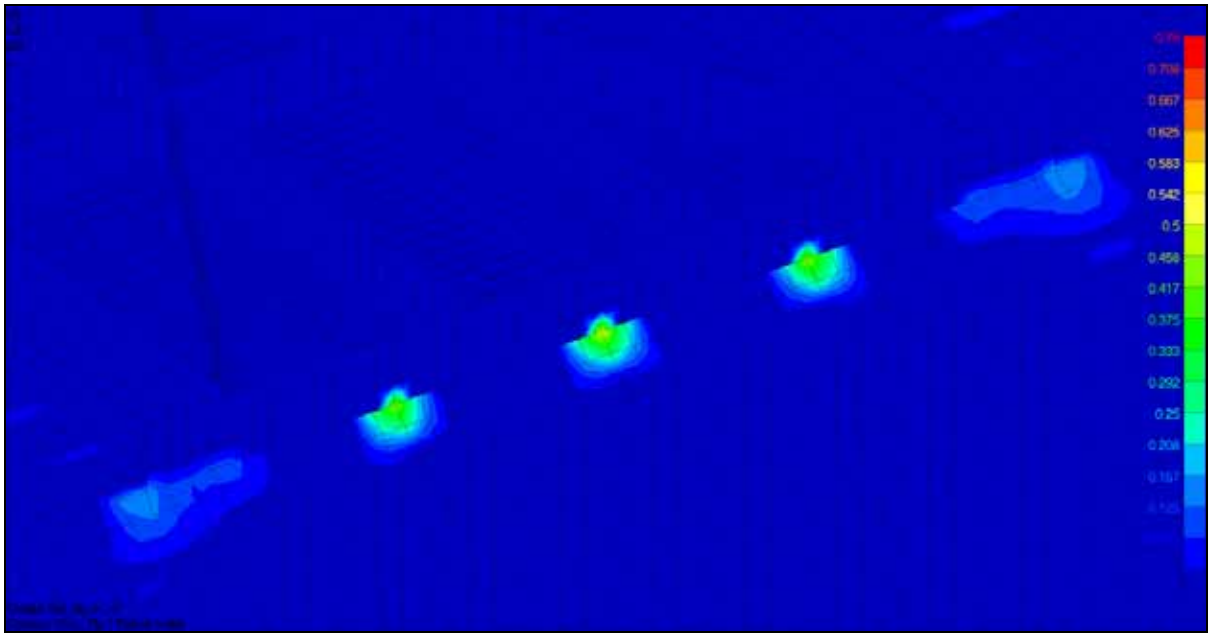

Figure 69: Modelling inaccuracy on the leading edge of the floor.

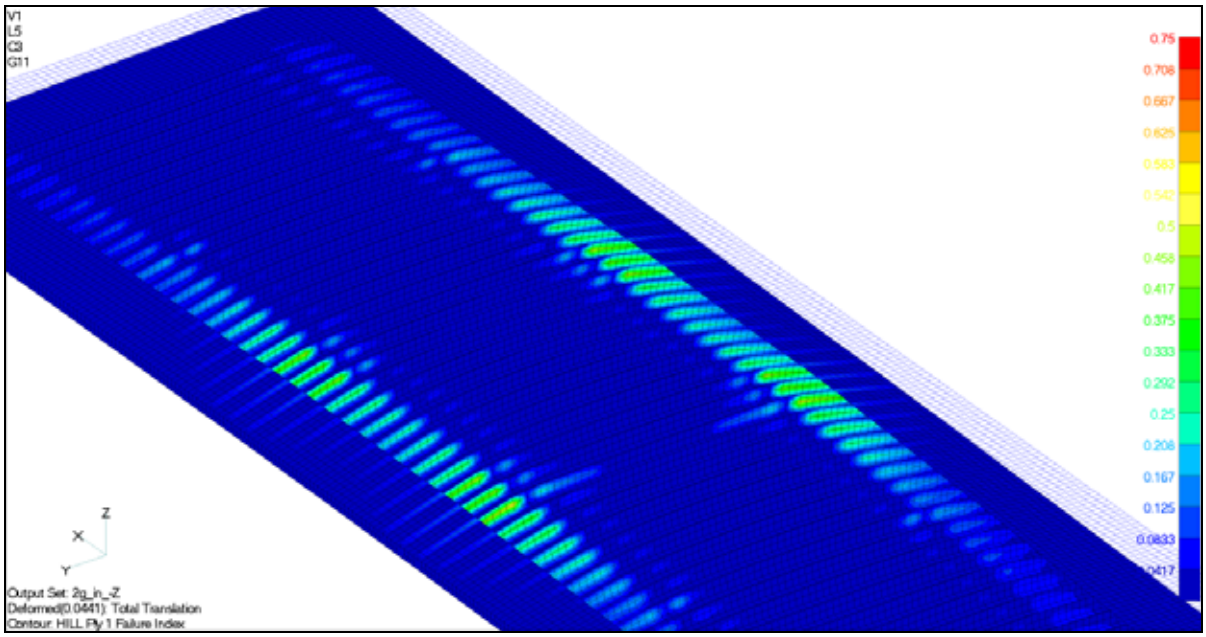

Figure 70: Rear floor failure index at 2g in –Z.

High web stresses also occur at the rear of the composite floor. The highest stress points occur at the positions where the load from the two axles is applied with a failure index of 0.53. This is an acceptably low stress level.

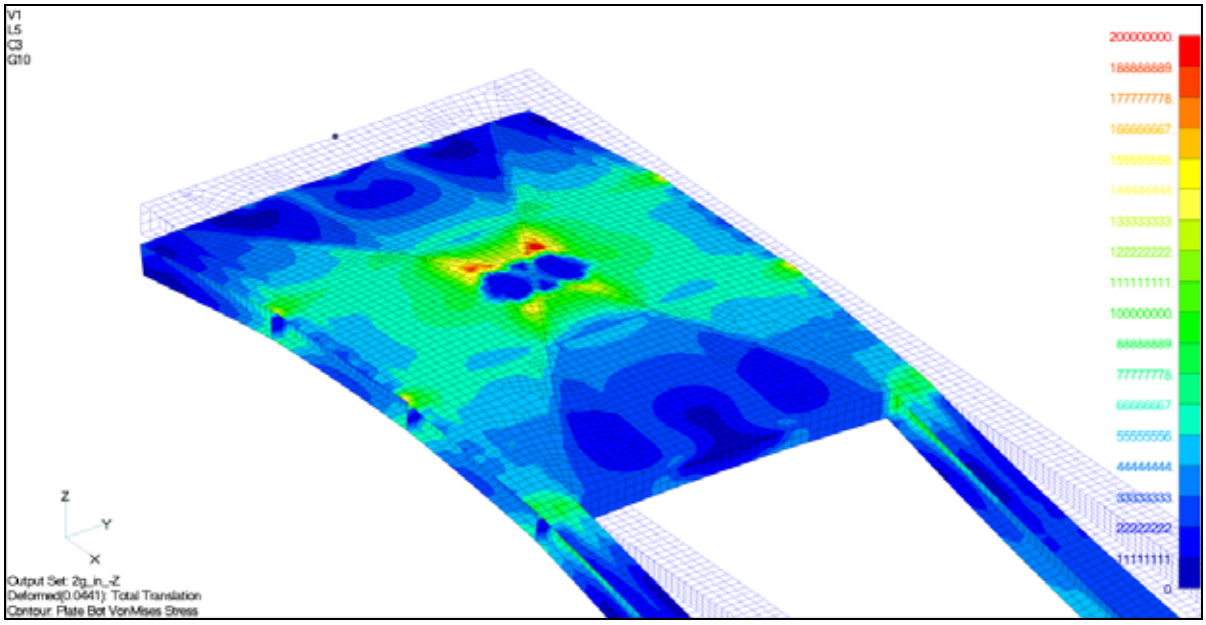

Figure 71: Stresses in the goose neck at 2g in -Z.

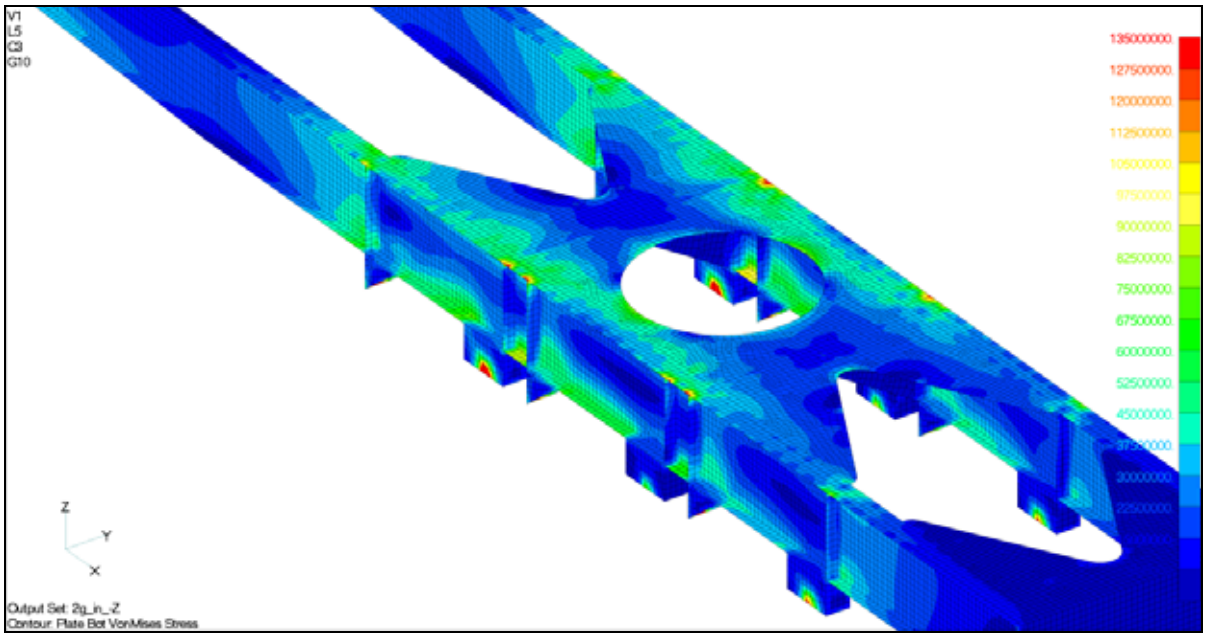

Figure 72: Stresses in the rear of the chassis at 2g in -Z.

Chassis stresses are acceptable in general but very high stresses are generated in the goose neck and at the rear web stiffeners at the suspension mounting points. At 150 MPa these stresses exceed the yield stress of the material and a redesign will be needed to address the problem. The high stresses are caused by marginal design and the use of a constraint set which does not allow the

At the goose neck it is suggested that the cover plate and internal stiffener thickness be increased from 8 mm to 10 mm. To reduce the stresses at the suspension mounting point it is advised that a doubler plate be added to the flange section between the web stiffeners. The doubler plate should extend 100 mm on both sides of the stiffeners and should be profiled to give a gradual change in stiffness to prevent a stress concentration.

Further analysis will be performed to evaluate these suggestions.

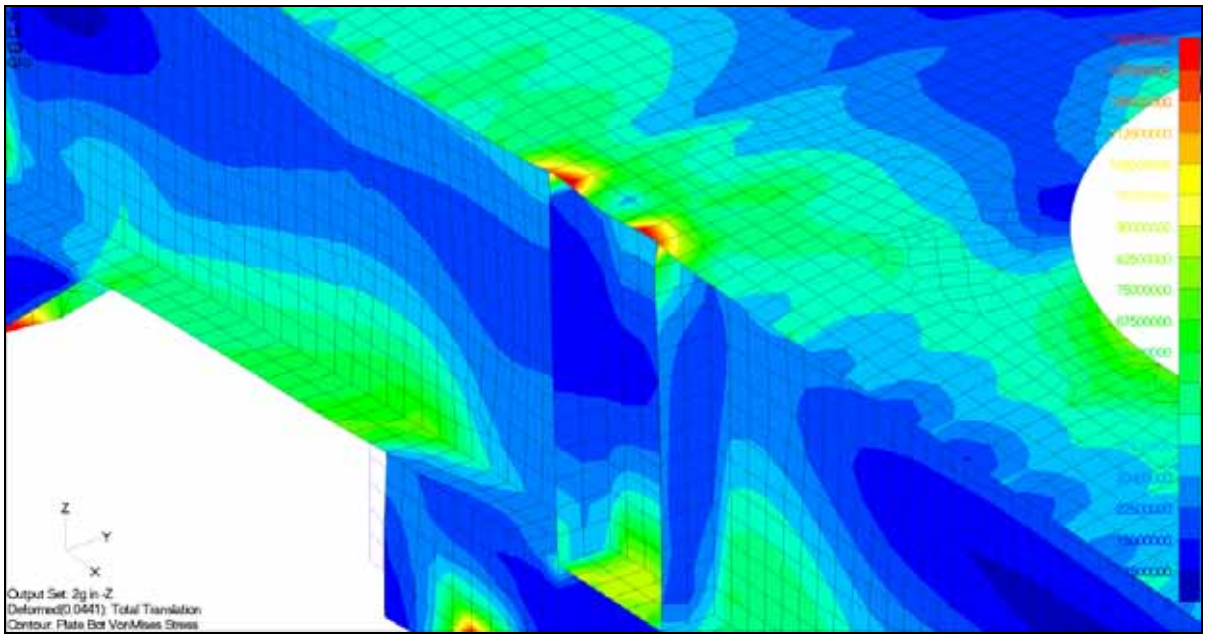

Figure 73: Detail of high stress area at rear web stiffeners at 2g in -Z.

C.6.3 Load case 3: 2g Axial acceleration

According to this analysis low stresses are generated during braking. The highest stresses were found at the points where the refrigeration unit are mounted. This model approximate the reefer unit with mass elements and beams and only six mounting points is used. In practice the load is distributed much better and hence the stresses will be lower.

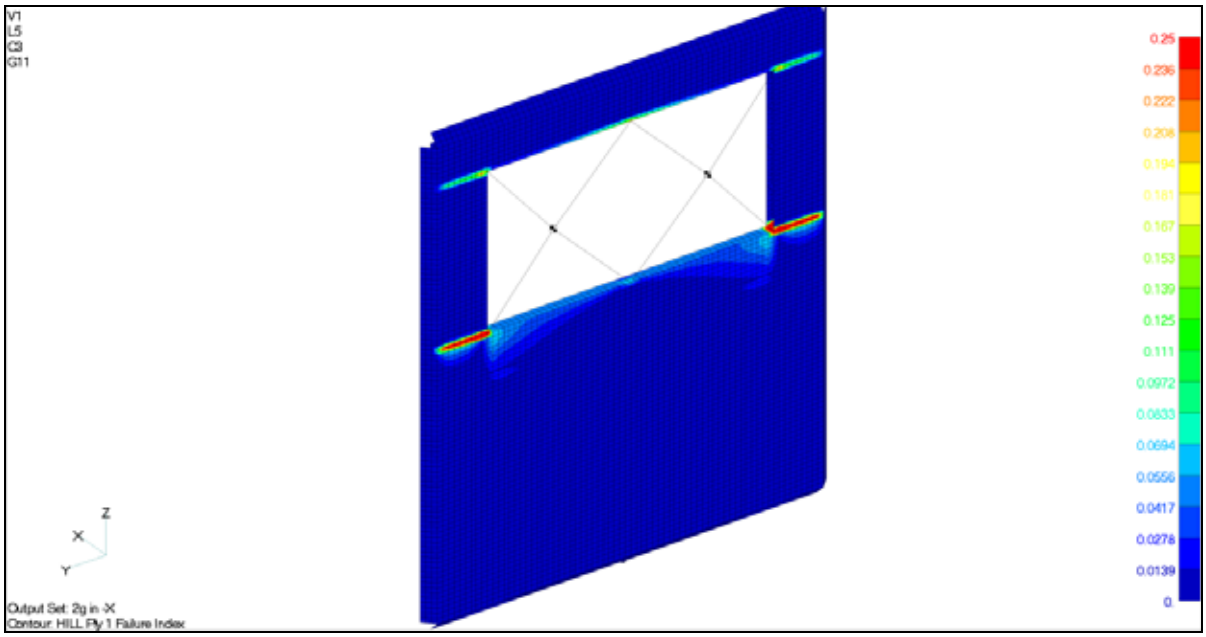

Figure 74: Hill failure index of load box bulkhead at 2g in –X.

Low stresses are generated in the floor webs with a peak failure index of 0.15.

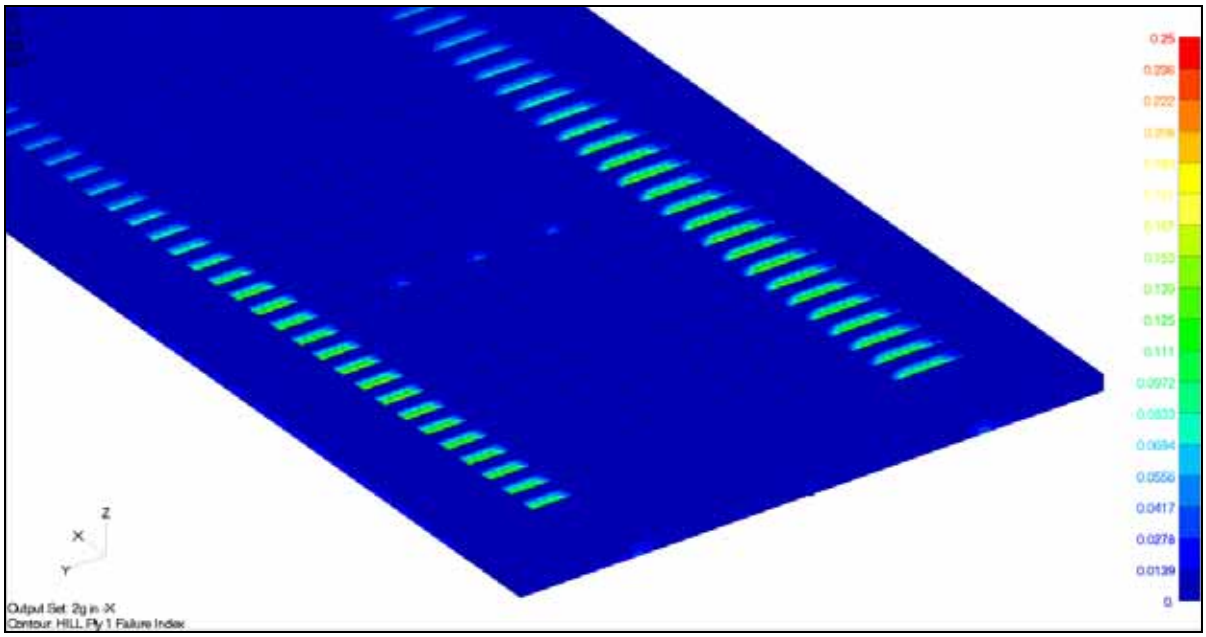

Figure 75: Failure index plot of floor at 2g in -X.

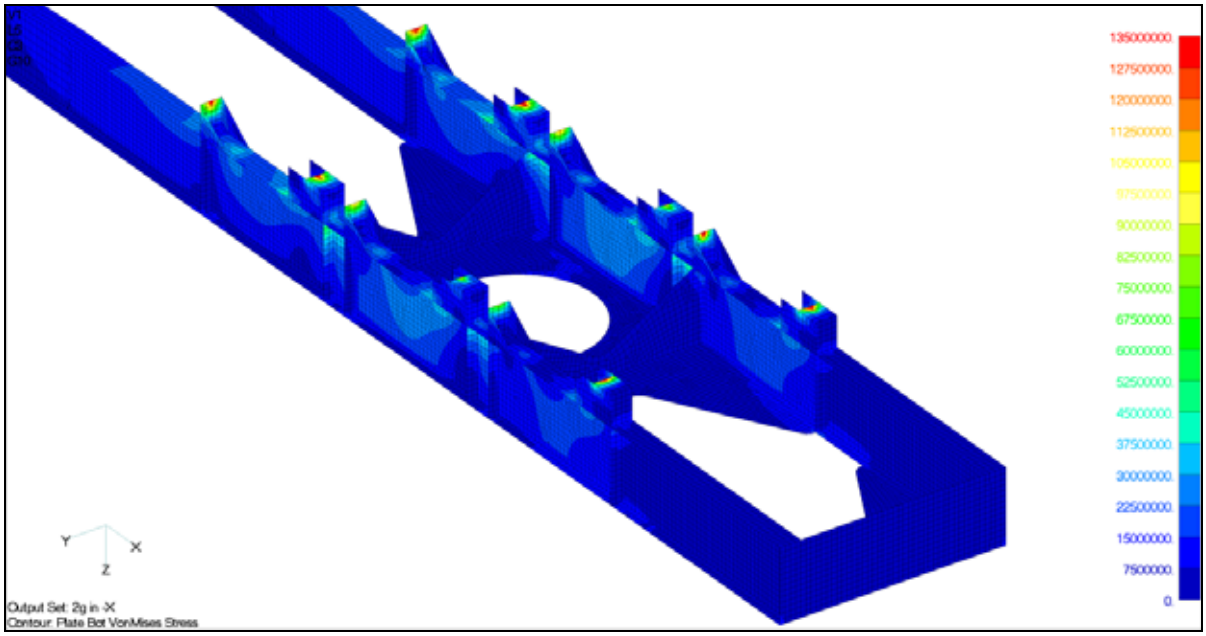

Figure 76: Von Mises stresses in chassis at 2g in -X.

The chassis also performs well in this load case with peak stresses of 42MPa near the bogie mounting points.

C.6.4 Load case 4: 1g Negative transverse acceleration

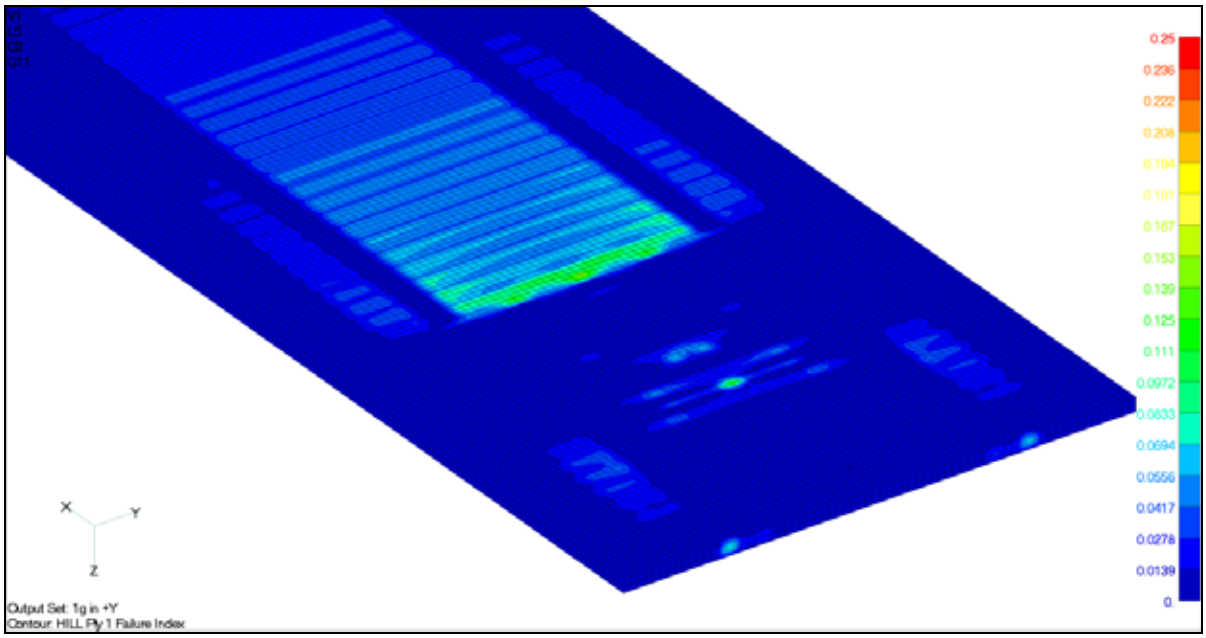

Figure 77: Failure index of the floor for load case 4.

Composite stresses are low with the maximum failure shown 0.16. This is once again seen in the floor webs. The chassis stresses are very high the structure will fail at numerous positions. Low transverse stiffness of the chassis allows it to perform a parallelogram deformation

causing very high stresses at the stiffening plate fix points. The low transverse stiffness is caused by mass saving cut-outs in the transverse stiffening plates. A redesign of the transverse stiffening plates must be performed.

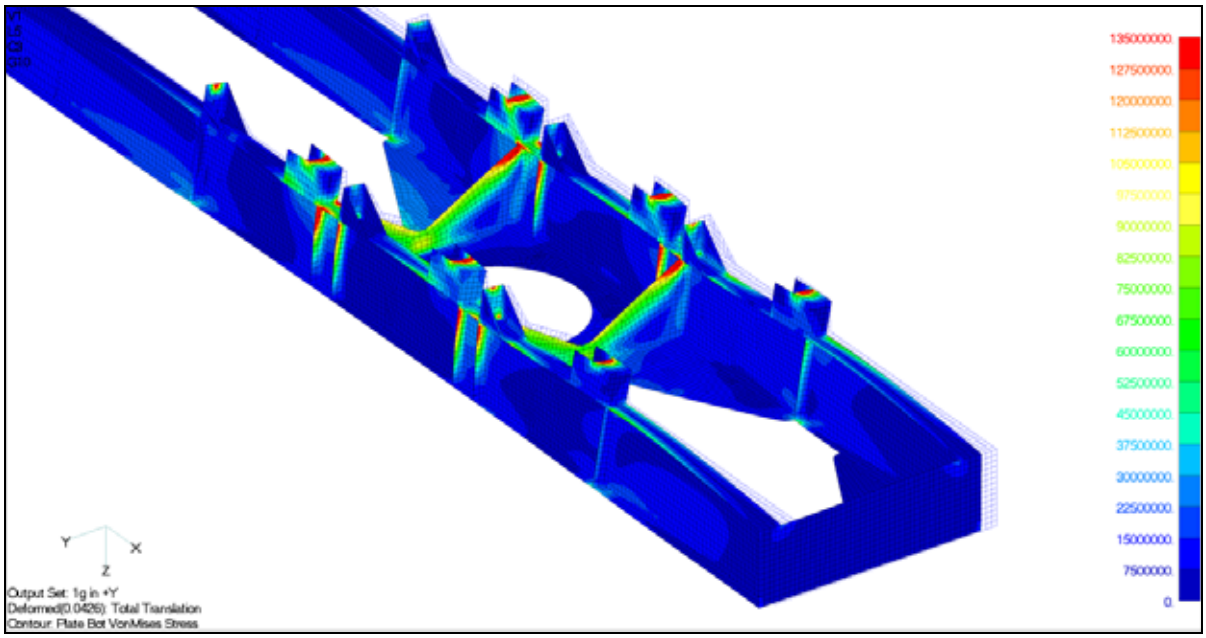

Figure 78: Von Mises stresses in chassis during transverse acceleration.

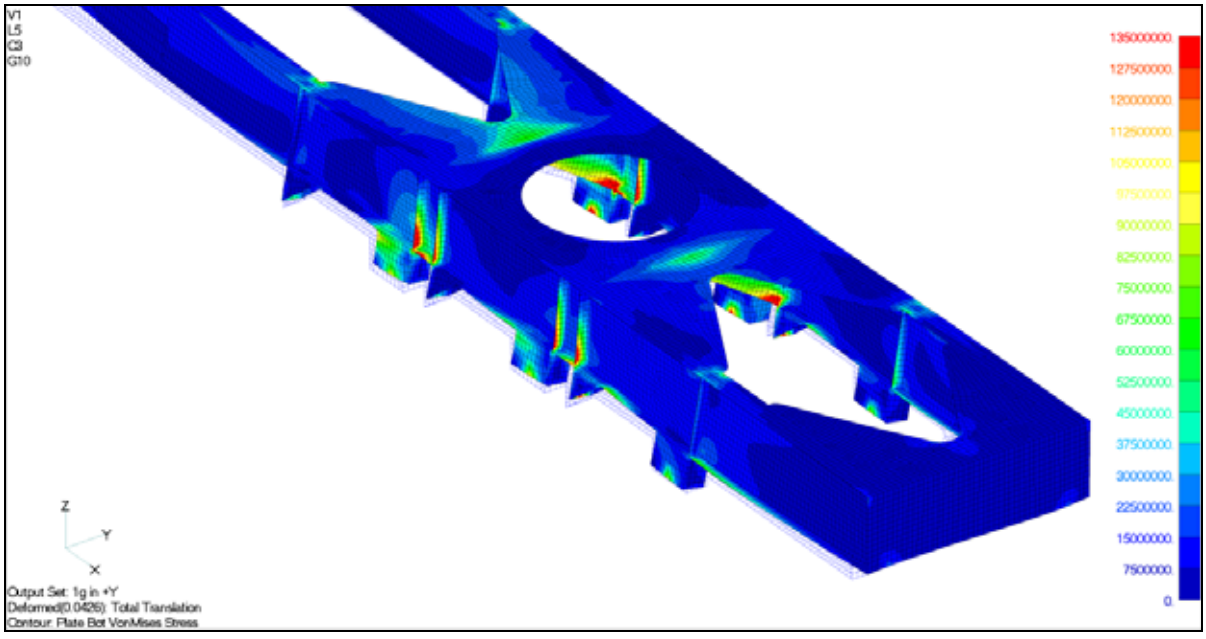

Figure 79: Top view of chassis stresses at 1g transverse accelaration.

C.6.5 Load case 5: 19.95 kN Scuffing load

Tyre scuffing is also a severe load case and high stresses are present in the chassis. The load box however is not highly stressed, with a peak failure index of 0.28 found in the floor webs at positions corresponding to the outer hanger bracket mounting points.

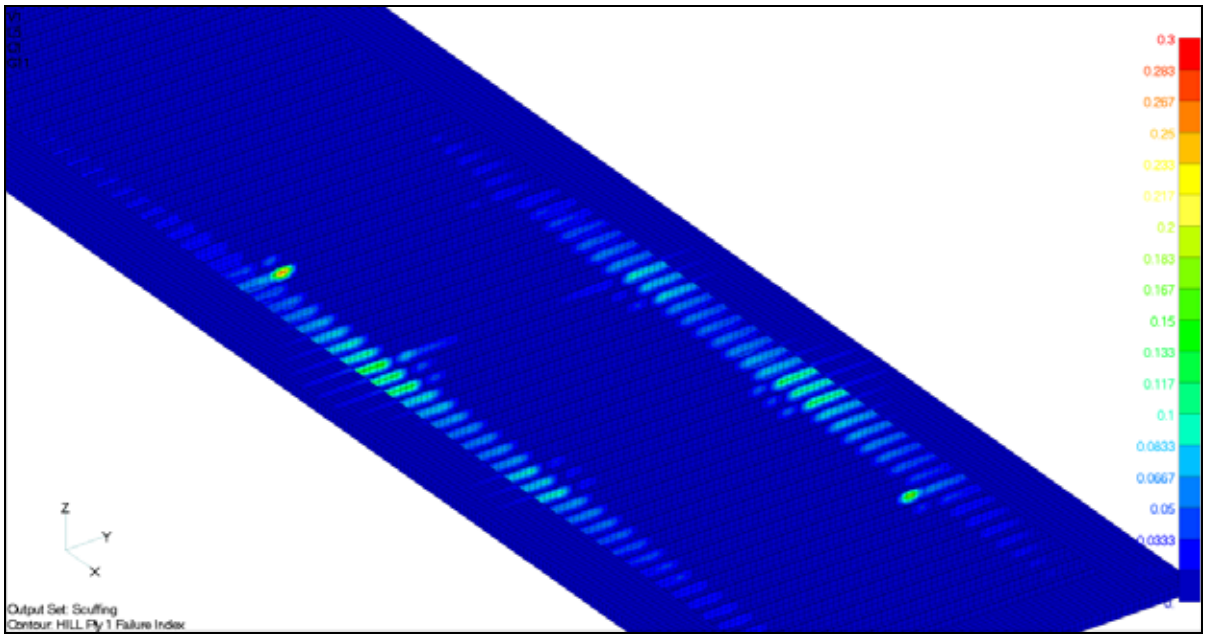

Figure 80: Failure index of composite floor exposed to tyre scuffing.

Stresses in the goose neck exceeded the yield point of the material. A peak stress of 151 MPa is seen in the top plate where the load is applied. The load was distributed between five nodes and large stress gradient is seen at these points. Better structural performance will be achieved if the load is more distributed.

High stresses near the bogie mounting points in the transverse stiffening plates are also seen. Peak stress of 178 Mpa is recorded. Bending stresses in the web stiffener also exceeds the yield point of the material.

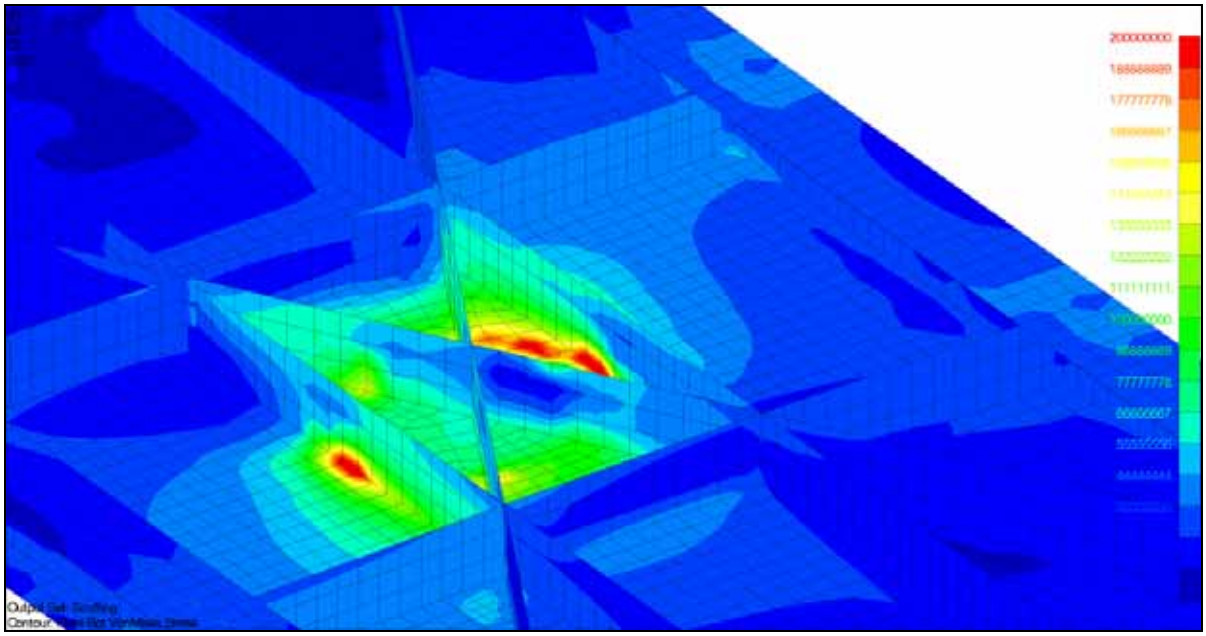

Figure 81: High stresses in goose neck caused by tyre scuffing.

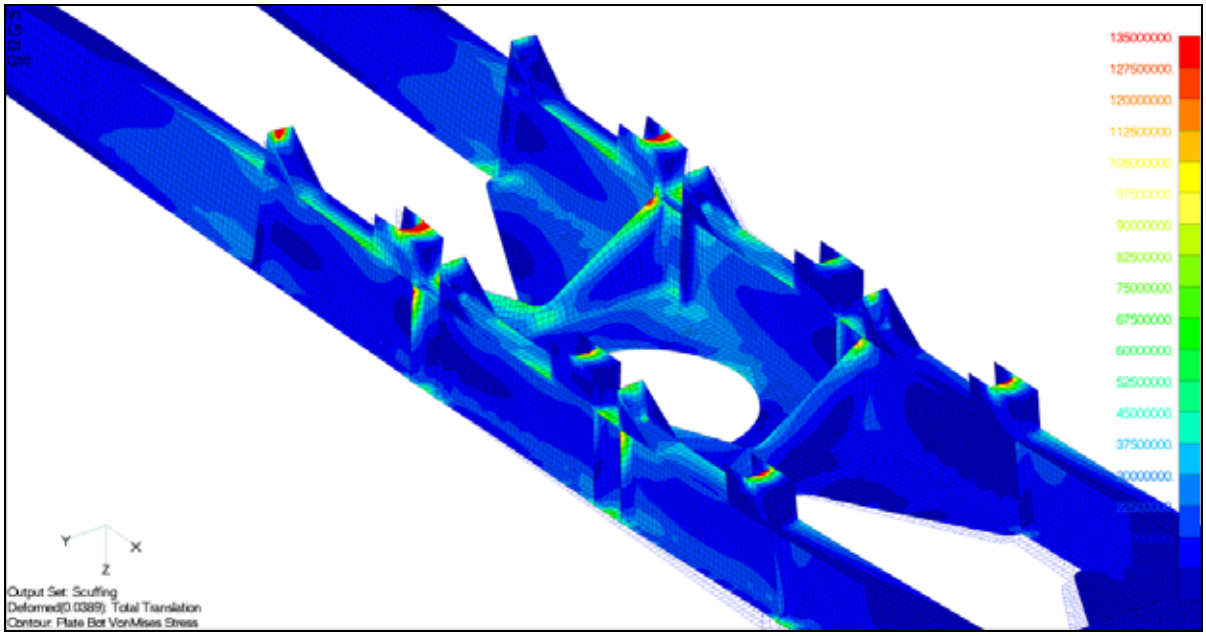

Figure 82: Von Mises stresses in the rear chassis for the tyre scuffing load case.

C.6.6 Load case 6: 50mm Curb stepping

This torsional displacement load gives the highest stresses in the composite load box. However these stresses are localised giving the impression that they might be caused by constraint forces. Hence the stresses at these locations are deemed acceptable.

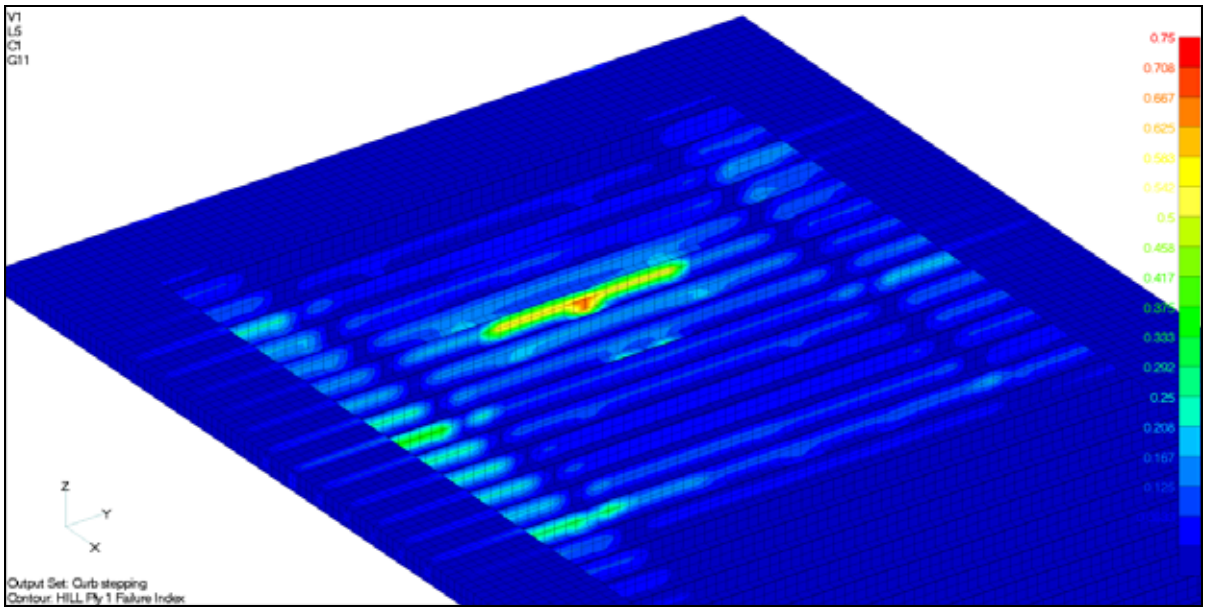

Figure 83: Failure index in the floor webs for torsion load.

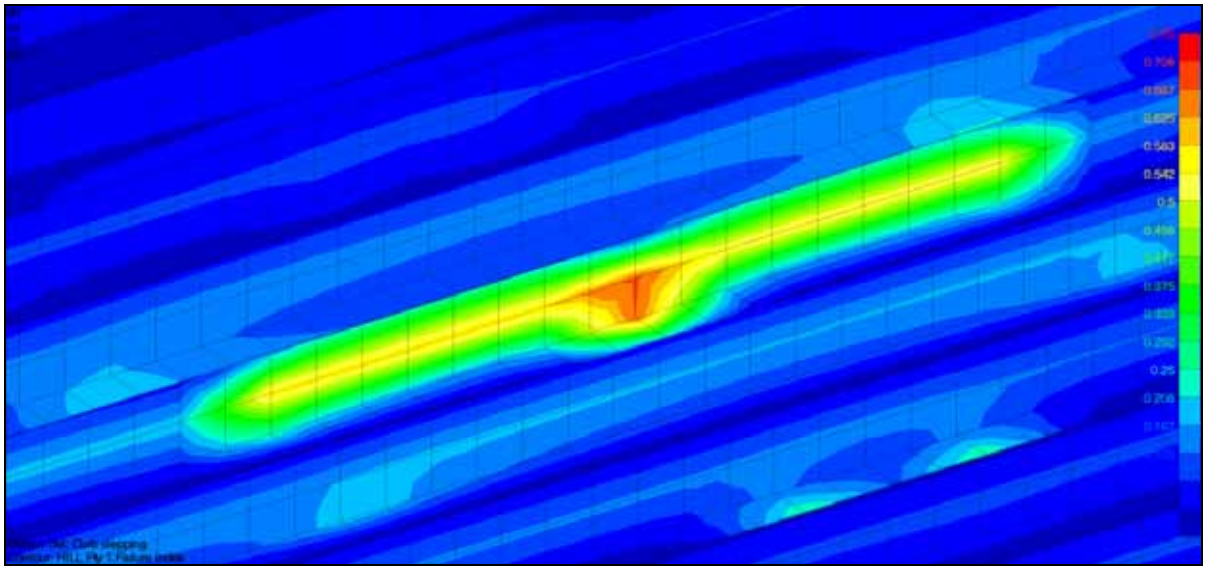

Figure 84: Detail of floor failure index.

Very high stresses of up to 187 MPa are seen in the goose neck. Shear stress load paths are clearly seen in Figure 45. To increase the shear path length it is advised to increase the

distance between the axial goose neck stiffener plates. This should distribute the shear loading by exposing more material to a lower average load.

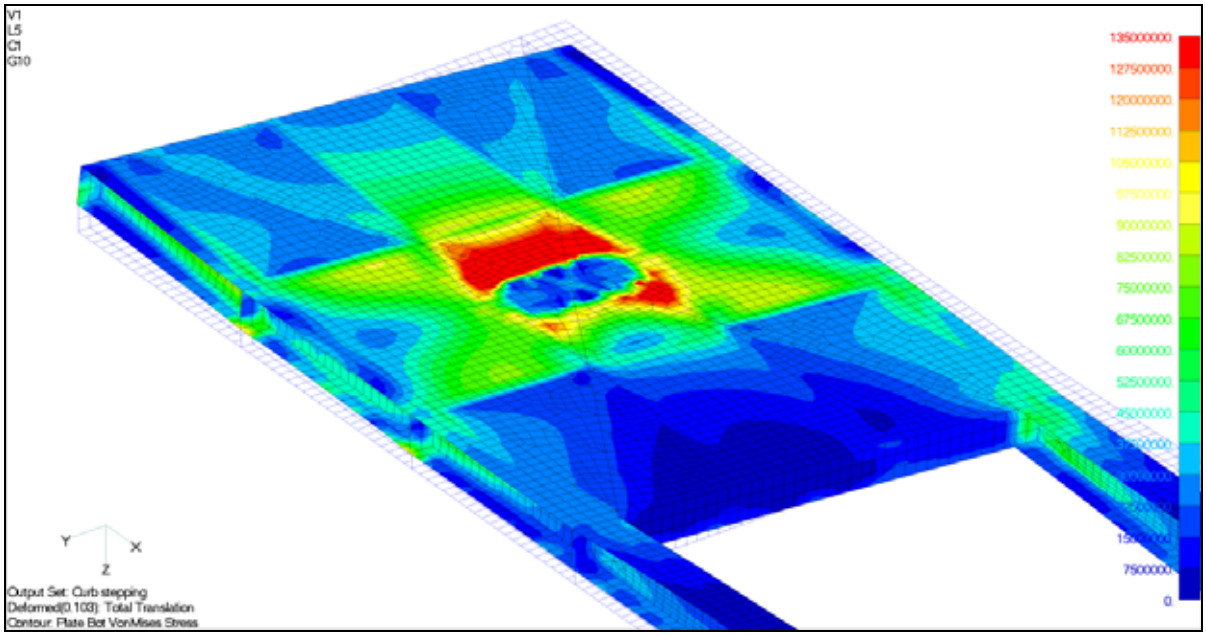

Figure 85: Goose neck stresses for the curb stepping.

Stresses near the bogie mounting point are at acceptable level and the only area of concern is the web stiffener plates where stresses peak at 118 MPa. These stresses can be lower with a redesign of the transverse stiffener plates.

Appendix D Computer Code

D.1 Code to determine mechanical properties of composites

```
%*******************************************************************************
%This program computes mechanical properties of a composite material with
%the use of Micromechanics. The material properties form the input for the calculation
%of the mid plane strains and curvatures of a laminate with n layers. Strains and average
%tensile stress is used to calculate the average tensile modulus.
%It also calculates the stresses and strains at the top and bottom of each lamina, in
%both the XY and LT co-ordinate systems.
%By Ockert Strydom Nov 2006
%*******************************************************************************
clear all
mat_id=[1 2 2 2 2 1 2 2 2 2 1];
% number of layers
n=11;
%Material properties for Resin:NCS992 and E-glass in MPa
Em = 4027; %Matrix stiffness
Ef = 72.4e3    %Fibre stiffness
vm = 0.35;    %Matrix poisson
vf = 0.2      %Fibre poisson
Gm = Em/2*(1+vm); % Matrix shear modullus
Gf = Ef/2*(1+vf); % Fibre shear modullus


for i =1:n;
    if mat_id(i)== 1;
        % Volume fill fractions
        Vf = 0.285;   % Fibre fill fraction for mat
        Vm = 1-Vf;  % Matrix fill fraction
    else
        Vf = 0.645;   % Fibre fill fraction for rovings
        Vm = 1-Vf;  % Matrix fill fraction
    end
    % Calculation of lmina properties with Micromechanics
    E11 = Vf*Ef + Vm*Em; % Longitudinal stiffness of lamina
    v12 = Vf*vf + Vm*vm; % Lamina poisson
    nn = ((Ef/Em) - 1)/((Ef/Em) + 2);
    E22 = Em*(1 + 2*nn*Vf)/(1 - nn*Vf); % Transverse stiffness of lamina
    nn = ((Gf/Gm) - 1)/((Gf/Gm) + 1);
    G12 = Gm*(1 + nn*Vf)/(1 - nn*Vf); % Shear stiffness of lamina

    if mat_id(i)== 1;
        %Lamina mechanical constants in MN/m^2 and mm;
        EL(i)=(3*E11 + 5*E22)/8;
        ET(i)=(3*E11 + 5*E22)/8;
        GLT(i)=(1*E11 + 2*E22)/8;
        NuLT(i)=(EL(i)/(2*GLT(i)))-1;
    else
        EL(i)=E11;
        ET(i)=E22;
        GLT(i)=G12;
        NuLT(i)=v12;
    end
end
%Fiber angles for each layer;
theta=[0 0 0 0 0 0 0 0 0 0 0];
theta=theta(1:n)*pi/180;

%Load in N;
N=25e3;
F=0;
S=0;
Lz=4.76/n;

for i=1:n;
    NuTL(i)=NuLT(i)*ET(i)/EL(i);
end

%Size of Laminate
b=20;
```

```
h=-0.5*Lz*n:Lz:0.5*Lz*n;
l=400;

%Force resultants
Nx=N/b;
Ny=F/l;
Nxy=S/b;

%Moment Resultants
Mx=-F*l/b;
My=-F*b/l;
Mxy=0;

% Calculation of the Q-Matrix and transformation to the Qdash matrix
Q=zeros(3,3,8);
    for i=1:n;
        q(1,1)=EL(i)/(1-(NuLT(i))*NuTL(i));
        q(2,2)=ET(i)/(1-NuLT(i)*NuTL(i));
        q(1,2)=NuTL(i)*EL(i)/(1-NuLT(i)*NuTL(i));
        q(2,1)=q(1,2);
        q(3,3)=GLT(i);
        q(1,3)=0;
        q(3,1)=0;
        q(2,3)=0;
        q(3,2)=0;

        Q(1,1,i)=q(1,1)*(cos(theta(i)))^4+q(2,2)*(sin(theta(i)))^4 ...;
            +2*(q(1,2)+2*q(3,3))*(sin(theta(i)))^2*(cos(theta(i)))^2;

        Q(2,2,i)=q(2,2)*(cos(theta(i)))^4+q(1,1)*(sin(theta(i)))^4 ...;
            +2*(q(1,2)+2*q(3,3))*(sin(theta(i)))^2*(cos(theta(i)))^2;

        Q(1,2,i)=(q(1,1)+q(2,2)-4*q(3,3))*(sin(theta(i)))^2*(cos(theta(i)))^2 ...;
            +q(1,2)*((cos(theta(i)))^4+(sin(theta(i)))^4);

        Q(2,1,i)=Q(1,2,i);

        Q(1,3,i)=(q(1,1)-q(1,2)-2*q(3,3))*(cos(theta(i)))^3*sin(theta(i))...;
            -(q(2,2)-q(1,2)-2*q(3,3))*cos(theta(i))*(sin(theta(i)))^3;

        Q(3,1,i)=Q(1,3,i);

        Q(2,3,i)=(q(1,1)-q(1,2)-2*q(3,3))*cos(theta(i))*(sin(theta(i)))^3 ...;
            -(q(2,2)-q(1,2)-2*q(3,3))*(cos(theta(i)))^3*sin(theta(i));

        Q(3,2,i)=Q(2,3,i);

        Q(3,3,i)=(q(1,1)+q(2,2)-2*q(1,2)-2*q(3,3))*(cos(theta(i)))^2*(sin(theta(i)))^2 ...;
            +q(3,3)*((cos(theta(i)))^4+(sin(theta(i)))^4);

    end;

%Calculation of A matrix
A=zeros(3,3);
B=A;
D=A;

for k=1:n;
    A=A+(h(k+1)-h(k))*Q(:,:,k);
end;

%Calculation of B matrix
for k=1:n;
    B=B+0.5*(h(k+1)^2-h(k)^2)*Q(:,:,k);
end;

%Calculation of D matrix
for k=1:n;
    D=D+(h(k+1)^3-h(k)^3)*Q(:,:,k)/3;
end;

%Calculation of ABD Matrix
abd=zeros(6,6);
abd=[A B; B D]
NM=[Nx Ny Nxy Mx My Mxy]'

% Solution for strains and curvature of the midplane
```

```
disp('The midplane strains in XY co-ordinates')
EpsKappa=abd\NM

% Solution for tensile modulus
disp('The tensile modullus of laminate')
E_comp_long = N/EpsKappa(1)/(n*Lz*b)


% Solution of top and bottom stresses and strains of each layer in XY co-ordinates.
% And transformation of these stresses and strains to the LT co-ordinate system.
for i =1:n;
    Tsigma=[(cos(theta(i)))^2 (sin(theta(i)))^2 2*sin(theta(i))*cos(theta(i));...
            (sin(theta(i)))^2 (cos(theta(i)))^2 -2*sin(theta(i))*cos(theta(i));...
            -sin(theta(i))*cos(theta(i))    sin(theta(i))*cos(theta(i))    ((cos(theta(i)))^2-
(sin(theta(i)))^2)];

    Tepsilon=[(cos(theta(i)))^2 (sin(theta(i)))^2 2*sin(theta(i))*cos(theta(i));...
            (sin(theta(i)))^2 (cos(theta(i)))^2 -2*sin(theta(i))*cos(theta(i));...
            -2*sin(theta(i))*cos(theta(i))  2*sin(theta(i))*cos(theta(i))  ((cos(theta(i)))^2-
(sin(theta(i)))^2)];

    SigmaT(:,1,i)=Q(:,:,i)*EpsKappa(1:3)+h(i+1)*Q(:,:,i)*EpsKappa(4:6);
    SigmaB(:,1,i)=Q(:,:,i)*EpsKappa(1:3)+h(i)*Q(:,:,i)*EpsKappa(4:6) ;
    SigmaTlt(:,1,i)=Tsigma*SigmaT(:,1,i);
    SigmaBlt(:,1,i)=Tsigma*SigmaB(:,1,i);

    EpsilonT(:,1,i)=EpsKappa(1:3)+h(i+1)*Q(:,:,i)*EpsKappa(4:6);
    EpsilonB(:,1,i)=EpsKappa(1:3)+h(i)*Q(:,:,i)*EpsKappa(4:6);
    EpsilonTlt(:,1,i)=Tepsilon*EpsilonT(:,1,i);
    EpsilonBlt(:,1,i)=Tepsilon*EpsilonB(:,1,i);
end;

% Display of the Stresses and Strains
% disp('Transformation matrixes Tsigma and Tepsilon')
% Tsigma
% Tepsilon
%
% disp('Stresses at the top of each layer in XY co-ordinates')
% SigmaT(:,:)
% disp('Stresses at the bottom of each layer in XY co-ordinates')
% SigmaB(:,:)
% disp('Stresses at the top of each layer in LT co-ordinates')
% SigmaTlt(:,:)
% disp('Stresses at the bottom of each layer in LT co-ordinates')
% SigmaBlt(:,:)
%
%
%
% disp('Strains at the top of each layer in XY co-ordinates')
% EpsilonT(:,:)
% disp('Strains at the bottom of each layer in XY co-ordinates')
% EpsilonB(:,:)
% disp('Strains at the top of each layer in LT co-ordinates')
% EpsilonTlt(:,:)
% disp('Strains at the bottom of each layer in LT co-ordinates')
% EpsilonBlt(:,:)
```

D.2 Code to post-process service load data

```
%
*********************************************************************************************
*
% Data analysis program to calculate fft's from trailer data
% and to count acceleration peaks
% By Ockert Strydom Aug 2005
%
*********************************************************************************************
*
close all
clear all

% Load Measurement Data for plotting
    [filename, pathname] = uigetfile('*.txt', 'Pick an txt-file')
    if isequal(filename,0)|isequal(pathname,0)
       disp('File not found')
   else
       disp(['File ', pathname, filename, ' found'])
    end
data = ([pathname,filename])
meting = load(data);

% The following is put in because of a bug causing matlab to evaluate
% rest of the program before the uiimport is finished
go = input('Please press 1 > ' )
disp('---------------------------------------   ');
disp('   ');
disp('   ');
if go ~= 1
    close all
end
% Setting the matrixes up
n = size(meting, 1); % Num rows
m = size(meting, 2); % Num columns
tyd = zeros(n,1);
p = 2^12; % Num points for fft
i = 1:n;
t = p/300; % Length of time vector in seconds
tyd(:,1) = i(:)/300;
n_gem = floor(n/p); % Number of averages that will be calculated fir the fft
df = 1/t


channels(1,:) = (['Time     ']);
channels(2,:) = (['Vert LF  ']);
channels(3,:) = (['Vert RF  ']);
channels(4,:) = (['Axial L  ']);
channels(5,:) = (['Axial R  ']);
channels(6,:) = (['Vert LB  ']);
channels(7,:) = (['Vert RB  ']);
channels(8,:) = (['Trans    ']);
channels(9,:) = (['Bending  ']);
channels(10,:) = (['Bending L']);
channels(11,:) = (['Bending R']);
channels(12,:) = (['Torsion  ']);

% Calibration of data
K(1) = 1/8.2/2;%0
K(2) = 1/8/2;%1
K(3) = 1/8/2;%2
K(4) = 1/0.445;%3
K(5) = 1/7.865/2;%4
K(6) = 1/7.90/2;%5
K(7) = 100;%6
% Strain data: 1 mV/V = 2*2000 micro strain
% Stress = 207e9*2000*2*(2/k)/2
K(8) = 207e3*4000/2.085;
K(9) = 207e3*4000/2.085;
K(10) = 207e3*4000/2.085; % Bending stress front in MPa (k = 2.085)
K(11) = 207e3*4000/2.09; % Bending stress LB in MPa (k = 2.09)
K(12) = 207e3*4000/2.09; % Bending stress RB in MPa (k = 2.09)
K(13) = 207e3*4000/2.12; % Torsion stress front in MPa (k = 2.12)
K(14) = 207e3*4000/2.065; % Torsion stress front in MPa (k = 2.065)
```

```
j = 2:m+1;
cal_data(:,1) = tyd;
for ii = 2:m+1;
    cal_data(1:n,ii) = meting(1:n,ii-1)*K(ii-1);
end
cal_data = meting;
gem = mean(cal_data(:,2:m));

% Calculating the average fft
fft_data = zeros(p,m-1);
han_mat = ones(p,m-1);
ch = 2:m-1;
for teller = 1:m-1
    han_mat(:,teller) = hanning(p);
end
for ii = 1:n_gem;
    low = ((ii-1)*p)+1; % For calculating the average fft we need to step through the data
points
    high = (p*ii);
    raw_fft(:,ch) = abs(fft(cal_data(low:high,ch)))/(p)^0.5;
    fft_data = fft_data + han_mat.*raw_fft;
end
fft_gem = fft_data/n_gem;
q = 1/t:1/t:p/t; % fft time vector
stoordata = (fft_gem);
stoornaam = ([data(1:end-4),' Verwerkte fft.csv']);
csvwrite(stoornaam,stoordata); %

% Peak counter
% Store the peaks in a matrix -------- peak(level, ch)
% Minimum peaks will be store first
N_level = 12; % Fixed number of counting bins
Peak_range = 2.4; %Total peak to peak acceleration range which will be seperated in N_level
counting bins [g]
Dpeak = (Peak_range/N_level); % Delta between peak bins
peakcount_ch = [2 6]; % Measurement channels used for peak count
peak(N_level,size(peakcount_ch,2)) = zeros; % Set peak count to zero

for jj = 1:size(peakcount_ch,2);
    ch = peakcount_ch(jj);
    for ii = 3:n-3;
        % Search for all postive peaks
        if cal_data(ii,ch) >= cal_data(ii-1,ch) &...
                cal_data(ii,ch) >= cal_data(ii-2,ch) &...
                cal_data(ii,ch) >= cal_data(ii+1,ch) &...
                cal_data(ii,ch) >= cal_data(ii+2,ch)
            pk = (cal_data(ii,ch) - gem(ch-1));
            % Seperating the peaks into bins as defined with Dpeak
            if pk > 0 & pk <= Dpeak
                peak(7,jj) = peak(7,jj) + 1;
            elseif pk <= 2*Dpeak & pk > Dpeak
                peak(8,jj) = peak(8,jj) + 1;
            elseif pk <= 3*Dpeak & pk > 2*Dpeak
                peak(9,jj) = peak(9,jj) + 1;
            elseif pk <= 4*Dpeak & pk > 3*Dpeak
                peak(10,jj) = peak(10,jj) + 1;
            elseif pk <= 5*Dpeak & pk > 4*Dpeak
                peak(11,jj) = peak(11,jj) + 1;
            elseif pk > 5*Dpeak
                peak(12,jj) = peak(12,jj) + 1;
            end
        end
        % Now search for all negative peaks
        if cal_data(ii,ch) <= cal_data(ii-1,ch) &...
                cal_data(ii,ch) <= cal_data(ii-2,ch) &...
                cal_data(ii,ch) <= cal_data(ii+1,ch) &...
                cal_data(ii,ch) <= cal_data(ii+2,ch);
            pk = abs(cal_data(ii,ch) - gem(ch-1));
            % And seperate them into the appropriate levels
            if pk > 0 & pk <= Dpeak
                peak(6,jj) = peak(6,jj) + 1;
            elseif pk <= 2*Dpeak & pk > Dpeak
                peak(5,jj) = peak(5,jj) + 1;
            elseif pk <= 3*Dpeak & pk > 2*Dpeak
                peak(4,jj) = peak(4,jj) + 1;
            elseif pk <= 4*Dpeak & pk > 3*Dpeak
```

```
                peak(3,jj) = peak(3,jj) + 1;
            elseif pk <= 5*Dpeak & pk > 4*Dpeak
                peak(2,jj) = peak(2,jj) + 1;
            elseif pk > 5*Dpeak
                peak(1,jj) = peak(1,jj) + 1;
            end
        end
    end
end

figure(1)
peak

range = (-Peak_range/2+Dpeak:Dpeak:Peak_range/2);
barh(range,peak), colormap(cool)
set(gca,'YLimMode','manual');
set(gca,'YLim',[-1 1]); % sets the x axis to freqlow and freqhigh
legend('Front', 'Rear');

% Plotting the fft data
numcolor = 8;
some_colors = hsv(numcolor);

figure(2)
hold on;
for i = [2 6];
    %plot(q, abs(fft_gem(:,i)),'b');
    line('xdata',q,'ydata', abs(fft_gem(:,i)), 'color',some_colors(i,:)); % line plot of the
data
end
set(gca,'XLimMode','manual');
set(gca,'XLim',[0 150]); % sets the x axis to freqlow and freqhigh
% set(gca,'YLimMode','manual');
% set(gca,'YLim',[0 0.1]); % sets the x axis to freqlow and freqhigh
title(['Vertical Corner Acceleration FFT: ', filename(1:end-4)],'Interpreter','none');
xlabel('Frequency [Hz]')
ylabel('Acc [g]');
legend('Front','Rear')
grid on;
box on;
savename = ([data(1:end-4)]);
saveas(2,savename,'png');

save_peak = peak';
```

Appendix E Material Specification Sheets

MATERIAL PROPERTIES

Pultex® Fiber Reinforced Polymer **SuperStructural** Profiles

Angles

Angle profiles larger than 76 mm x 76 mm x 6.4 mm angle are **SuperStructurals**.
Note: 76 mm x 76 mm x 9.52 mm is a **SuperStructural** *Angle.*

Metric Version

1500 Series - Thermoset Polyester – Olive Green
1525 Series - Thermoset Polyester Class 1 FR – Slate Gray (Dark Gray)
1625 Series - Thermoset Vinyl Ester Class 1 FR – Beige

Pultex® **SuperStructural** Profiles are identified with imprinted veil.

The following data was derived from ASTM coupon and full section testing. The results are average values based on random sampling and testing of production lots. Composite materials are not homogeneous; and therefore, the location of the coupon extraction can cause variances in the coupon test results. Creative Pultrusions publishes an average value of random samples from production lots.

Property (coupon values)	ASTM Test	Units	1500/1525 Series	1625 Series
Mechanical				
Tensile Strength (LW)	D638	MPa	213.1	244.7
Tensile Strength (CW)	D638	MPa	113.4	129.9
Tensile Modulus (LW)	D638	GPa	24.1	24.1
Tensile Modulus (CW)	D638	GPa	6.9	6.9
Compressive Strength (LW)	D695	MPa	266.7	306.9
Compressive Strength (CW)	D695	MPa	175.3	199.4
Compressive Modulus (LW)	D695	GPa	20.6	20.6
Compressive Modulus (CW)	D695	GPa	15.1	15.1
Flexural Strength (LW)	D790	MPa	299.1	344.9
Flexural Strength (CW)	D790	GPa	165.1	189.1
Flexural Modulus (LW)	D790	MPa	13.1	13.1
Flexural Modulus (CW)	D790	GPa	11.0	11.0
Modulus of Elasticity	Full Section[2]	GPa	19.2	19.2
Shear Modulus	Full Section[2]	GPa	3.4	3.4
Interlaminar Shear (LW)[4]	D2344	MPa	23.4	26.8
Shear Strength By Punch (PF)	D732	MPa	37.8	41.2
Notched Izod Impact (LW)	D256	J/m	1,814.9	2,081.8
Notched Izod Impact (CW)	D256	J/m	1,761.5	2,028.4
Maximum Bearing Strength (LW)	D953	MPa	226.9	261.2
Maximum Bearing Strength (CW)	D953	MPa	226.9	261.2
Poisson's Ratio (LW)	D3039	mm/mm	0.35	0.35
Poisson's Ratio (CW)	D3039	mm/mm	0.12	0.12
In-Plane Shear (LW)	Modified D2344[3]	MPa	48.3	48.3
In-Plane Shear (LW) (through heel of angle)	Full Section*	MPa	23.4	26.9

**Note: Based on Full Section Connection Test*

Additional properties located on back

CREATIVE PULTRUSIONS, INC.
214 Industrial Lane ■ Alum Bank, PA ■ 15521
814-839-4186 ■ Fax: 814-839-4276
Web site: http://www.creativepultrusions.com ■ E-mail: crpul@pultrude.com

CPM060-0199-6.50
Revision Date: 10/9/06

XTRAL 728®

A generation ahead

Sheets and plates

Description

This data sheet gives information on the properties of Alcan Issoire's new XTral 728® alloy. XTral 728® has been optimized to upgrade the product Rm x A % together with the safety of tankers following ADR rules.
The alloy complies ADR evolution with the new equivalence formula.

Optimized dimensioning of tankers

XTral 728® makes it possible to achieve a level of RM x A % ≥ 7280 and therefore build safe aluminium tankers with the compulsory minimum thickness of 5 mm. It also retains the weight advantages aluminium has over steel.

Alloy	5083	5186	XTral 728®
Rm (MPa)	275	275	280
A % $_{t\geq5}$	17	24	26
Rm x A % $_{t\geq5}$	4675	6600	7280
Equivalent thickness (mm) old formula	5,12	4,57	
Equivalent thickness (mm) new formula	6,64	5,28	5

Reference specifications

This alloy from the 5xxx Series is registered with the Aluminium Association.
It is currently being introduced into the main european standards; for example EN 14286. For the time being the reference will be the Alcan standard IS 5022.
On request it can be delivered with TÜV acceptance as VdTÜV 549 and EN 10204-3.1A.

Chemical composition

	Si %	Fe %	Cu %	Mn %	Mg %	Cr %	Zn %	Zr %	Others (%) each	Others (%) total
Min.		0,10		0,20	4,70		0,20			
Max.	0,20	0,35	0,25	0,50	5,50	0,15	0,40	0,15	0,05	0,15

Remainder : Al

Physical properties

Density g/cm³	2,65
Melting interval °C	580-640
Linear expansion coefficient (0 to 100 °C) $10^{-6}.K^{-1}$	23,9
Modulus of elasticity MPa	71000
Poisson's ratio	0,33

Minimum mechanical properties

Temper	Thickness (mm)	Rm (MPa)	Rp 0,2 (MPa)	A $_{t\geq5}$ (%)	Bend radius 90° (indicatif)
O / H111	4 ≤ t ≤ 10	280	135	26	1,0 x thickness

Rm x A % $_{t\geq5}$ = 7280 (guaranteed minimum)
Rm x A % $_{t\geq5}$ > 8000 (typical value)

Impact Charpy notch test

	Sampling direction	Shape of test-piece	Test temperature °C	Specific energy J/cm²
Guaranteed mini	TL	DVM	20	25
Typical				> 40

Dimensional possibilities

Thickness (mm)	Width (mm)	Length (mm)
4 to 10	1000 to 2500	2000 to 15000

Please contact Alcan Issoire for all other shapes as per specific drawing.